A compact neutron spectrometer for detecting neutrons produced by cosmic rays

Erin Jarvie

A thesis presented for the degree of
Master of Science

University of Cape Town
Department of Physics
2023

Abstract

The high energy secondary neutron fields from cosmic radiation that are found in aviation and space environments have impacts on both biological and technological systems. A compact neutron spectrometer that is safe to operate in an aviation environment and suitable for detecting these secondary neutrons has been developed. The detector consisting of a ($0.6\times0.6\times12.0$ cm^3) EJ-276 plastic scintillator coupled to a silicon photomultiplier (SiPM) has been designed, constructed and characterised with neutrons up to 62.5 MeV at the UCT n-lab, IRSN AMANDE and iThemba LABS fast neutron facilities. The compact detector displays good quality pulse shape discrimination for the separation of neutron and gamma ray events. Neutron energy spectra were obtained through time-of-flight (ToF) measurements and spectrum unfolding. The energy spectra obtained from ToF display energy resolution similar to that obtained by a BC-501A reference detector. A matrix of measured response functions for neutrons with energies between 11 MeV and 62 MeV at 3 MeV intervals selected by ToF has been constructed for the detector. The response functions have been used to successfully unfold neutron energy spectra across the entire range of energies.

Acknowledgements

First and foremost I'd like to thank my supervisors Tanya Hutton and Andy Buffler for all of the support and guidance over the last two years; along with the rest of my supervisory team, Rendani Nndanganeni and Zina Ndabeni, for the time and effort put into editing of abstracts, presentations, proceedings and of course this thesis.

This project would not have been possible without the funding from SANSA, UCT and the NRF. Additionally, I'd like to thank the UCT Department of Physics and the wonderful people in it for not only the help and support on this project, but also being a home for me over the last few years. With a special thank you to Chloé Sole for the guidance and help she gave me with QtDAQ (and morale) even after she left the department.

Many thanks to Richard Babut and the whole team at the IRSN for the spectacular beam time at their AMANDE facility and making our stay in France so enjoyable.

I also thank Charlot Vandevoorde and the other contributors to the South African Space Neutron Initiative (SASNI).

Lastly, I'd like to thank my family and friends for all their love and support throughout the last two years. And a special shout out to my army of proof readers: Penny, Ant, Rachel, Jenni, Senyo, Sabrina, Jenna, Shanyn and Naledi. It truly takes a village (to submit a thesis).

Contents

Chapter 1

Introduction

The high energy secondary neutron fields that originate from cosmic rays [1, 2, 3] can have serious impacts on both biological and technological systems in aviation [4, 5] and space environments [6, 7]. Historically, fast neutron spectroscopy has either required the use of flammable xylene-based liquid scintillators or large gas filled detectors, along with bulky analog electronics; making in-situ measurements on board air- and spacecraft difficult. The development of plastic scintillators capable of discriminating between neutron and gamma ray events, compact silicon photomultipliers (SiPMs) and digital data acquisition systems in more recent years presents the opportunity to develop a new compact and portable detector system for performing fast neutron spectroscopy outside a laboratory environment a possibility.

Cosmic rays that enter the Earth's atmosphere collide with atoms and molecules producing secondary radiation cascades. At aviation altitudes the neutron energy spectrum takes the form shown in Figure 1.1, with a significant contribution between 1 and 100 MeV. The dose rate at these altitudes is significantly higher than at ground level and aircrew are subsequently exposed to an average of 2-6 mSv per year, with secondary neutrons making up roughly 55% of the ambient dose equivalent [5]. The neutron fluence varies significantly with solar activity, geomagnetic latitude and altitude, and for the most part can be accurately estimated through simulation [8, 9]. However, space weather events such as solar flares and coronal mass ejections can result in short lived and localised increases in the dose rate which cannot accurately be accounted for in the calculations of annual dose [5].

There is currently very little observational data on the neutron fluence during these kind of space weather events due to their unpredictable, fleeting and localised nature. An ideal solution would be to have a wide network of radiation detectors installed on aircraft which monitor the neutron field. However, without financial incentive or legal obligation airlines would be unlikely to agree. An alternative solution being implemented by projects such as Cosmic on Air [10, 11, 12] and the Smart Atmospheric Ionizing RAdiation network (SAIRA) [13] is the use of citizen volunteers to conduct the measurements when they fly. For a detector system to be suited to a citizen science project or be permanently installed in an aircraft the device must be compact, robust, user friendly and safe to operate on

board on aircraft, in addition to being able to perform neutron spectroscopy on neutrons with energies up to 100 MeV.

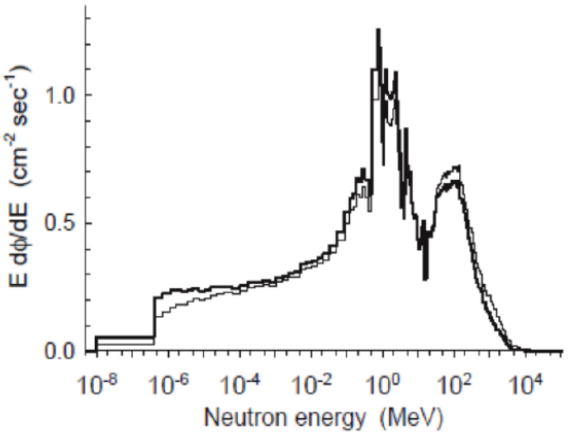

Figure 1.1: Neutron energy spectrum at an altitude of 20 km at 54°N, 117°W. The darker line is the measured spectrum by Goldhagen et al.[1] and the lighter line is the calculated spectrum produced by Clem et al. [14].

1.1 Currently available detector systems

There are a large number of neutron detectors available commercially, however there are none available that meet all three requirements of being compact, capable of performing fast neutron spectroscopy and being safe to operate in an aviation setting. The majority of the compact detectors on the market are personal dosimeters such as thermoluminescent dosimeters (TLDs) [15] and Tissue Equivalent Proportional Counters (TEPCs) [16, 17] which cannot perform spectroscopy; or spectrometers that are only suitable for low energy neutrons, for example small gas filled detectors. The spectrometers that are sensitive to high energy neutrons tend to be large and often unsafe to operate onboard aircraft due to flammability or the requirement for high voltages.

Measuring the neutron field in an aviation setting is not an impossible task and has been done successfully in previous studies [18, 19, 20]. Some of these studies [18, 19] used a multisphere neutron spectrometer (Bonner sphere) system which utilises ^{3}He filled proportional counters surrounded by high density polyethylene moderators of varying thicknesses (between 6.7 cm - 38.0 cm). These detector systems, while effective, are incredibly large and consist of many components. The neutron fluence has also been measured with a phoswich type detector [20] consisting of a 12.17 cm diameter and 12.17 cm long EJ-309 liquid scintillator covered with a 15 mm thick EJ299-33 plastic scintillator. This system is far more compact than the multisphere system however it is still fairly large, weighing in at 10 kg with dimensions of 19 $\varnothing \times 57$ cm^{3}. In more recent years there has also been research into the development of silicon based neutron detectors, both as dosimeters [13] and spectrometers [21, 22].

The instrumentation on spacecraft have to be as compact and light weight as possible. Since detecting high energy neutrons requires larger and heavier detector systems, the majority of neutron spectrometers and dosimeters that have been fitted to spacecraft are only sensitive to low energy neutrons, with energies from the thermal region up to around 20 MeV. These devices are primarily used to detect albedo neutrons from planetary and lunar surfaces [23, 24] or the lower energy neutrons produced cosmic ray particles interacting with spacecraft materials [25] and include TLDs, activation foils and Bonner spheres [26]. While there are no commercially available detectors that meet all our requirements, there have been a small number of devices deployed on spacecraft capable of detecting neutrons up to these high energies. In space environments the majority of the neutrons stem from interactions of cosmic ray protons with the materials of spacecraft and the most significant contribution to the effective dose is from neutrons with energies from 20 MeV up to several hundred MeV [25]. The most notable detector that has conducted measurements of the neutron field in space is the Radiation Assessment Detector (RAD) aboard the Mars Science Laboratory which has measured the neutron field on Mars between 8 MeV and 740 MeV [27]. The RAD consisted of a cesium iodide scintillator (for gamma ray detection) and a plastic scintillator (for neutron detection) with three silicon detectors used to exclude charged particles through anticoincidence.

1.2 Previous work at the University of Cape Town

Over the last decade the Department of Physics at the University of Cape Town (UCT) has been conducting research with the aim of developing a compact neutron spectrometer comprised of plastic scintillators, silicon photomultipliers (SiPMs) and digital data acquisition. This work has involved the characterisation of plastic scintillators with neutrons of energy exceeding 100 MeV [28] the development and characterisation of a digital data acquisition system for neutron spectroscopy [29, 30, 31] and the development of several SiPM based compact neutron spectrometer prototypes [32, 33, 29, 34].

The first prototype [29, 32] consisted of a single 0.6 × 0.6 × 15.0 cm^3 EJ299-33 plastic scintillator coupled to two SiPMs and was tested with neutrons from an ^{241}Am-^{9}Be source and 14.1 MeV neutrons from a D-T neutron generator. Response functions for this detector were produced through GEANT4 simulations and the neutron energy spectra were successfully determined from unfolding analyses. Subsequent version of the detector [35, 34] consisted of a 0.6 × 0.6 × 5.0 cm^3 EJ-276 plastic scintillator (the newer version of EJ299-33) coupled to a single SiPM. This detector was also tested with neutrons from an AmBe source and 14.1 MeV neutrons from a D-T fusion neutron generator. Response functions were not constructed for this detector, instead the neutron response of the detector was calibrated using a response matching with the response functions of an EJ-301 liquid scintillator and PMT detector. The light output spectra were then unfolded using the response functions for the EJ-301 detector with limited success, implying the need for detector specific response functions to obtain accurate energy spectra. Due to the length of the scintillator in this device, the design would likely only be suitable for neutrons up to approximately 65 MeV.

1.3 Objectives of the Present Work

The work presented in this thesis aims to further investigate the development of a plastic scintillator, SiPM and digital data acquisition based compact neutron spectrometer suitable for measuring the secondary neutron field produced by cosmic rays at aviation altitudes. To further the research done in previous work a detector comprised of EJ-276 scintillator with dimensions $0.6 \times 0.6 \times 12.0$ cm^3 coupled to a single 0.6×0.6 cm^2 SiPM was built and characterised with neutrons up to 62.5 MeV. The main objectives of the presented work were to:

- construct a compact neutron spectrometer capable of detecting neutrons with energy between 1 MeV and 100 MeV;
- conduct measurements campaigns at the UCT n-lab, IRSN AMANDE and iThemba LABS fast neutron facility to test the detector with neutrons up to 62.5 MeV;
- characterise the light output response of the detector for both gamma rays and neutrons;
- construct a matrix of measured response functions for neutrons with energies up to 62 MeV using the time-of-flight measurements performed at iThemba LABS [36];
- obtain neutron energy spectra through unfolding using the constructed response matrix;
- compare the performance in terms of edge resolution, energy resolution and quality of pulse shape discrimination of the compact spectrometer to a reference detector consisting of a liquid scintillator coupled to a 12-stage PMT; and
- investigate the directional sensitivity of the detector.

One of the long term goals of developing this compact spectrometer is for it to be used in citizen science projects such as Cosmic On Air to increase the amount of observational data on the neutron field at aviation altitudes particularly in the Southern Hemisphere. To be used in such a project there are additional requirements for the detector to be:

- compact to the degree of being hand-held;
- safe to fly with and make it through airport security easily;
- robust and user friendly; and
- cost effective.

A key modification that has been made to the design by Comrie [29] is the use of a single SiPM. Comrie's work showed that the addition of a second SiPM to the detector resulted in an improvement of the light output edge resolution, however it also increases the cost, size and complexity of the device. The subsequent design [35, 34] demonstrated that it was possible to perform good quality neutron spectroscopy with a single SiPM when using a short (5 cm) scintillator, however the short scintillator limits the effectiveness of the detector at high energies. This work aimed to determine whether a single SiPM design with a longer scintillator can perform neutron spectroscopy effectively at high energies.

Chapter 2

Cosmic Rays

The term cosmic radiation refers to the flux of ionising radiation that enters the Earth's atmosphere from outer space [3, 6]. The majority of the radiation bombarding the Earth is deflected by its magnetic field, and the radiation that enters our atmosphere is largely attenuated by interactions with atmospheric particles. These interactions lead to a wealth of secondary particles such as neutrons, pions, photons, electrons and muons being produced. The production of secondary particles is at a maximum at an altitude between 14 km and 20 km above sea level, this altitude is known as the Regener-Pfotzer maximum (R-P max) [37]. Below the R-P max the amount of ionising radiation in the atmosphere steadily decreases. The composition of the radiation field therefore depends on altitude, as shown in Figure 2.1. The energy and flux of cosmic rays entering the Earth's atmosphere also depends on the geomagnetic latitude [38]. Due to the shape of the geomagnetic field it is easier for particles to enter in polar regions than at equatorial regions, resulting in a higher particle flux near the poles [39].

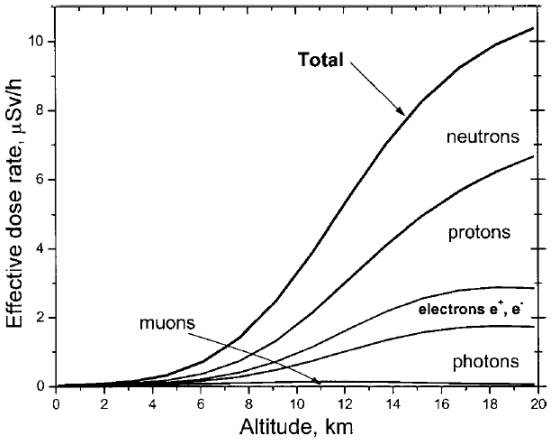

Figure 2.1: Effective dose rate and composition of the radiation field as a function of altitude above sea level [40].

Cosmic radiation is made up of two main components: galactic cosmic rays (GCR) which originate from outside our solar system and solar energetic particles (SEPs) which stem from the Sun, primarily from phenomena such as solar flares and coronal mass ejections [41, 42]. In this Chapter the radiation field produced by cosmic rays and space weather events will be discussed in detail with a focus on the effects at aviation altitudes.

2.1 Galactic Cosmic Radiation

Galactic cosmic radiation is the dominating source of cosmic radiation, contributing roughly 95% to the radiation field at aviation altitudes [43]. These cosmic rays, which are believed to originate from supernova remnants [44], impinge isotropically onto our atmosphere with energies up to 10^{20} eV [42]. Approximately 98% of these particles are nuclei, comprised of roughly 87% hydrogen, 12% helium and 1% heavier nuclei [45, 5].

The GCR field is well studied and can be accurately modelled and predicted. The particle flux varies as a function of time in a way that is oppositely correlated with the solar cycle. The solar cycle is characterised by the number of sunspots observed on the Sun's surface, which vary over an 11-year cycle and give an indication of the amount of activity on the Sun. Figure 2.2 shows the relationship between sunspot number (plotted in red) and neutron counting rate (plotted in black) between the years 1960 and 2010. Sunspots are regions on the Sun with very strong magnetic fields [46]. The high concentration of magnetic flux in these regions results in reduced surface temperature and therefore appear as dark spots on the Sun. Since phenomena such as prominences, solar flares and coronal mass ejections occur due to magnetic reconnection, the presence of sunspots will often lead to solar events like these occurring too [47].

Solar wind is the constant flow of ionised particles (plasma) emitted from the upper atmosphere of the Sun, known as the corona, far into space [42]. The solar wind plasma is comprised of mostly protons and electrons, however does contain some heavier nuclei. Embedded in the solar wind is the heliospheric magnetic field (HMF), also known as the interplanetary magnetic field (IMF) [48]. This magnetic field is the component of the Sun's magnetic field which has been dragged out by the highly conductive solar wind. The interaction of the solar wind and HMF with the Earth's magnetosphere is what gives it its distorted shape, seen in Figure 2.3, and the interaction of solar wind particles with the magnetosphere is what causes auroras at the poles [49].

When GCR coming towards our solar system encounters the HMF, the particles are decelerated [50]. During periods of high solar activity (solar maximum) the intensity of the solar wind and HMF increases, resulting in greater deceleration of the incoming GCR protons, particularly affecting those of lower energy. This process, known as cosmic ray modulation [51], is what causes the variation in GCR flux entering the heliosphere and our atmosphere as shown in Figure 2.2.

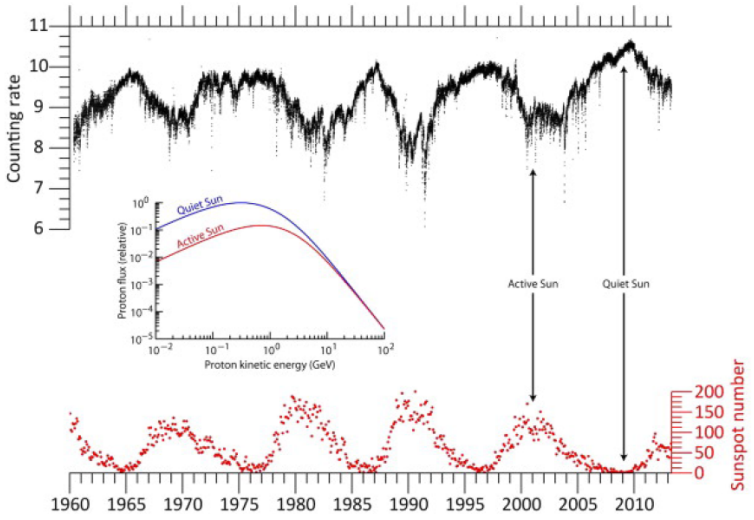

Figure 2.2: Neutron counting rate (units of 10^5 counts per hour) measured at McMurdo Station in Antarctica as a function of time from 1990 to 2013 shown in black. The monthly sunspot number over the same time period is shown in red. A comparison between the two plots shows the anti-correlation between sunspot number and neutron counting rate. During less active solar periods (low sunspot number) more lower energy protons can reach the Earth, shown in the plot in the centre of the figure. The increase in the number of lower energy protons is what causes the increase in neutron counting rate [52].

2.2 Solar Energetic Particles

Solar energetic particles (SEPs) are distinct enhancements of high energy particles from the Sun that can last for a few hours up to several days [53, 54]. The particles, consisting primarily of protons, electrons and photons, are accelerated to energies that range from 10 keV to several GeV by jets, solar flares and the shock waves produced in the interplanetary medium by coronal mass ejections in what are referred to as solar particle events [55].

SEPs are divided into two categories: impulsive and gradual. These two categories have distinct differences in characteristics such as electron to proton ratio, the intensity-time profiles and the mean ionic charge of heavy ions [56]. The differences in these two classes stems from the mechanisms which accelerate them. Impulsive SEPs are accelerated by solar flares, while gradual SEPs are accelerated by shock waves in the interplanetary medium produced by coronal mass ejections.

Solar flares are rapid and intense bursts of high energy radiation caused by the release of energy during magnetic reconnection in the Sun's photosphere [57]. Solar flares emit large amounts of electromagnetic radiation across the entire electromagnetic spectrum, along with electrons, protons and heavy nuclei which are accelerated in the solar atmosphere. SEPs from solar flares have an elevated abundance of ^{3}He, ^{4}He, heavy ions and electrons

in comparison to the solar wind [58, 59] since they originate from the hot plasma solar photosphere.

Coronal mass ejections (CMEs) are large expulsions of plasma and accompanying magnetic field from the Sun's corona. CMEs propagate at speeds between a few hundred km s^{-1} and 3000 km s^{-1} [60, 61]. However in cases when the velocity of the CME exceeds that of the local solar wind (between 350 km s^{-1} and 750 km s^{-1} [62, 63]), a bow shock will be established ahead of the the CME [64]. The particles that are accelerated by the CMEs reflect the abundances and temperature of coronal material in the solar wind. The most intense and energetic SEP events are the result of CME shock waves [65].

Geomagnetic storms are major disturbances in the Earth's magnetosphere caused by an efficient transfer of energy from the solar wind to the Earth's magnetosphere [66]. A geomagnetic storm is characterised by significant decrease in the horizontal component of Earth's magnetic field [67, 68], usually lasting a few hours, followed by its recovery which could last several days [69]. The occurrence of geomagnetic storms requires sustained strong solar wind with a southward z-component of the IMF. As shown in Figure 2.3, when there is a southward IMF it will connect with the northward magnetic field of the Earth. This magnetic reconnection releases energy and allows the solar wind plasma to enter the magnetosphere. The sudden influx of charged particles causes disturbances to the magnetic field, particularly near the poles. The high solar wind speeds required for geomagnetic storms are caused by CMEs and coronal holes, which are regions in the Sun's corona with less dense plasma and more open magnetic fields [70].

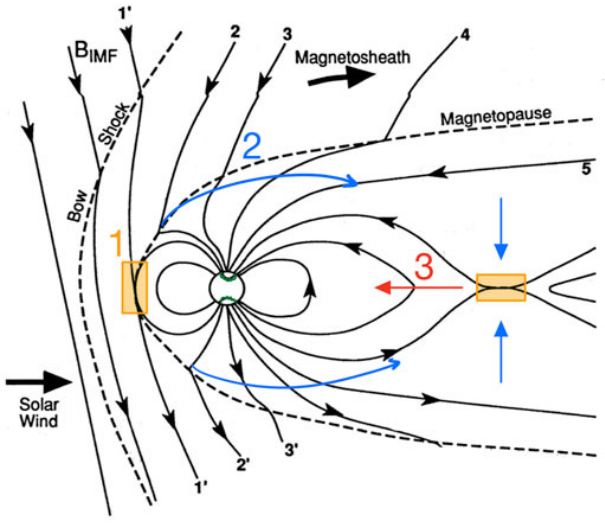

Figure 2.3: Diagram depicting the interaction between the Earth's magnetic field and a southward solar wind associated with geomagnetic storms [71]. The process starts (1) with magnetic reconnection of the southward solar wind and the Earth's magnetosphere at the day side of the magnetopause, (2) the magnetic field lines convect across the polar cap, transferring energy into the magnetotail, and (3) the large amount of energy transferred to the magnetotail prompts magnetic reconnection which send the plasma towards the Earth, causing a geomagnetic storm.

Impulsive and gradual SEP events occur over distinctly different time scales, as shown in Figure 2.4. Impulsive SEPs will typically last anywhere between several hours to several days and are characterised by a rapid increase followed by a rapid decrease in radiation intensity. Gradual SEP events last for several days and are characterised by a rapid increase in radiation intensity which then decreases very slowly. The main differences in properties are summarised in Table 2.1.

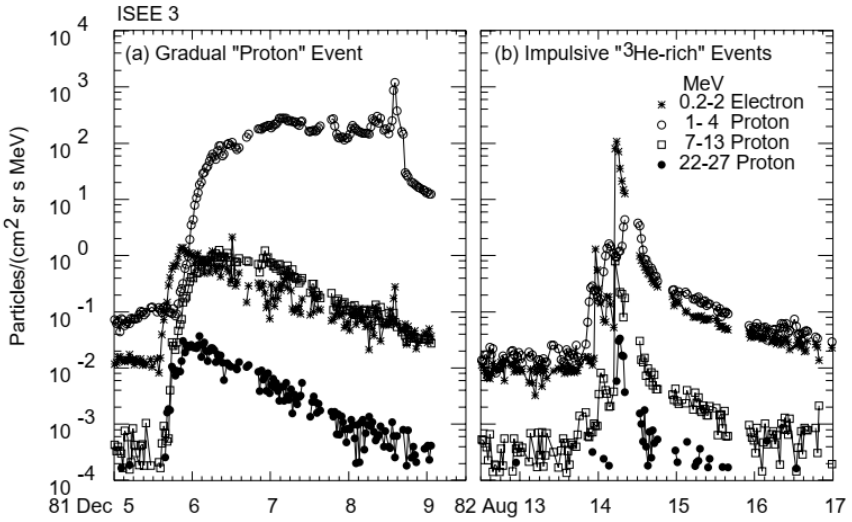

Figure 2.4: Intensity-time profiles of electrons and protons in various energy ranges in 'pure' (a) gradual and (b) impulsive SEP events [59].

Table 2.1: Properties of impulsive and gradual SEPs

Properties	**Impulsive**	**Gradual**
Acceleration event	Flares and jets	Coronal mass ejections
Elemental composition	He^3, electron and heavy ion-rich	Proton rich, very similar composition to solar wind
Duration	Short, hours to a couple of days	Long, several days
Events per year	$\sim$ 1000	$\sim$ 10

2.3 Secondary Neutrons from Cosmic Rays

Almost all of the neutrons associated with cosmic rays are produced as a secondary radiation field when the cosmic ray particles interact with other nuclei. Cosmic ray particles produce a plethora of secondary particles through interactions with other nuclei, a large proportion of which are high energy neutrons. These high energy neutrons stem from spallation of the target nucleus and the breakup of cosmic ray particles with $Z > 1$ [25]. The interactions deposit large amounts of energy into the material prompting the

release of more neutrons with lower energies (<30 MeV). The resulting neutron field is therefore strongly dependent on the type and thickness of material that the cosmic rays interact with and the composition of the primary cosmic ray field.

In space environments, the secondary neutron field is due to interactions with spacecraft, human and habitat materials [25], while in aviation environments they primarily stem from interactions with atmospheric nuclei. Due to the large amount of variable factors in space environments there is no standard secondary neutron energy spectrum, however from simulations it is expected that the majority of the neutron field within a spacecraft due to GCR would exist between 10^{-1} MeV and 10^{4} MeV. Within the Earth's atmosphere altitude plays one of the largest roles in determining the secondary neutron field. The neutron field at aviation altitudes (10 - 20 km) due to GCR is well known [1] and is shown in Figure 2.5. There will be slight variations in the energy spectrum depending on the flux of primary cosmic rays entering the atmosphere, which is linked to both solar activity and geomagnetic latitude. However, the neutron energy spectrum is expected to possess a similar overall shape with the most significant contribution within the 1 - 100 MeV energy range [8, 1].

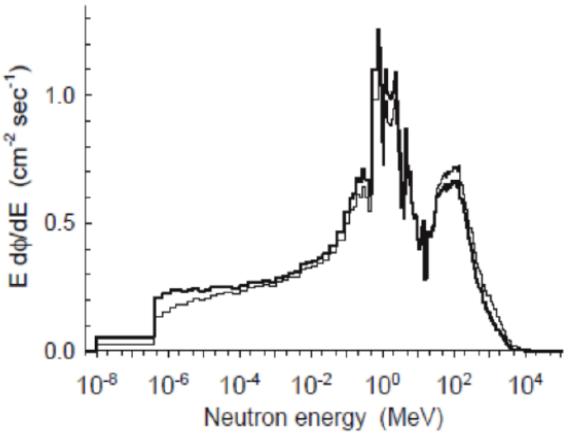

Figure 2.5: Neutron energy spectrum at an altitude of 20 km at 54°N, 117°W. The darker line is the measured spectrum by Goldhagen et al.[1] and the lighter line is the calculated spectrum produced by Clem et al. [14].

2.4 Monitoring of Cosmic Rays

The cosmic ray flux in space and on the Earth's surface is constantly being monitored. Ground-based neutron and muon detectors are currently the main instrumentation used for continuous real-time observations of cosmic ray intensity [72] in conjunction with space-borne detectors on spacecraft and satellites.

Neutron monitors (NMs) [73] are the detectors typically used for ground-based detection of secondary neutrons from cosmic rays. From the particles detected by NMs, spectral

information about the primary cosmic rays can be obtained with the use of atmospheric yield functions [74]. There is a world-wide network of NMs which are constantly monitoring the intensity of cosmic rays arriving at Earth. However, NMs are limited to obtaining information about the cosmic rays that have enough energy to enter the atmosphere and not have their secondary particles fully attenuated at ground level; which are primary cosmic rays with energies in the range of approximately 450 MeV to 100 GeV per nucleon [75]. The quality that determines whether a particle will be able to pass through the magnetosphere is not energy but rather momentum per charge - known as rigidity. Due to the shape of the magnetic field the minimum rigidity at the poles is 0 GV, while at mid latitudes its 17 GV [55]. In order for a particle to reach sea level it must have a rigidity of at least 1 GV, which for a proton is equivalent to an energy of 400 MeV [76].

The other primary method of monitoring cosmic rays is through detector systems onboard spacecraft and satellites like the Geostationary Operational Environmental Satellites (GOES), which detect the primary cosmic ray particles. Since they are outside the Earth's atmosphere they are able to detect the lower energy particles from SEPs.

2.5 Space Weather and Cosmic Rays

Space weather refers to conditions on the Sun and in the solar wind, magnetosphere and ionosphere that can affect space-borne and ground-based technological systems and human life [60, 77]. Space weather is made up of four main components: solar flares, SEPs, CMEs and high speed solar wind [78, 79]. In this section some of the impacts of space weather and GCR are discussed. Aviation is one of the industries most affected by cosmic radiation and space weather, therefore the regulations put in place to protect aircrew from the consequences of working in a high radiation environment and how dosimetry for aircew is conducted are also discussed in detail.

2.5.1 Biological impacts

It has been well studied that being exposed to high doses of ionising radiation increases risk of cancer, damage to the central nervous system, circulatory diseases and degenerative diseases [80, 81, 82, 83]. Ionising radiation can deposit energy at the cellular and sub-cellular level. These energy deposits result in ionisations which disrupt the atomic and molecular structure causing chemical and biological damage [84].

Ionising radiation can cause damage through direct and indirect mechanisms. Direct damage is caused when energy deposition results in single or double stand breaks which damages the bases in DNA and can lead to altered genetic coding information [85, 79]. The Linear Energy Transfer (LET) of a particle describes the amount of energy per unit length that particle a deposits [86]. Double strand breaks are associated with high-LET radiation due to their capability of depositing large amounts of energy in a localised area

and are difficult for the cell to repair, increasing the chance of mutations. Indirect effects are caused through the ionisation of water in the body producing free radicals can also damage DNA and result in genomic instability [87]. When the genetic code is altered it is known as a mutation. Mutations in DNA affect the ability of cells to divide normally which can lead to cancer and degenerative diseases.

The effectiveness of different radiation types is described by the quantity known as Relative Biological Effectiveness (RBE) [84]. RBE depends on the LET of the particle, with high-LET particles such as neutrons, protons and alpha particles also having high RBEs [88], as seen in Table 2.2.

Neutrons interact through elastic and inelastic collisions with nuclei which produce secondary particles such as charged particles, gamma rays and lower energy neutrons [89], as well as various nuclear reactions. The type of interactions and secondary particles produced is heavily dependent on neutron energy, and therefore so is the RBE. Both primary and secondary neutrons have the ability to penetrate far into matter and are high-LET particles. This and the production of secondary radiation makes them particularly dangerous for interactions with biological tissue. As a result, the secondary neutrons produced by cosmic rays and space weather events are one of the largest concerns when it comes to biological risk.

Table 2.2: The relative biological effectiveness (RBE) of various radiation types [90].

Type and energy of radiation	**RBE**
X-rays	1
Gamma rays	1
β-particles ($>$ 30 keV)	1
β-particles ($<$ 30 keV)	1.7
Neutrons (thermal to slow, $<$ 0.02 MeV)	2-5
Neutrons (fast, 1-10 MeV)	10 (body), 30 (eyes)
Protons (1-10 MeV)	10 (body), 30 (eyes)
Alpha particles from natural radiation	10-20

For astronauts, the risks associated with exposure to ionising radiation are very high. When outside the Earth's protective atmosphere and magnetosphere the radiation field from GCR is harsh (see Figure 2.6), consisting of a high flux of high energy, heavy ions and photons (gamma rays, x-rays and UV) with an energy spectrum that peaks near 1000 MeV per nucleon [80]. As discussed in Section 2.3, in conjunction with the primary radiation from the cosmic rays, large amounts of neutrons and recoil nuclei are produced by interactions with the spacecraft wall and the astronauts bodies. Astronauts are exposed to whole body doses of 1-2 mSv per day in interplanetary space and the radiation dose from GCR and SEPs is one of the largest long term health concerns for astronauts on manned space missions.

Due to the high energy of GCR radiation, equipping spacecraft with thick enough shielding to solve the issue of radiation dose is not practically possible since the mass would create

problems for launch [7]. Additionally, shielding in spacecraft ends up producing large amounts of secondary neutrons, ultimately increasing the radiation dose. Spacecraft are however, equipped with some shielding since it is effective at absorbing radiation from SEPs which are of significantly lower energy than GCR, typically between tens and hundreds of MeV. SEPs associated with solar flares are primarily a risk to astronauts during extra-vehicular activity. Since the radiation from solar flares travels near the speed of light, their effects are immediate and no early warning can be given. SEPs produce a high flux of radiation and as a result can impart very high doses if an astronaut is outside the shielded spacecraft. If the SEP event is very large astronauts could experience dose rates high enough that they could experience acute radiation affects (radiation sickness) [91, 92].

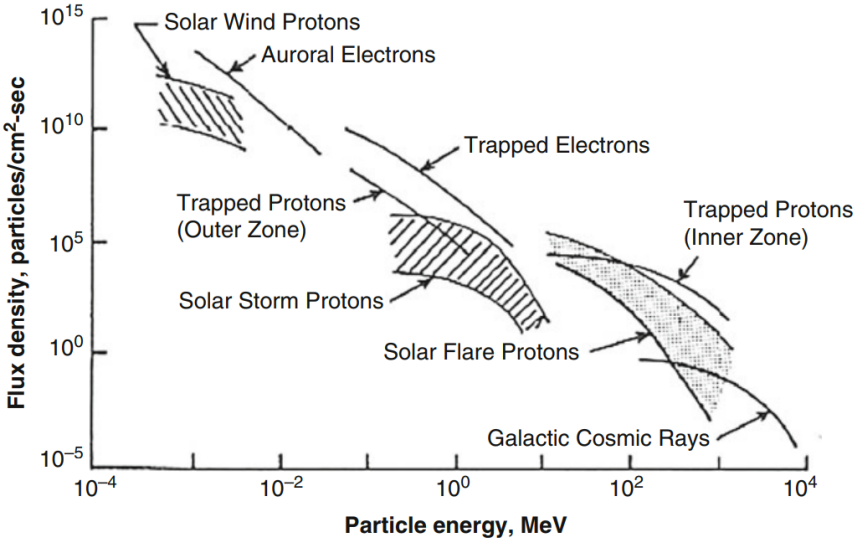

Figure 2.6: The space radiation environment [93].

Since aircrew experience long-term exposure to ionising radiation they also face an increased risk of cancer. Several studies have been undertaken investigating cancer in aircrew and it was found that they had increased risk of melanoma, brain, prostate and breast cancer [94, 95, 96]. However, the increased rates of cancer cannot be attributed solely to radiation exposure, many participants had other confounding factors such as circadian disruption [97, 98] and various lifestyle factors that have also been shown to increase cancer risk [99, 100].

2.5.2 Technological impacts

We rely heavily on semiconductor (primarily silicon) electronics in spacecraft, satellites and aircraft, however exposing this technology to ionising radiation fields can cause problems and damage components. The impacts of cosmic radiation on electronics can be divided into two categories, cumulative effects and single event effects.

Cumulative effects refer to changes in the device due to accumulated dose [101]. Energy deposited by non-ionising radiation causes defects in the material. The accumulation of these defects alter the material properties and therefore permanently change the way the device operates [102]. The most common cumulative effect is displacement damage, where an incident particle collides with an atom in the silicon lattice and dislodges it [103]. Neutrons around 1 MeV are known to be particularly efficient for causing displacement damage. Cumulative effects can be minimized by installing shielding and limiting operation time.

When ionising radiation passes through matter it deposits energy that ionises the molecules along its path. In electronics devices this creates a surge in current known as a Single Event Effect (SEE) which disrupts the operation of the device [104]. The SEE mechanism can produce short-term non-destructive errors, known as soft errors, which typically take the form of memory data corruption. It can also cause permanent catastrophic damage, known as hard errors.

Additionally, the electromagnetic radiation from solar flares can rapidly heat up the atmosphere to the point where satellites drop into lower orbits [60]. In the event of a geomagnetic storm the fluctuations in magnetic field can induce currents in conducting materials on the surface of the Earth [105]. As a result large geomagnetic storms can wreak havoc on our infrastructure, causing blackouts in electrical power grids, inducing current in pipelines and disrupting non-fibre optic communication cables [106].

2.5.3 Dosimetry and regulations in aviation

Commercial aircraft fly at an average altitude of 12 km, where the dose rate is roughly 100 times higher than at sea level [43]. In 1991 the International Commission on Radiological Protection (ICRP) recommended that air crew be considered occupationally exposed due to cosmic radiation [107]. As it stands, the recommended effective dose limit for occupationally exposed (non-pregnant) individuals is 20 mSv per year averaged over 5 years with no more than 50 mSv in one year [4]. For the general public the recommended limit is 1 mSv per year. With this recommendation in mind countries set their own regulations. For example, in the U.S. this recommendation is treated as an upper limit of acceptability [108], while for EU member states aircrew are required to undergo exposure assessment when it is likely they will be exposed to more that 1 mSv in a year and adjustment of work schedules so that no individual exceeds 6 mSv/year [109]. In South Africa aircrew are not recognised as radiation workers and therefore no radiation protection regulations for aviation currently exist [110, 111, 112].

On average aircrew receive a dose of 1.5 - 5 mSv per year [113], which is well below the ICRP dose limit. However during a large solar event the dose rate could increase anywhere from a few μSv h^{-1} to several mSv h^{-1} [114]. While the increase in dose rate is typically not significant, a particularly violent event could raise the dose rate high enough for the ICRP dose limit for passengers and even aircrew to be exceeded.

The dose received by aircrew is calculated through a combination of simulated data and data measured by the NM network [5]. Under normal conditions the simulated data is considered to be fairly accurate and has been shown to be in good agreement with measured values [115]. The verification of these models has been carried out over many years. The measurements of the neutron energy spectrum, most notably Goldhagen et. al. [1], and verification of the codes used to calculate neutron energy [2, 14] allowed for accurate calibration of dosimeters and accurate simulation of radiation dose. However, these codes are not able to accurately determine the dose during large solar events such as solar flares and CMEs [114].

Currently, when a solar event is large enough to result in a GLE, the data acquired from the NM network is used in conjunction with a simulation code to calculate an estimate of the dose [116]. While these simulations have improved over the years [117, 118], there are still large uncertainties associated with these estimates. Additionally, due to the complex relationships between solar activity and the conditions in the solar wind and the Earths' magnetic field it is not currently possible to predict which events will result in significant increases in the dose rate at aviation altitudes from observations of the Sun [114, 119, 116].

To verify and improve the current codes more observational data of both the dose and neutron energy spectrum at aviation altitudes during a GLE is needed. In the past the now decommissioned Concorde aircraft which flew at high altitudes were fitted with a radiation dose monitoring system, known as the In-Flight Radiation Warning Meter [120, 121, 122]. The meter was used to record the cumulative dose during the flight and would indicate the whether the instantaneous dose rate fell within 1–100 Sv h^{-1} (green), 100–500 Sv h^{-1} (amber) or above 500 Sv h^{-1} (red). Since these monitors were installed for radioprotection purposes the data was usually unsuitable for studying specific GLE events, with the exception of a few instances where the measurements during a GLE were saved [119]. The data recorded during this era has been instrumental in validating and improving the simulations used for calculating dose in both normal and GLE conditions [115]. However, to this day there is still a lack of observational data of dose and, in particular, the neutron energy spectrum during GLEs.

Due to the rare, transient and unpredictable nature of GLEs, constant widespread monitoring onboard aircraft, such as was implemented with Concorde, would be ideal for obtaining more observational data. While there are many dosimeters which are well suited to such a project, there are few neutron spectrometers which could be used. Currently Bonner sphere spectrometer systems are best suited for measuring neutron energy spectra onboard aircraft and have been the most widely used. However, as with all detector systems, to detect high energy neutrons larger detector volumes are needed. To achieve a more compact spectrometer, a detector materials with a higher efficiency than those used in Bonner spheres could be used, such as organic scintillators.

There is currently no program in place for widespread monitoring of the neutron energy spectrum onboard aircraft. An alternative method for increasing the amount of observational data at a low cost is the use of citizen-based campaigns, such as the Cosmic On Air project. This project utilises citizen volunteers to conduct measurements when

they fly. For such a project, a neutron spectrometer that is very compact and easy to operate by a non-expert is required.

Chapter 3

Neutron Spectroscopy with Organic Scintillators

The detection of radiation using organic scintillator materials dates back to the 1940s [123] and has been used for neutron spectroscopy since the early 1950s [124, 125]. Scintillation based detectors all operate in a similar way: radiation interacts with the detector material which produces photons in the visible light or UV spectrum, the photons are detected by a device which converts the photons to an electronic pulse, which is acquired through an electronics system. Through the manipulation of the acquired pulses, using various analysis techniques, spectral information can be extracted. In this Chapter the detection mechanism in organic scintillators, and the technology and analysis techniques used to perform neutron spectroscopy with organic scintillators are discussed in detail.

3.1 Organic Scintillators

Organic scintillators are widely used for fast neutron (E $>$ 1 keV) spectroscopy due to their high efficiency for neutron interactions, neutron-gamma pulse shape discrimination and fast timing resolution [126]. Organic scintillators are materials primarily made up of hydrogen and carbon which fluoresce when interacting with radiation. The fluorescence arises from transitions in the energy levels of a single molecule, since this is an inherent molecular property the fluorescence can be observed independently of the physical state [127]. As a result, organic scintillators can be gases, liquids or solids, in comparison to inorganic scintillators where the scintillation originates from the crystalline structure of the material and can therefore only exist as a solid.

The light output of an interaction is related to the scintillation efficiency of the material and the specific energy loss of the interacting particle within the scintillator. This relationship is well understood and can be described by Birk's relation [128]. The specific energy loss, and therefore light output, is dependent on the type of particle interacting in the scintillator. For neutrons with energies above 3 MeV [129] and gamma rays, the

light output as a function of particle energy is considered to be linear. Gamma rays and neutrons are both neutral particles and ionise the scintillation material indirectly through recoil electrons and charged particles respectively. As shown in Figure 3.1, the heavier charged particles, such as those produced from neutron interactions, produce a lower light output due to an increased number of energy depositions in the detector that don't result in scintillation, known as quenching.

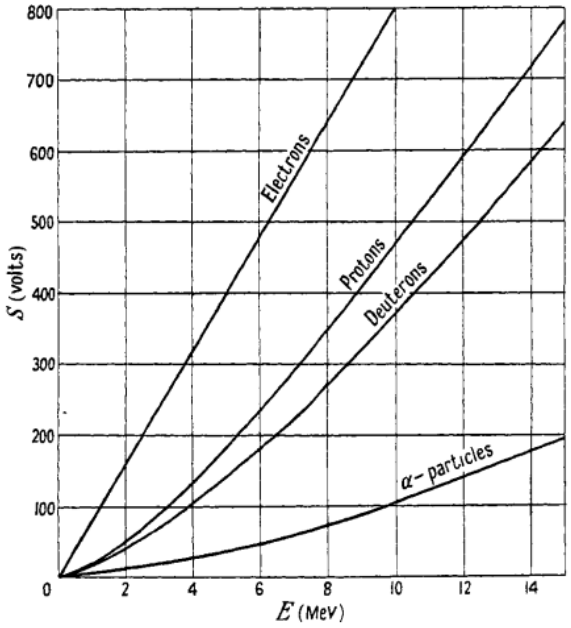

Figure 3.1: Relative scintillation response S (V) of anthracene to particles of energy E (MeV) [128].

Neutron fields are typically contaminated by gamma rays which originated either from the neutron source or interactions of the neutrons with other matter [130]. Organic scintillators are sensitive to both neutrons and gamma rays, therefore it is important to understand how both of these particles interact and the characteristics of the detector response they produce. In some organic scintillators the different interaction mechanisms of gamma rays and neutrons produce scintillation that decays over distinctly different time scales, a property that can be used to distinguish between gamma ray and neutron events using pulse shape discrimination (PSD).

3.1.1 Neutron interactions in organic scintillators

Neutrons are electrically neutral particles, thus they interact through non-coulombic mechanisms and ionise materials indirectly [131]. Neutrons interact with the nuclei of the material through elastic scattering, inelastic scattering or nuclear reactions; producing secondary heavy charged particles which go on to ionise the material through Coulomb interactions [132].

In the context of neutron interactions, the microscopic cross section (σ) describes the probability of a neutron interacting with a single atomic nucleus, a quantity that depends on the atomic nucleus and energy of the incident neutron (E_n). For a neutron interacting with a bulk material, the probability of interaction is described by the macroscopic cross section (Σ) which is specific to the nuclear density (N) of the material and is related to σ such that:

$$\Sigma(E_n) = \sigma(E_n)N. \tag{3.1}$$

The total macroscopic cross section is described as the sum of the macroscopic cross sections for all of the possible interaction channels.

For fast neutron interactions in organic scintillators elastic scatter off hydrogen and carbon nuclei dominate the total macroscopic cross section. During the scatter the incident neutron of energy E_N transfers energy (E_R) to the recoil nucleus, which can be described by Eq. 3.2:

$$E_R = \frac{4A}{(1+A)^2} cos^2(\theta) E_n, \tag{3.2}$$

where the atomic mass (A) of the nucleus and the scattering angle (θ) of the recoil are indicated in Figure 3.2.

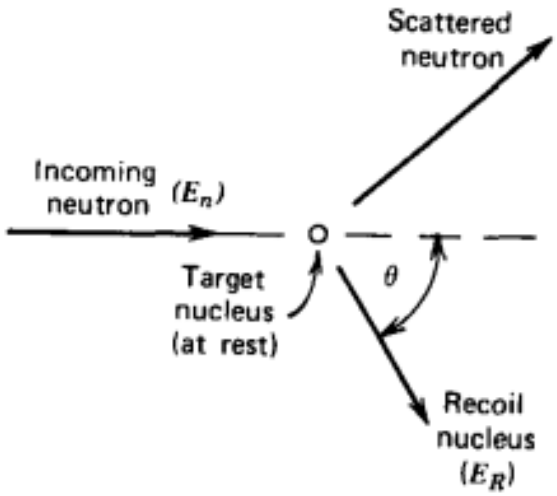

Figure 3.2: Elastic scatter of a neutron with energy E_n off a target nucleus in the lab frame. The interaction results in a scattered neutron and a recoil nucleus with energy E_R scattered through an angle of θ [133].

The energy transferred to the recoil nucleus has a dependence on the scattering angle. In most cases the scattering is isotropic, resulting in a rectangular response function from the detector. For a head-on collision ($\theta = 0°$) with a proton ($A = 1$), the full energy of the neutron can be transferred to the recoil proton and the edge of the response function

occurs at $E = E_n$, shown in Figure 3.3 (a). Hydrogen is therefore the most efficient neutron moderator and, as a result, proton recoil is the backbone of neutron detection in organic scintillators. The assumption of isotropic scattering in (n, p) scattering is only accurate for neutron energies < 10 MeV. At higher energies the angular distribution of the scatters becomes anisotropic, favouring small angle scatters and causing distortions to the shape of response function, as shown in Figure 3.3 (c).

Elastic scatter from hydrogen is the most important interaction in neutron detection with organic scintillators, however the other interactions that take place distort the proton recoil response function in various ways. In elastic scatter with carbon nuclei ($A = 12$), a head-on collision will only transfer 28% of the neutron energy to the recoil nucleus. This results in an enhancement in the response function at low energies (up to 0.28 E_n) as shown in Figure 3.3 (b). The scintillation efficiency in organic scintillators decreases with increasing Z, and therefore these interactions contribute little to the measured light output response.

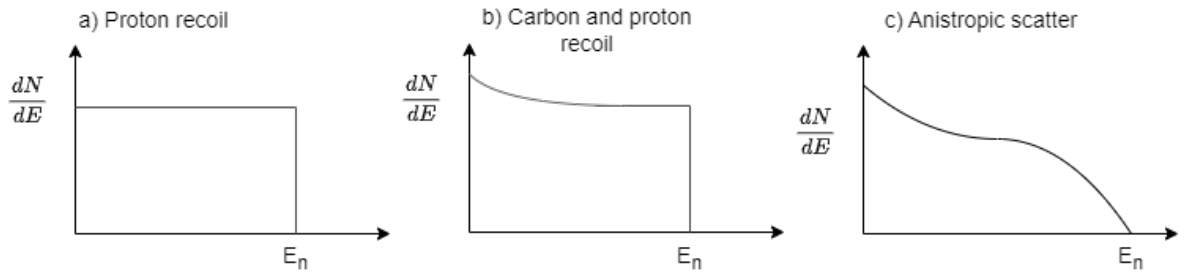

Figure 3.3: Detector response to (a) proton recoil interactions, (b) the distortion to the response caused by elastic scatter with carbon nuclei and (c) anisotropic elastic scatter associated with neutrons at high energies.

The other two interaction mechanisms, inelastic scatter and nuclear reactions contribute a small amount to the measured response and only begin to contribute above certain threshold energies. During inelastic scattering the recoil nucleus is elevated to an excited state from the collision, the nucleus will subsequently de-excite emitting gamma rays. Inelastic collisions are only possible when the neutron energy is greater than the nuclear level it excites the nucleus to [134]. Inelastic scattering with carbon usually results in the emission of 4.81 MeV gamma rays. Many nuclear reactions such as neutron capture are associated with lower energy (thermal) neutrons, but the threshold reactions ^{12}C(n, p)^{12}B , ^{12}C(n, α)^{9}Be, ^{12}C(n, d)^{11}B and ^{12}C(n, t)^{10}B become possible with neutron energies above approximately 6.5 MeV [135].

The effectiveness of a detector material is largely affected by its efficiency for detecting the particle. The efficiency is linked to both the probability that the neutron will interact with the scintillator and the size of the scintillator. The probability distribution for interaction $P(x)$ at a function of scintillator thickness x is described by:

$$P(x) = 1 - e^{-\frac{1}{\lambda}\cdot x} \qquad \lambda = \frac{1}{\Sigma_{tot}} \tag{3.3}$$

where λ is the average distance travelled by the neutron before it's first interaction in the scintillator, known as the mean free path [132].

For a scintillation detector to be effective the scintillator needs to be thick enough that the recoil protons can deposit all of their energy and an edge can be seen in the response function. The range of a charged particle is the distance that the particle has to travel to deposit all of its energy. The range, described by the Bethe-Bloch equation [136], is dependent on the charge and energy of the particle and the density of the material.

3.1.2 Gamma ray interactions in organic scintillators

Gamma rays have three main interaction mechanisms: photo-electric absorption, Compton scatter and pair production [132]. In organic scintillators gamma rays interact primarily through Compton scatter, since the cross section for photoelectric absorption and pair production are very low for low Z nuclei.

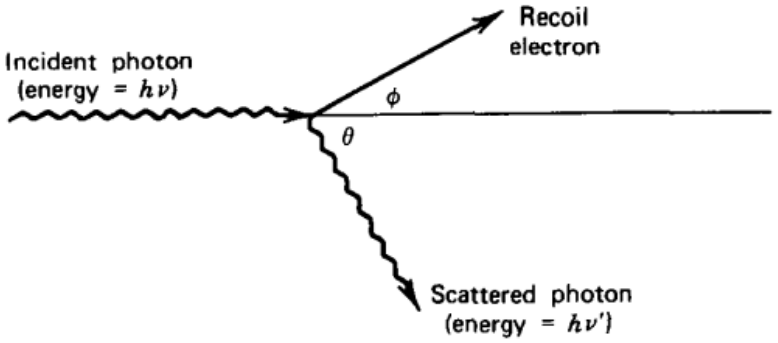

Figure 3.4: Illustration of a photon with energy $h\nu$ undergoing Compton scatter with the recoil electron scattered through the angle ϕ and the scattered photon through the angle θ [137].

Compton scattering is the deflection of a photon from its original direction due to a collision with an electron in the material. During the collision the photon transfers a portion of its energy to the recoil electron. The amount of energy transferred is related to the the angle at which the photon is deflected θ, shown in Figure 3.4. The energy E' of the scattered photon can be written in terms of θ and the incident energy, E, of the photon:

$$E' = \frac{E}{1 + \frac{E}{m_e c^2}(1 - cos\theta)} \tag{3.4}$$

where $m_e c^2$ is the rest mass energy of the electron (511 keV). The maximum energy is deposited when $\theta = 180°$, leading to a Compton edge.

The measured response due to Compton scatter is a continuum that distinctly drops off at the Compton edge energy (E_{CE}) which is given by:

$$E_{CE} = \frac{2E^2}{m_e c^2 + 2E}. \tag{3.5}$$

Compton scatter is not isotropic for most energies, which means the Compton continuum is not rectangular. The probability distribution for θ is given by the differential cross section which is predicted by the Klein-Nishina formula [138], shown in Figure 3.5, and is dependent on photon energy. Figure 3.5 shows that small angle scatters are favoured for gamma rays with energies greater than 1 keV, corresponding to the measured responses having higher contributions at lower energies.

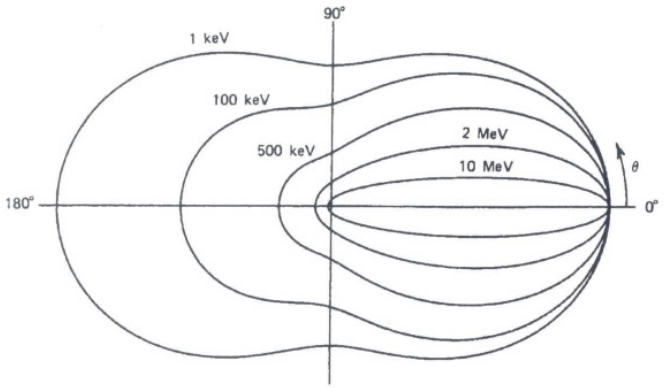

Figure 3.5: Polar plot of the differential cross section as predicted by the Klein-Nishina formula [139].

3.2 Photomultipliers

To utilise scintillators the scintillation photons need to be detected and converted to an electric signal. The most common method of doing this is through the use of a photomultiplier tube (PMT), a device which has been used since the 1940's [140]. PMTs are composed of a photosensitive window and multiple dynodes, which are operated at high voltage [141]. The electrons which are produced by the photosensitive window through the photo-electic effect are multiplied at the dynodes through secondary electron emission to produce an electrical pulse [142].

The explosion of research in solid-state physics has lead to the development of many semiconductor based analogs to the PMT; the most successful being the silicon photomultiplier (SiPM), which was invented roughly 25 years ago [143, 144]. SiPMs are semiconductor structures made up of an array of microcells (typically between 100 and 1000 per mm^2), each consisting of a Single Photon Avalanche Diode (SPAD) [145]. A

SPAD is made up of silicon with a p-n junction [146]. When a photon travels through the silicon it is absorbed, transferring its energy to a bound electron, causing the electron to move from the valence band to the conduction band and creating an electron-hole pair. By applying a reverse bias, the charge carriers are accelerated to the anode if they are holes (positively charged) and to the cathode if they are electrons (negatively charged). The bias applied must be high enough to accelerate the charge carriers to a kinetic energy that it is sufficient for creating secondary charge pairs through impact ionisation and creating a cascade of secondary charge pairs. The minimum bias that can be applied for this to happen is known as the breakdown voltage. The breakdown voltage is typically around 24 V and an operating bias 10-25% higher than the breakdown voltage (over voltage) is typically used, however the recommended overvoltage varies for different products. A quenching resistor is placed in series with each SPAD, to limit the current drawn by the diode and halt the avalanche by bringing the bias below the breakdown voltage, producing a pulse. The diode then recharges back to the operating voltage (which is above the break down voltage) and is ready to detect photons again.

In addition to the break down voltage, the two most important operational characteristics of the SiPM are the photo-detection efficiency (PDE) and noise [147]. PDE is the ratio between the average number of incident and detected photons and depends heavily on the wavelength of the incident photons [148]. It is therefore very important to have a scintillator that produces photons that are within the optimum range of wavelengths for the SiPM. The primary source of noise in these devices is dark current or dark count rate, which is the number of events that are triggered in dark conditions. The events are typically due to thermally generated electrons initiating charge avalanche in the active region of the SAPD and is therefore strongly dependent on the temperature of the environment, where higher temperatures are associated with a higher signal-to-noise ratio. Both the dark current and PDE are also dependent on the over voltage that the SiPM is operated at. Operating at high over voltages increases the PDE but also increases the dark current.

3.3 Time-of-flight

Time-of-flight (ToF) [149] is a commonly used technique for determining the energy spectrum of a neutron beam. The technique requires a ns-pulsed beam and is therefore confined to the laboratory environment. The ToF parameter T is the time it takes a particle to travel from the source to the detector; and is calculated by determining the time difference between a reference pulse which is associated with the pulsing of the neutron beam at the source and the pulse produced by an event within the detector [150].

From the ToF the energy of the neutrons E_n can be calculated using the relativistic kinetic energy equation [151]:

$$E_n = (\gamma - 1)m_n, \qquad \gamma = \frac{1}{\sqrt{1 - (\frac{v_n}{c})^2}}, \qquad v_n = \frac{l}{T}, \tag{3.6}$$

where γ is the Lorentz factor, m_n is the rest mass of the the neutron, c is the speed of light and and v_n is the velocity of the neutron which can be calculated using the known distance l between the detector and the source and the ToF of the neutron T.

3.4 Unfolding

Spectrum unfolding is an alternative method for determining the energy spectrum of a neutron field and is typically used when ToF measurements are not possible. The measured light output spectrum $\frac{dN}{dL}$ can be described as the convolution of the energy spectrum of the incident radiation $S(E)$ and the inherent mono-energetic response functions of the detector system, as indicated by Eq. 3.7; where $R(L, E)$ is the response function for energy E as a function of light output L [152].

$$\frac{dN}{dL} = \int R(L, E)S(E)dE. \tag{3.7}$$

Unfolding is the process of de-convolving the measured neutron light output spectrum with mono-energetic response functions to produce an energy spectrum. These algorithms require a matrix of response functions $R(E, L)$ defined over the measured energy range, a default energy spectrum $S_{def}(E)$ and the measured neutron light output spectrum. The response matrix is a collection of the detector response to mono-energetic neutrons. It is vital that the response functions are well defined and accurate to the detector response as they are highly detector specific. For neutron energies below 20 MeV the response functions can be simulated, however above 20 MeV the neutron data libraries are not accurate for all reaction channels [153] and response functions must be measured [154, 155]. The default energy spectrum is used as an initial approximation for the energy distribution and should be a good estimate of the source distribution. The measured neutron light output spectrum needs to be calibrated using the same scale as the response functions and typically requires a large number of measured events.

Chapter 4

Methodology

A compact spectrometer consisting of an EJ-276 plastic scintillator coupled to a single SiPM was built and characterised in neutron fields between 5.000 MeV and 62.5 MeV at the n-lab, University of Cape Town, the AMANDE facility, IRSN Cadarache, and the D-line neutron facility at iThemba LABS. The performance of the compact spectrometer was compared at each facility to a standard organic liquid scintillator coupled to a PMT. The data from all detector systems were acquired using an identical digital data acquisition system. In this chapter the design of the compact detector, the digital data acquisition system and the facilities used to characterise the spectrometer are discussed in addition to the digital pulse processing and methods of neutron spectroscopy.

4.1 Compact Detector System

The EJ-276 [156] scintillator is a plastic scintillator manufactured by Eljen Technologies which is capable of pulse shape discrimination and has been extensively studied and characterised over a wide range of neutron energies [28, 32, 157, 158]. This scintillator has the advantages of being non-toxic, robust and easily customisable in shape and size, however it does not perform as well as the liquid organic scintillators with respect to PSD quality and detection efficiency [159]. The properties of this scintillator in comparison to those of a standard liquid scintillator (EJ-301 or equivalent) are summarised in Table 4.1.

The SensL MicroFC-60035 C-series SiPM [160], shown in Figure 4.1 (a), has an active area of 6×6 mm^2 consisting of 18980 microcells, each with dimensions $35\times$ 35 μm^2. The SiPM was mounted to an evaluation board with dimensions 4.0×3.7 cm^2 which features three ports: the input, fast output and slow output. Figure 4.1 (b) shows a simplified circuit diagram of the SiPM and the individual microcells. Each microcell also has a fast output and a slow (anode-cathode) output and therefore the slow output from the SiPM is made up of the sum of the anode-cathode pulses from all of the microcells. The microcells operate in Geiger mode [161], meaning they produce the same output regardless of the energy of the photon. Since the pulse from the SiPM is the sum of the signals from all

of the individual microcells, the size of the pulse from the slow output of the SiPM is proportional to the number of photons detected. The pulse from the fast output is the derivative of the internal fast switching of the microcell in response to the detection of a single photon and can be used for applications requiring fast timing, however it was not used in the presented work. The break down voltage for this SiPM is approximately 24.5 V and for optimum performance an operating bias of +28.5 V (overvoltage of 16%) was used, supplied by a BK Precision 1550 power supply [162]. The optimum overvoltage was determined in previous work [29].

Table 4.1: The scintillation and atomic properties of the EJ-276 plastic scintillator [156] and EJ-301 liquid scintillator [163].

Properties	**EJ-276**	**EJ-301**
Light output (% Anthracene)	56	78
Scintillation efficiency (photons/1 MeV$_{ee}$)	8600	12000
No. of H atoms per cm^3 ($\times 10^{22}$)	4.546	4.82
No. of C atoms per cm^3 ($\times 10^{22}$)	4.906	3.98
No. of electrons per cm^3 ($\times 10^{23}$)	3.533	2.27

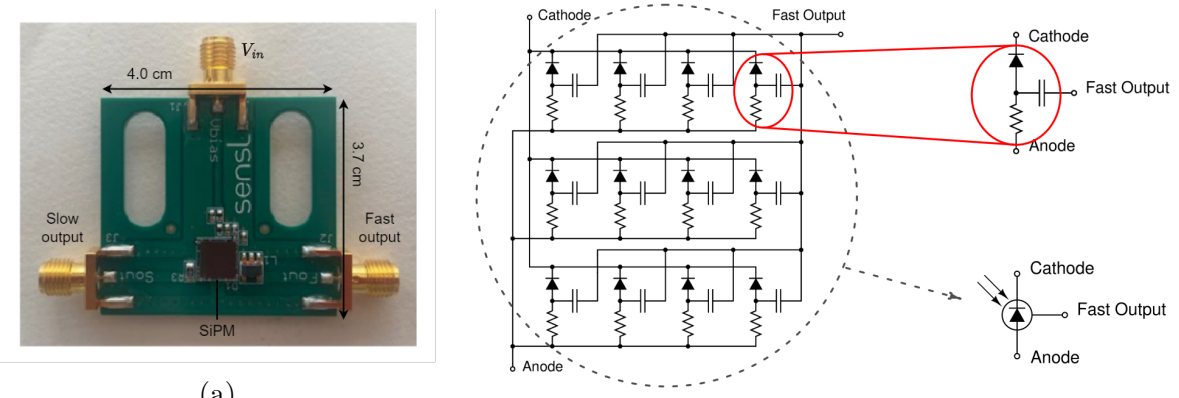

(a) (b)

Figure 4.1: (a) The SensL C-series silicon photomultiplier mounted to the evaluation board. The input (V_{in}), slow output and fast output are indicated, as are the dimensions of the board. (b) Simplified circuit diagram of a silicon photomultiplier. The section circled in red highlights the circuit for a single microcell within the array.

A digital data acquisition system consisting of a CAEN DT5730 desktop digitiser [164] and custom open-source acquisition software QtDAQ [29], which was developed at UCT, was used to acquire all of the data presented in this work. This acquisition system has been tested and found to be a suitable alternative to the traditional analogue systems for neutron metrology [30]. The DT5730 desktop digitiser, shown in Figure 4.2, is an 8-channel, 14-bit digitiser with a sampling rate of 500 MS/s and features a Programmable Gain Amplifier (PGA) which allows for a voltage range of either 0.5 V$_{pp}$ or 2.0 V$_{pp}$.

Acquisition can occur on all channels simultaneously and can be programmed to trigger on any of the channels. There are various trigger schemes available, however in this work the digitiser was set to trigger on absolute voltage threshold crossing. The pulses from the detector systems are acquired in list mode through either a USB-2.0 connection to a laptop or an Optical Link to a PC with an A3818 PCI express CONET2 controller. The digitiser can perform onboard digitised pulse analysis, however acquiring the full digitised pulse for each triggered event provides flexibility for offline analyses, which was necessary for this work. In the presented work the analysis of the acquired digitised pulses was performed post-acquisition using a series of custom-built Python scripts.

Figure 4.2: The CAEN DT5730 desktop digitiser.

Figure 4.3 (a) shows a schematic of the compact detector. The $6 \times 6 \times 120$ mm^3 EJ-276 scintillator was wrapped in a diffuse reflector and coupled to a single SensL C-series SiPM using optical gel. A specular reflecting material was used to cover the opposite end of the scintillator. The components were housed in a light tight covering consisting of an aluminum tube covering the scintillator with a 3D printed casing containing the SiPM, shown in Figure 4.3 (b). The pulses were acquired from the slow output using the digital data acquisition system. The dimensions of the scintillator ($6 \times 6 \times 120$ mm^3) were chosen such that the profile of the scintillator matched the 6×6 mm^2 profile of the SiPM and the length of the scintillator was chosen to optimise both the energy deposition of 100 MeV neutrons and the light collection of the scintillation photons. The mean free path of 100 MeV recoil protons in EJ-276 was calculated to be approximately 9 cm [165], which defines the minimum length of the scintillator. By having a scintillator longer than this value the number of recoil protons that escape before depositing their full energy can be considerably reduced. The longer the scintillator, the more neutron interactions, and hence energy deposition, can occur producing scintillation photons. However, a longer scintillator has poor light transport characteristics since the scintillation light has to travel further to be detected, scattering and attenuating as it moves through the scintillator. The optimum scintillator length for the 6×6 mm^2 profile was determined to be 12.0 cm using a GEANT4 simulation which is discussed in more detail in Appendix A.

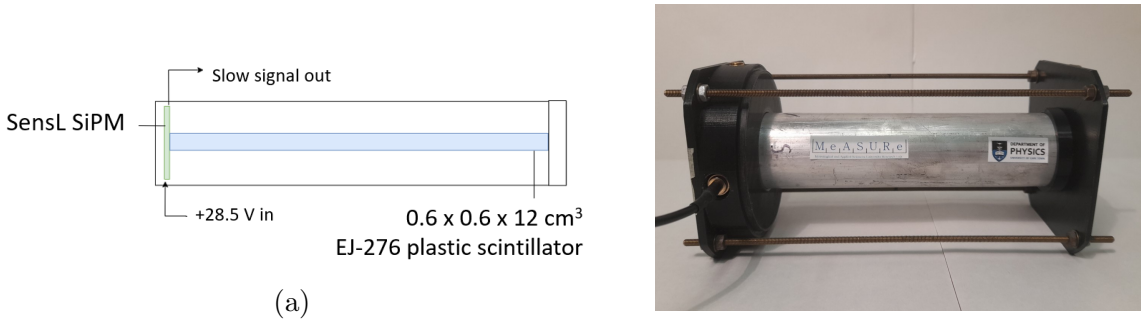

Figure 4.3: (a) Schematic of the compact spectrometer. (b) The compact neutron spectrometer where the scintillator is encased in an aluminium tube to minimise light leakage, and coupled to the SiPM (left) housed in a 3D printed casing.

4.2 Facilities and Measurements

4.2.1 The n-lab, University of Cape Town

The n-lab is a fast neutron facility within the Metrological and Applied Science University Research Unit (MeASURe) at the UCT Department of Physics [166, 167, 168]. The facility, which is illustrated in Figure 4.4, features a Thermo MP-320 sealed tube neutron generator (STNG) and a 220 GBq radioisotopic ^{241}Am-^{9}Be (AmBe) source, which are located in a high density polyethylene (HDPE) vault. In this work, the STNG and a lower activity AmBe source (2.2 GBq) were used, in addition to several gamma ray calibration sources. The reference detector used at this facility is a 5 $\varnothing$ $\times$ 5 cm^3 EJ-301 organic liquid scintillator [163] coupled to a 12-stage PMT.

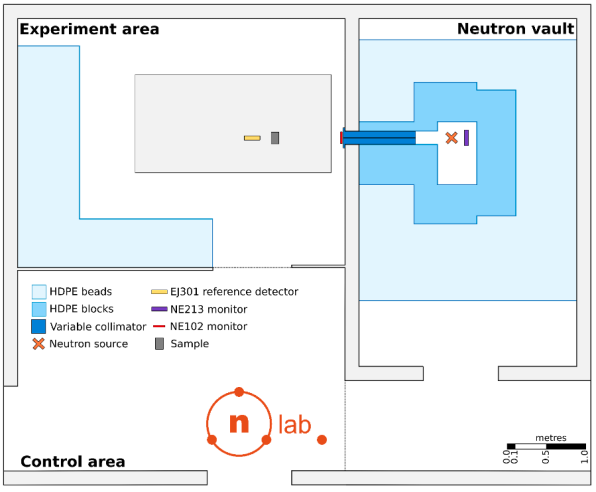

Figure 4.4: Schematic of the n-lab facility at UCT showing the neutron vault, experimental area and control room.

The STNG produces 14.1 MeV neutrons via the deuterium-tritium fusion reaction. The 14.1 MeV neutrons are accompanied by 2.2 MeV gamma rays produced by neutron capture on hydrogen and 4.4 MeV gamma rays produced from elastic scatter of the neutrons on ^{12}C in the HDPE shielding. The energy spectrum of the neutrons produced is shown in orange in Figure 4.5. Measurements of the radiation field produced by the STNG were performed with both the EJ-276 compact detector and EJ-301 reference detector with the collimator set to 8.0 mm in diameter at the beam exit. Both detectors were placed in the experiment area shown in Figure 4.4, in line with the collimator opening. The compact detector was placed 0.86 m from the colllimator opening and the reference detector was placed at 1.23 m.

The radioisotopic source AmBe is commonly used as a gamma ray and neutron source and decays via the scheme illustrated in Eq. 4.1. The ^{241}Am isotope decays to ^{237}Np via alpha decay. The alpha particles and ^{9}Be then undergo an (α, n) reaction to produce neutrons and an excited ^{12}C atom. The de-excitation of the ^{12}C nucleus results in the emission of a 4.4 MeV gamma ray [169]. The neutrons produced have energies ranging up to 11 MeV, with the distribution shown in blue in Figure 4.5, with an average neutron energy of 4.3 MeV.

$$\begin{aligned} {}^{241}\mathrm{Am} &\rightarrow \alpha + {}^{237}\mathrm{Np} \\ \alpha + {}^{9}\mathrm{Be} &\rightarrow \mathrm{n} + \gamma + {}^{12}\mathrm{C} \end{aligned} \tag{4.1}$$

The (α, n) reaction occurs roughly 70 times per 10^6 alpha particles [170], thus the 2.2 GBq AmBe source used in this work has a neutron emission rate of approximately 1.5×10^5 neutrons per second into 4π steradians. Since the gamma rays and neutrons are produced in approximately equal amounts, the gamma ray emission rate is assumed to be the same as the neutron emission rate.

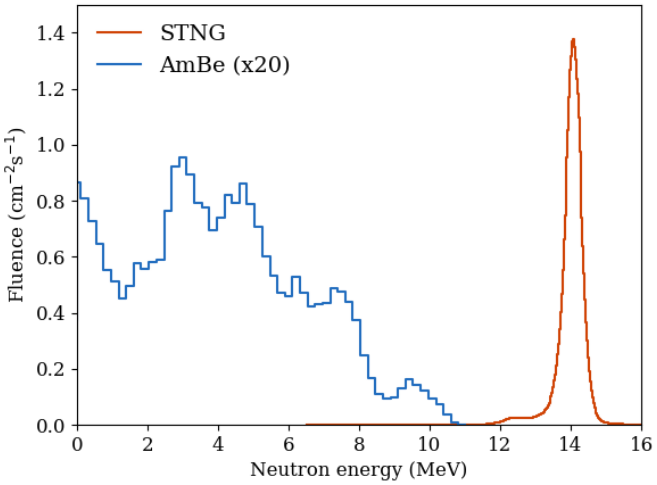

Figure 4.5: Neutron energy spectra produced by the AmBe source and sealed tube neutron generator (STNG) measured with a 5 ⌀ × 5 cm^3 EJ-301 liquid scintillator [171].

Measurements of the radiation field from the radioisotopic sources were performed with both detectors with the sources placed against the front face (opposite end to the SiPM) of the detector. For all measurements performed at this facility the EJ-301 reference detector was operated at a voltage of -1.1 kV and the compact detector was operated at +28.5 V.

4.2.2 AMANDE, IRSN Cadarache

The Accelerator for Metrology and Neutron Applications for External Dosimetry (AMANDE) facility [172] of the Institut de Radioprotection et de Sûreté Nucléaire (IRSN) in France provides monoenergetic neutron fields between 2 keV and 20 MeV. The neutron fields are produced by accelerating proton or deuteron ions to a given energy using a 2 MV HVEE Tandetron [173] onto a target of either deuterated or tritrated titanium. The beams can be operated in pulsed mode, delivering 6 ns wide pulses at 500 ns intervals, allowing for measurements of neutron time-of-flight (ToF). This facility features a 5 $\varnothing\times$ 5 cm^3 BC-501A organic liquid scintillator [174] and 12-stage PMT reference detector. BC-501A is an equivalent scintillator to EJ-301 (and NE-312).

The experiment hall, shown in Figure 4.6, was designed to minimise the production of secondary radiation from neutron scattering in the surrounding environment. The movable arms feature an automated transport system allowing for accurate and repeatable placement of detectors at any distance between 0.5 m and 6.0 m away from the target and at any angle between -160° and +160° relative to the incoming ion beam.

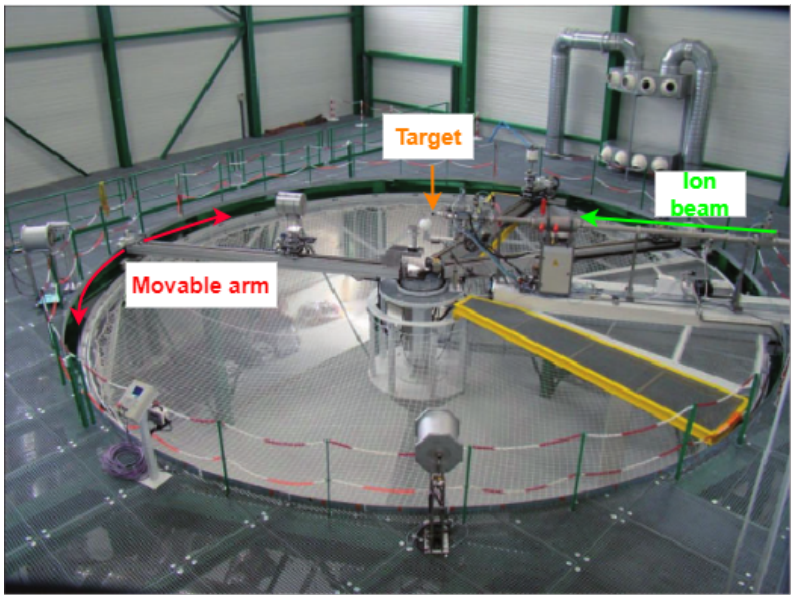

Figure 4.6: The experimental hall at the AMANDE neutron facility at the IRSN in Cadarache [175].

The neutrons are produced in the entire solid angle, however the angle at which the neutron leaves the target is related to its energy such that a unique neutron energy is observed at a defined angle. At 0° from the beamline the energy of the neutrons is at a maximum.

Table 4.2 details the experimental conditions of measurements of the neutron field that were performed with the EJ-276 compact detector and the BC-501A reference detector. The detectors were secured to the movable arm shown in Figure 4.6, which was positioned at 0° relative to the incoming ion beam. The detector positions on the movable arm are shown in Table 4.2, where the distance specified is between the target and the end of the detector closest to the target. At 5.000 MeV reference pulses associated with the ns-pulsed ion beam on the target were simultaneously acquired on a second channel for time-of-flight analyses.

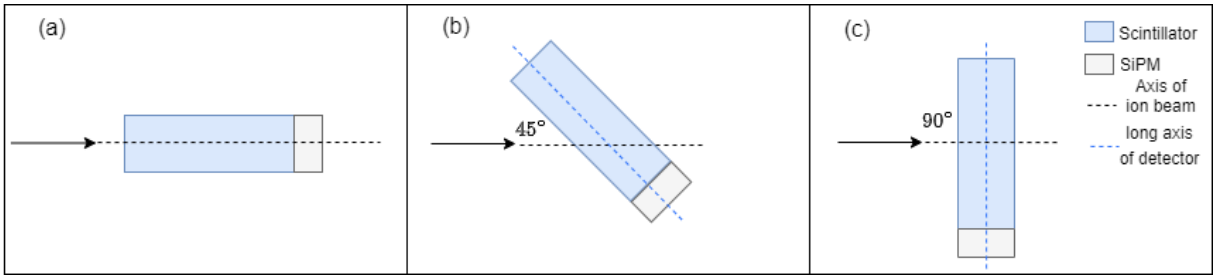

Figure 4.7: Diagrams of the detector orientations at (a) 0°, (b) 45° and (c) 90° relative to the ion beamline.

Table 4.2: Summary of the experimental conditions for the neutron field measurements made with the BC-501A reference and EJ-276 compact detectors at the AMANDE facility at the IRSN. The entries marked with ∗ are featured in Appendix C, and the entries marked with † utilised a pulsed beam for ToF.

					Reference Detector			**Compact Detector**		
Ion beam	**E_{ion} (MeV)**	**Target**	**Target thickness (µg cm^{-2})**	**$E_{n,\,max}$ (MeV)**	**Beam Intensity (µA)**	**Distance (m)**	**Voltage (kV)**	**Beam Intensity (µA)**	**Distance (m)**	**Detector angle (degrees)**
*deuteron	0.432	TiD	793	3.225	2.0	1.808	-1.93	2.0	0.655	0
†deuteron	1.841	TiD	793	5.000	3.6	2.058	-1.93	3.2	2.208	0
*deuteron	3.777	TiD	793	7.000	1.0	1.808	-1.93	3.1	1.652	0
triton	0.432	TiT	776	15.100	1.9	1.808	-1.80	2.0	0.655	0
								1.8	0.655	45
								1.8	0.655	90

For the majority of the measurements the detectors were oriented with the axis of the detector in line with the axis of the ion beamline, as shown in Figure 4.7 (a). Two measurements were performed with the compact detector rotated to test the directional sensitivity. The angle specified is between the axis of the ion beam and the detector, as shown in Figure 4.7 (b) and (c).

In addition to those shown in Table 4.2, measurements of AmBe and ^{207}Bi sources were also performed for calibration purposes, with the sources placed very close to the detector face.

4.2.3 The D-line at iThemba LABS

iThemba Laboratory for Accelerator-Based Sciences (LABS) is the largest accelerator facility in the southern hemisphere [176] and where there exists a fast neutron facility, D-line, which can deliver quasi-monoenergetic neutron beams with energies between 30 MeV and 200 MeV. Protons accelerated by the separated sector cyclotron (SSC) are directed onto a ^{nat}Li target (typically) to produce neutrons through the ^{7}Li(p,n)^{7}Be reaction. A beam pulse selector is used to suppress a fraction of the proton bunches [33] such that a pulsed neutron beam with 1 ns wide pulses 500 ns apart [177] is delivered allowing ToF measurements to be taken. A schematic of the neutron vault is shown in Figure 4.8. A 2.0 m thick steel collimator allows for measurements at 0° and 16° relative to the direction of the proton beam and produces beams with a 10 cm × 10 cm profile at 8.0 m from the target. The facility was recently upgraded in terms of the beam delivery system and vault geometry and is in the process of being characterised [178].

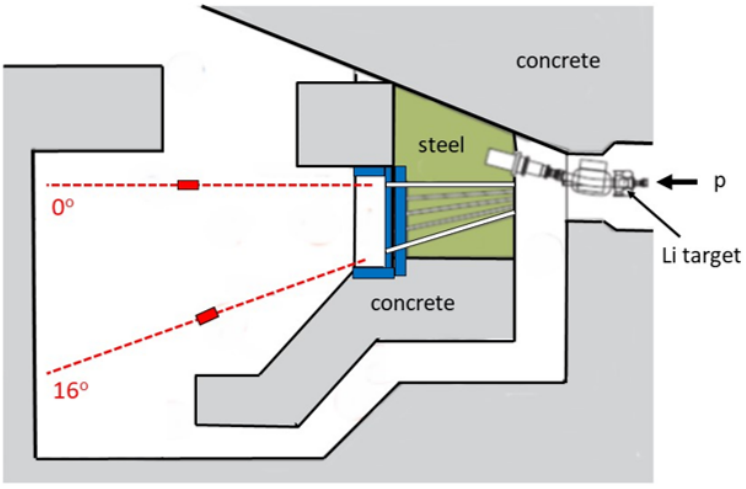

Figure 4.8: Schematic of the neutron vault at the iThemba LABS fast neutron facility. The 0° and 16° beam lines are indicated by the dashed lines, with standard neutron measurements at 8.0 m from the Li target, indicated by the red boxes.

The neutron emission spectra from 100 MeV protons on a Li target at 0° and 16° are shown in Figure 4.9. At both angles the spectra feature a high intensity mono-energetic peak from the ^{7}Li(p, n)^{7}Be reaction with an energy equal to the energy of the proton minus the Q-value of the reaction (1.664 MeV) and the average energy loss of the proton in the Li target. The peak is accompanied by a continuum of neutrons extending from low energies up to the peak energy which are produced by break-up reactions in the Li target. The ^{7}Li(p,n)^{7}Be reaction is strongly forward biased while the break-up reactions are mostly isotropic, therefore the largest difference in neutron emission at 0° and 16° is the intensity of the high energy neutron peak.

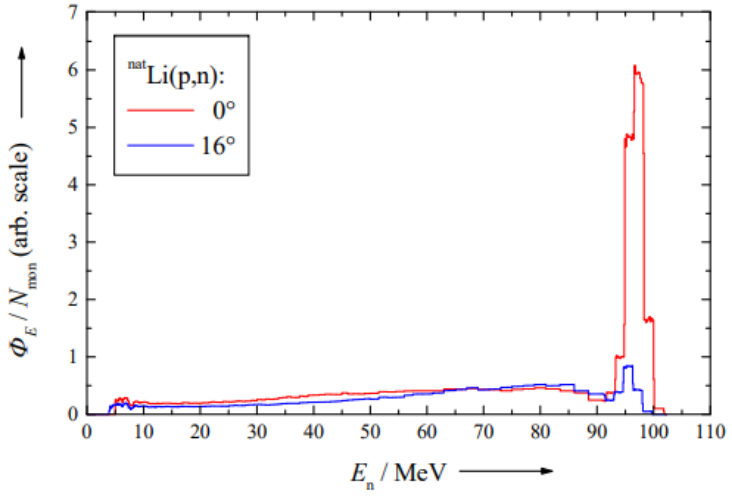

Figure 4.9: Normalised spectral neutron distributions measured with a BC-501A detector at 8.0 m at 0° and 16° for a 100 MeV proton beam incident on a 6.0 mm thick Li target [33].

Measurements of the neutron field produced by 66.0 MeV protons on an 8.0 mm thick Li target were performed using the compact detector and the reference detector, consisting of a 5 ⌀ × 10 cm^3 BC-501A liquid scintillator coupled to a 12-stage PMT [177]. The detectors were placed in the 16° beamline with the end of the compact detector closest to the target at 8.04 m and the reference detector at 8.13 m from the target. The average energy loss in the target was calculated to be 1.793 MeV [165], where the average energy loss was considered to be half of the energy loss in the 8.0 mm thick target. In these conditions neutron energy spectrum has a peak at 62.5 ± 0.2 MeV. The reference pulses associated with the ns-pulsed proton beam on the target were simultaneously acquired on a second channel for time-of-flight analyses. Additionally, measurements of an AmBe source were made with both detectors for calibration purposes.

4.2.4 Summary

The measurements performed on the neutron fields detailed in Table 4.3 are presented and analysed in detail in this thesis. Additionally, at all three facilities, measurements of gamma rays with known energies were made with both the reference detector and the compact spectrometer for the light output calibration. Table 4.4 summarises the sources used for the calibration measurements for each detector at the three facilities.

Table 4.3: The neutron measurements performed at the n-lab, AMANDE and iThemba LABS fast neutron facilities.

Facility	**$E_{n(max)}$ (MeV)**	**Field type**	**ToF**
AMANDE	5.000	monoenergetic	yes
n-lab	14.1	monoenergetic	no
AMANDE	15.100	monoenergetic	no
iThemba LABS	62.5	broad energy range	yes

Table 4.4: The energy and associated Compton edge of the gamma ray sources used for calibration and the facility at which the sources were used. The $^{12}C^{*}$ gamma ray emission is associated with the AmBe source.

Source	**Gamma ray energy (MeV)**	**Compton edge energy (MeV)**	**Facility**
$^{12}C^{*}$	4.44	4.20	n-lab, AMANDE, iThemba LABS
^{207}Bi	1.77 1.06 0.57	1.55 0.86 0.39	AMANDE
^{22}Na	1.27 0.51	1.06 0.34	n-lab
^{54}Mn	0.83	0.64	n-lab
^{137}Cs	0.66.0	0.48	n-lab

4.3 Digital Pulse Processing

The DT5730 acquisition system triggers when the absolute voltage exceeds the set threshold and acquires the entire raw pulse, an example of which is shown in Figure 4.10. The energy deposited in the detector is proportional to the integral of the digitised pulse. The pulses therefore need to be digitally integrated over equivalent time scales. Additionally, the digitised pulses must have equivalent baseline voltages.

The baseline of each digitised pulse was determined by taking the mean value of the samples preceding the sharp change in voltage, which in Figure 4.10 are the samples from t = -200 ns to 0 ns. To account for variations in baseline voltage, this was subtracted from each digitised pulse.

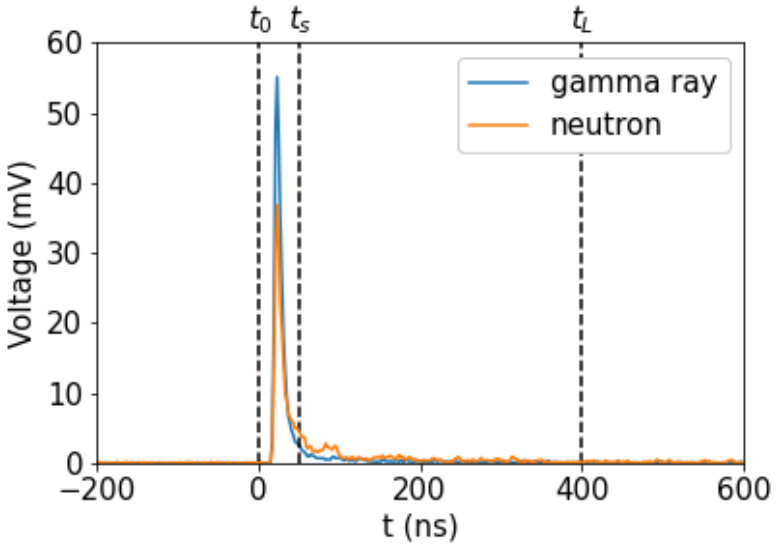

Figure 4.10: Sample digitised pulses for gamma ray and neutron induced events with equivalent long integrals after being aligned with respect to voltage baseline and time, measured with a BC-501A detector and acquired by the CAEN DT5730 digitiser. The plot includes the digital integration gates (t_0, t_S and t_l) [30].

The triggering mechanism of the digitiser results in pulses which are not consistently aligned in time. To ensure the signals are integrated over equivalent time intervals, a digital constant fraction discriminator (CFD) filter of the form:

$$v_i = \sum_{j=1}^{N} (fV_{i-j} - V_{i-j-D}) \tag{4.2}$$

was applied to the digitised pulses. Where v_i is event i after having the CFD filter applied, N is the the filter length, f is the filter fraction, D is the filter offset and V is the unfiltered pulse. The parameters $N = 6$ samples, $D = 6$ samples and $f = 0.75$ were used [30]. The CFD filter is applied after subtracting the baseline.

Figure 4.11 shows a typical pulse before and after the CFD filter is applied. By assuming linear interpolation between samples, the time of zero crossing t_{cfd} for the CFD filtered pulse can be found by taking the weighted average of the samples on either side of the zero voltage line. The start time t_0 of the pulse is defined relative to t_{cfd}. In this work the start time t_0 was defined to be $t_0 = t_{cfd} - 40$ ns. The short and long integration times, t_S and t_L respectively, were then defined relative to t_0.

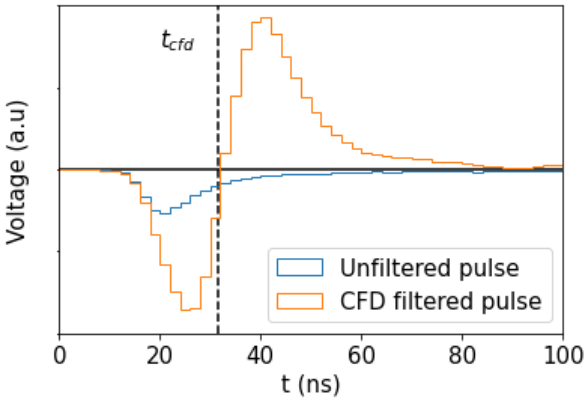

Figure 4.11: A typical digitised pulse before and after the application of the CFD filter, showing the the time of zero crossing t_{cfd} for the filtered pulse.

4.3.1 Light output parameter

The long integral parameter Q_L is a measure of the charge in the digitised pulse and is linearly related to the light output parameter L according to:

$$Q_L = ML + C \tag{4.3}$$

where M is the gradient and C is the y-axis intercept which is expected to be zero. The long integral parameter Q_L is determined by integrating the digitised pulse between t_0 and t_L as shown in Figure 4.10. The long integration time is chosen to include the majority of the pulse and also optimise the quality of PSD, which is discussed in more detail in Section 4.3.3. The parameters M and C are determined through a calibration of the detector response to gamma rays. Table 4.4 shows a list of calibration gamma rays used in this work and their associated Compton edge energies. The light output parameter L is also linearly related to the energy deposited in the scintillator and by convention:

$$L = E_\gamma \tag{4.4}$$

where E_γ is the energy deposited by a gamma ray interaction. The parameter L therefore has the units of energy (MeV) for recoil electrons. As discussed in Chapter 3, events from recoil electrons produce a different light output to events from heavier recoil charged particles associated with neutron events. Since the same calibration scale is used for the neutron light output parameter the units are denoted as MeV_{ee} (MeV electron equivalent).

Since Compton scatter is the primary interaction channel for gamma rays in organic scintillators, the Compton edge of the gamma ray spectrum which has a defined energy is used for the calibration. Figure 4.12 demonstrates the method used to determine the position of the Compton edge in this work. The Compton edge was fitted to a half Gaussian distribution and the Q_L value at half-height of the distribution, calculated as the centroid value μ plus half of the full width half maximum $\frac{FWHM}{2}$, was used to define the location of the Compton edge.

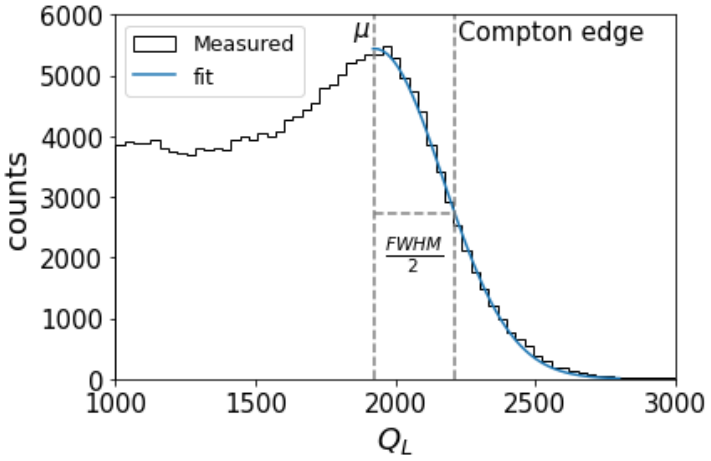

Figure 4.12: Half Gaussian distribution fitted to the edge of the Compton continuum of the long integral spectrum for the gamma rays produced by ^{137}Cs measured with an EJ-301 organic liquid scintillator. The centroid value μ, half of the full width half maximum $\frac{FWHM}{2}$ and position of the Compton edge ($\mu + \frac{FWHM}{2}$) are indicated.

In instances where there are three or more points for the calibration the parameters M and C are determined through a weighted Levenberg-Marquardt linear fit. Figure 4.13 (a) shows the typical long integral spectra 4.13 (b) demonstrates how these spectra are calibrated using a linear fit.

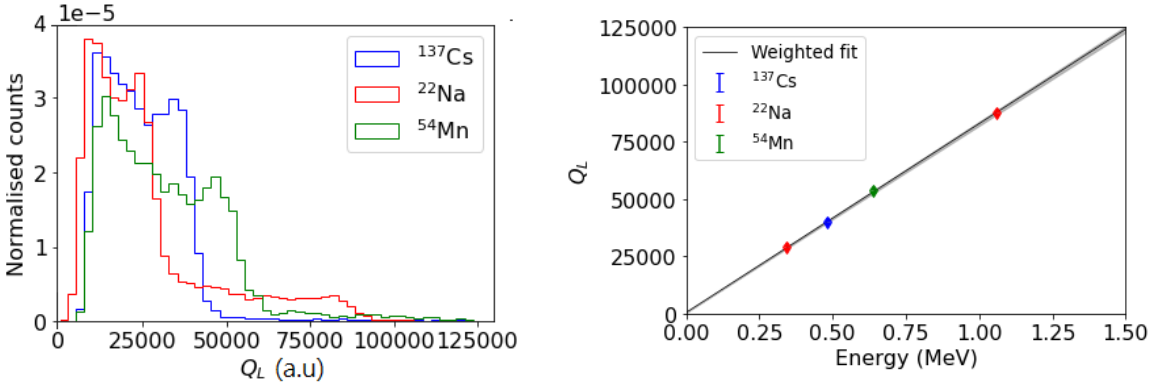

(a) (b)

Figure 4.13: (a) The uncalibrated long integral spectra and (b) weighted linear fit of the long integral (Q_L) of the Compton edge as a function of energy for measurements of the gamma ray emissions of ^{137}Cs, ^{22}Na and ^{54}Mn taken at the n-lab with the compact spectrometer. The parameters of the fit being $M = 82464 \pm 880$ MeV^{-1} and $C = 488 \pm 543$.

However, when less than three points are available for calibration performing a weighted fit is not possible. In these cases C is assumed to be zero and M is calculated using:

$$M = \frac{Q_L}{E_\gamma} \tag{4.5}$$

for each calibration point. The uncertainty of M is associated with the uncertainty on the Q_L of the Compton edge determined by the fit. The average M value, weighted according to uncertainty, is then taken.

4.3.2 Pulse shape parameter

The scintillation produced by certain organic scintillators, such as EJ-301 and EJ-276, consists of both a fast and slow decay component [179]. The relative intensity of the two components depends strongly on the particle species inducing the scintillation. In these organic scintillators the difference in relative intensities of the fast and slow component differ significantly for different particle species, a quality that can be used to distinguish the types of events from each other using a technique known as pulse shape discrimination (PSD). Figure 4.10 shows the difference in the waveforms of neutron and gamma ray events with the same light output.

There are many methods of PSD [180, 181, 182, 183, 184, 185], each with their own advantages and disadvantages . In this work the charge comparison method was used [31] and implemented post-acquisition. This method is commonly used in digital signal processing due to its short computational time [186] and excellent performance at energies above 0.8 MeV_{ee} [187]. Digital charge comparison uses the ratio between the integral of the pulse over a short and long time interval to define the pulse shape parameter S in the form:

$$S = k\frac{Q_S}{Q_L} + c \tag{4.6}$$

where Q_S and Q_L are the integrals of the pulse over the short and long time intervals (t_0 to t_s and t_0 to t_L) respectively and k and c are scaling constants. In this work the calculation of S was performed post acquisition to allow for maximum flexibility when determining the optimum values for the integration parameters, the method of which is discussed in detail later. In future versions of the detector, real-time PSD [180, 188, 189] could be implemented with the use of FPGA programming.

Figure 4.10 shows the typical waveforms for neutron and gamma ray induced events. Since electron excitation events induced by gamma ray interaction have a larger fast decaying component they will have a higher S than the interactions from the recoil protons, deuterons, tritons and alpha particles associated with neutron interactions which have a larger contribution from longer lived scintillation processes. The neutron and gamma ray events can therefore be separated according to S. The pulse shape parameter has a

distribution with distinct loci for the different interacting particles, illustrated in Figure 4.14. A cut can be applied to separate the locus associated with the gamma ray events and the locus associated with neutron events.

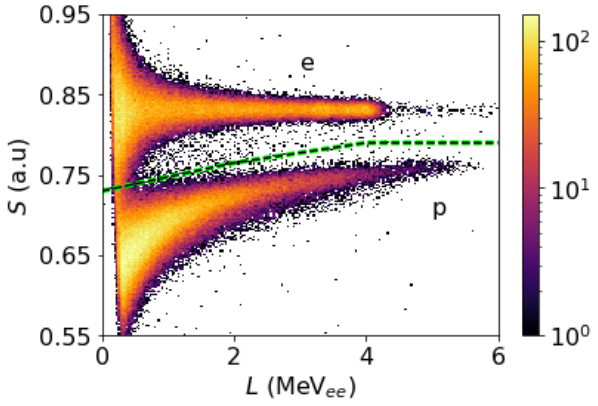

Figure 4.14: Counts as a function of light output parameter L and pulse shape parameter S for events in an EJ-301 liquid scintillator coupled to a PMT when irradiated by the neutron and gamma rays produced by an AmBe source. The events associated with recoil electrons (e) and protons (p) are indicated and the green dashed line indicates the cut used to separate neutron and gamma ray events.

The quality of the PSD can be quantified by fitting a Gaussian distribution to the S spectrum for the two kinds of events, as shown in Figure 4.15, and calculating the figure of merit (FoM) [190]:

$$\text{FoM} = \frac{|\mu_g - \mu_n|}{FWHM_g + FWHM_n} \tag{4.7}$$

where μ_g and μ_n are the centroid values and $FWHM_g$ and $FWHM_n$ are the full width half maxima of the gamma ray and neutron distributions respectively.

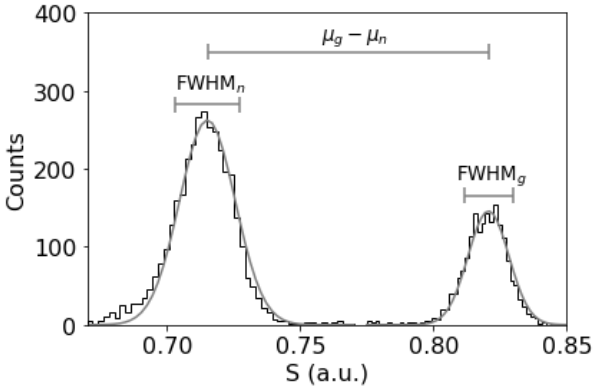

Figure 4.15: The distribution of pulse shape parameter S for events with $2.5 < L < 3$ MeV$_{ee}$ associated with the data set shown in Figure 4.14. Two Gaussian distributions have been fitted to the data and the full width half maxima of the neutron and gamma ray events (FWHM$_n$ and FWHM$_g$) and the difference between the mean values of the gamma ray and neutron ($\mu_g - \mu_n$) distributions are indicated.

4.3.3 Integration parameter optimisation

Figure 4.10 shows the long and short integration times on sample digitised pulses, however these integration times will vary for pulses acquired by different devices. The choice of optimum long and short integration times are made to maximise the quality of pulse shape discrimination (PSD).

The integration parameters were optimised for all three of the reference detectors and the compact detector at each facility using the AmBe measurements. The optimisation process requires one of the integration times to be kept constant whilst the other is varied. For each integration time PSD was performed, the neutrons and gamma ray events were separated using the cuts shown in Figure 4.16 and the FoM was calculated using a subset of the events, indicated by the vertical dashed lines in Figure 4.16. The FoM varies as a function of light output L. In the optimisation of the long gate the variation of the long integration time results in a variation in the relationship between Q_L and L. To ensure that the FoM was calculated with events of equivalent L the lower and upper thresholds of the selection window were chosen to be positioned in the same position relative to the highest Q_L value of the gamma ray spectrum.

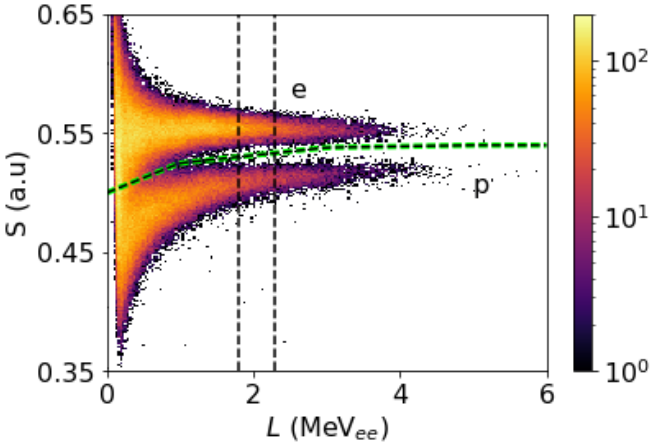

Figure 4.16: Counts as a function of long integral Q_L and pulse shape parameter S for events in the EJ-276 compact spectrometer when irradiated by the neutron and gamma ray field produced by an ^{241}Am-^{9}Be radioisotopic source.

The long integration time was initially set to $t_L = t_0 + 440$ ns for the reference detectors and $t_L = t_0 + 840$ ns for the compact detector, based on the relative pulse durations. The short integration time was varied, as shown in Figure 4.17 (a). The optimum short integration time was then used while the long integration time was varied, which is shown in Figure 4.17 (b). The optimum values determined for t_S and t_L at the three facilities are summarised in Table 4.5.

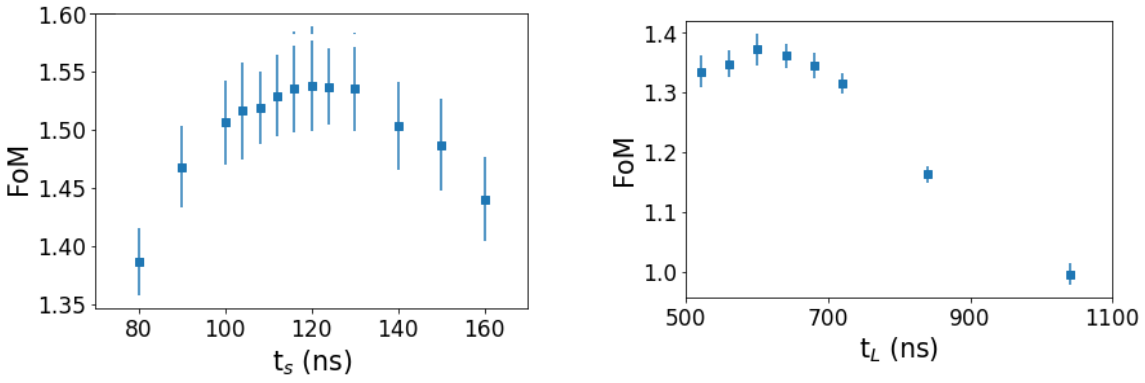

(a) (b)

Figure 4.17: (a) The short integration time t_S as a function of FoM for a long gate of 840 ns. (b) The long integration time t_L as a function of FoM for a short gate of 120 ns. The calculations were performed on measurements of an AmBe source made with the compact detector at the n-lab. The integration times that yield the highest FoM are $t_s = 120$ ns and $t_L = 600$ ns.

Table 4.5: The short and long integration times t_S and t_L used for the digitised pulses from the compact detector acquired at n-lab, AMANDE and iThemba LABS.

	Reference detector		Compact detector	
Facility	t_S (ns)	t_L (ns)	t_S (ns)	t_L (ns)
n-lab	54	340	120	600
AMANDE	48	480	120	450
iThemba LABS	58	340	80	500

A sample of the digitised pulses from the compact and reference detectors at the three facilities is shown in Figure 4.18. The waveform and quality of the pulses acquired using the compact spectrometer, seen in Figure 4.18 (b), varied significantly between the three facilities which accounts for the variation in the optimised t_S and t_L seen in Table 4.5. The poor pulse quality of the data acquired at iThemba LABS is likely the result of the very long signal cables from the neutron vault to the acquisition room. As shown in Table 4.5 both the short and long integration times for the compact detector are longer than those used for the reference detectors since SiPMs produce pulses that decay over longer time scales than those produced by PMTs, which can be seen by comparing the pulses in Figures 4.18 (a) and (b).

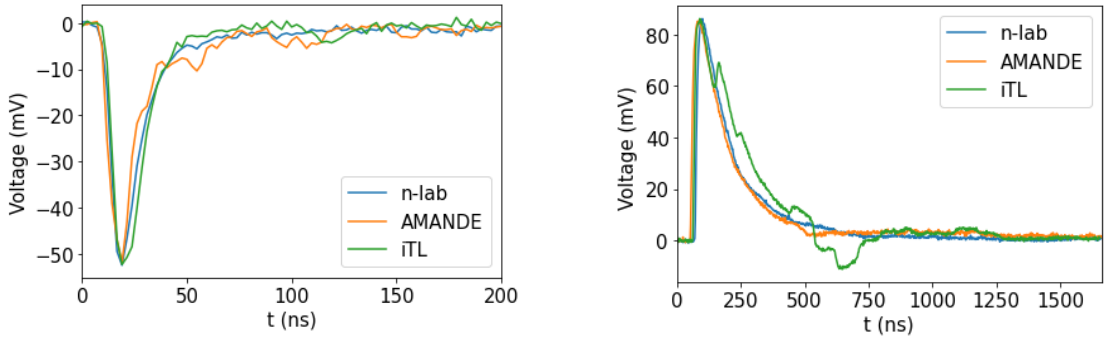

(a) (b)

Figure 4.18: Typical digitised pulses from the (a) reference and (b) compact detectors at n-lab, AMANDE and iThemba LABS (iTL) neutron facilities.

4.4 Neutron Spectroscopy

4.4.1 Time-of-flight

For time-of-flight calculations both the pulses from the detector system and the reference pulses associated with the pulsed ion beam on the target were acquired. The acquisition system was set to acquire when the trigger condition is met on the digitised pulses from the detector system and as a result, the reference pulse of the neutron bunch associated with the detected event was not included in the acquisition window. The parameter τ is defined in terms of the time between the detected event t_{det} and the reference pulse of the neutron bunch after the bunch associated with the detected event t_{ref}:

$$\tau = t_{ref} - t_{det}, \tag{4.8}$$

as illustrated in Figure 4.19 (a), where t_{det} and t_{ref} are the t_{cfd} of the respective pulses.

To transform τ to time-of-flight T and account for factors that may have affected timing such as light transport within the scintillator and cable length, a time calibration was performed using the gamma rays that were produced in the target at the same time as the neutrons. Gamma rays travel at the speed of light c and therefore present as a separate distribution of events to the neutron events. The value of τ corresponding to the gamma ray peak τ_γ was determined through the fitting of a Gaussian distribution to the peak. Using the known distance between the detector and the source l:

$$T = T_\gamma + \tau_\gamma - \tau \qquad\qquad T_\gamma = \frac{l}{c} \tag{4.9}$$

where T_γ is the ToF of the gamma rays. The energy of the neutron events were then calculated according to Eq. 3.6 in Section 3.3.

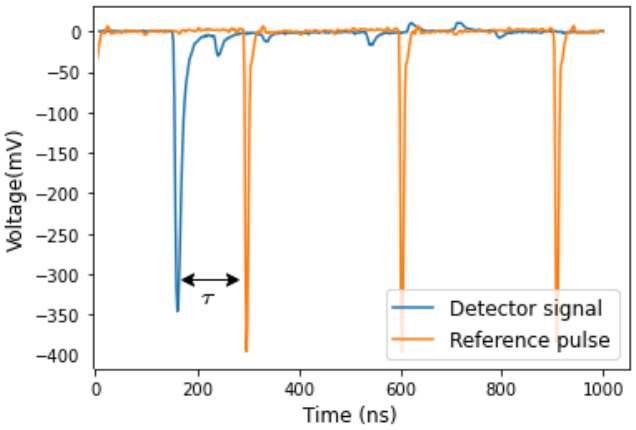

Figure 4.19: The signals from the BC-501A detector at iThemba LABS and reference pulses associated with the pulsed proton beam incident on the Li target. The parameter τ which defines the time between the reference pulse and the detector pulse is indicated.

4.4.2 Unfolding

As discussed in Section 3.4, unfolding is the de-convolution of the measured light output spectrum to determine the energy spectrum of the incident radiation and requires both a matrix of response functions and a default energy spectrum in addition to the measured light output spectrum. In the work presented, the UMG-3.3 [191] package was used to unfold the measured light output spectra, specifically the two unfolding algorithms, GRAVEL and MAXED.

GRAVEL, which is a slight modification to the SAND-II algorithm [192], is an iterative algorithm. The default spectrum supplied is iteratively modified until it converges on a solution spectrum $S(E)$ [193]. The algorithm will stop when the χ^2/dof of the measured light output spectrum and the calculated light output spectrum from $S(E)$ reaches a desired value or the number of iterations exceeds the limit set by the user. The desired χ^2/dof is typically set to one, however in some cases this value is too low and can result in over convergence.

MAXED is an unfolding algorithm which uses the maximum entropy principle [194]. Since the solution for $S(E)$ is not unique, MAXED uses *a priori* information to help the algorithm produce a final best estimate which is close to the true spectrum. The algorithm relies heavily on the *a priori* information and therefore the default energy spectrum that is supplied must be close to the true spectrum. The method with which $S(E)$ is calculated allows for the uncertainties of the solution to be calculated through Type A evaluation which is provided by the ICQU code included in the UMG-3.3 package.

For both GRAVEL and MAXED unfolding detector specific response functions are essential. For neutrons with energies below 20 MeV they can be determined through simulation, however above 20 MeV the neutron data libraries are not sufficiently accurate and the

response functions must be measured. In the work presented, response functions for the compact detector are produced through measurements of neutrons with energies between 11 MeV and 62 MeV.

Instead of performing many measurements of monoenergetic neutrons at small increments of energy, a measurement of a broad spectrum neutron field was made. Through time-of-flight (ToF) the energy of the neutron associated with each event was determined. By selecting the events of neutrons with energies within a certain range, the light output response of the detector to monoenergetic neutrons can be mimicked [36]. The "monoenergetic neutrons" will have the average energy of the energy range used when selecting the events.

For both the GRAVEL and MAXED algorithms, the energy resolution of the response functions determined by the width of the energy range used to select the events for the response function limits the minimum energy resolution of the unfolded energy spectrum. The width of the energy range used to select the events also affects the edge resolution of the response function which impacts the energy resolution from unfolding.

Chapter 5

Results and Discussion

The measurements of the neutron fields performed with the EJ-276 compact detector, detailed in Section 4.2, are analysed and discussed in this chapter. The analysis of the measurements performed with the BC-501A and EJ-301 reference detectors are presented for comparison.

5.1 Light Output Calibration

As discussed in Section 4.3.1, the calibration of the light output parameter requires determining the linear relationship between the long integral parameter Q_L and the light output parameter L, where L is equivalent to energy for gamma ray events. The Q_L value of the Compton edge of the gamma ray spectrum is determined through the fitting of a half Gaussian distribution and the energy of the Compton edge can be calculated using Eq. 3.5. The Compton edge energies for the gamma rays used in this work are shown in Table 4.4. The method used for determining the calibration scaling factor between Q_L and L depends on the number of data points available for calibration. In cases when there were three or more data points a weighted linear fit was performed, else a weighted average of the ratio between Q_L and energy of the Compton edge was used.

A measurement of the gamma ray emission by an AmBe source was performed at all three of the facilities. Figure 5.1 shows a comparison of the gamma ray light output spectra after calibration measured with the reference (a) and compact (b) detectors. The spectra measured with the compact spectrometer in Figure 5.1 (b) have a complete lack events at higher L, as a result the Compton edge expected at 4.2 MeV_{ee} is not visible. The origin of this behaviour is not known at this stage and requires further investigation. It is possible that it is associated with poor light collection due to the length of the scintillator. This behaviour was not observed for lower energy gamma rays and thus may only become relevant for gamma rays at higher energies. Additionally, the spectrum measured at the n-lab with the compact detector has a distinctly different shape to those measured at

AMANDE and iThemba LABS, lacking the increase in events around 1 MeV$_{ee}$ and having events up to higher L. This could be a result of the longer t_L used on the digitised pulses of this data set, and the difference in overall quality (Figure 4.18 (b)).

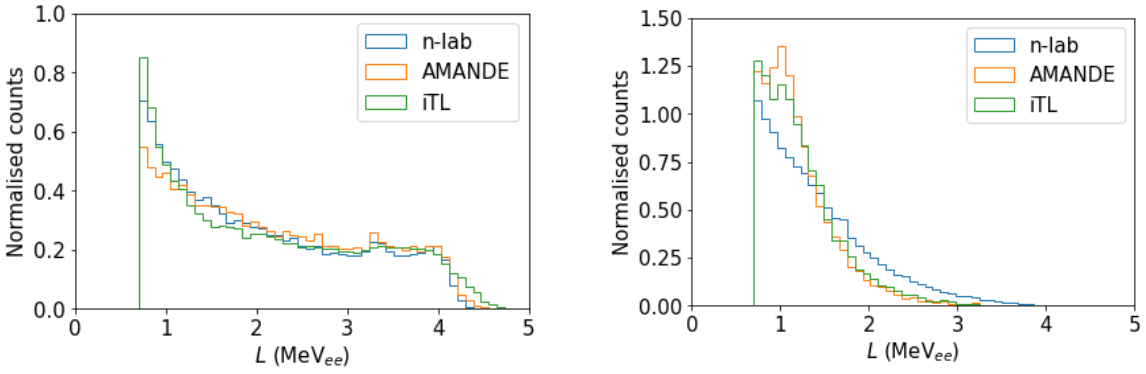

(a) (b)

Figure 5.1: The AmBe gamma ray L spectra measured with the (a) reference and (b) compact detectors at the n-lab, AMANDE and iThemba LABS (iTL) facilities.

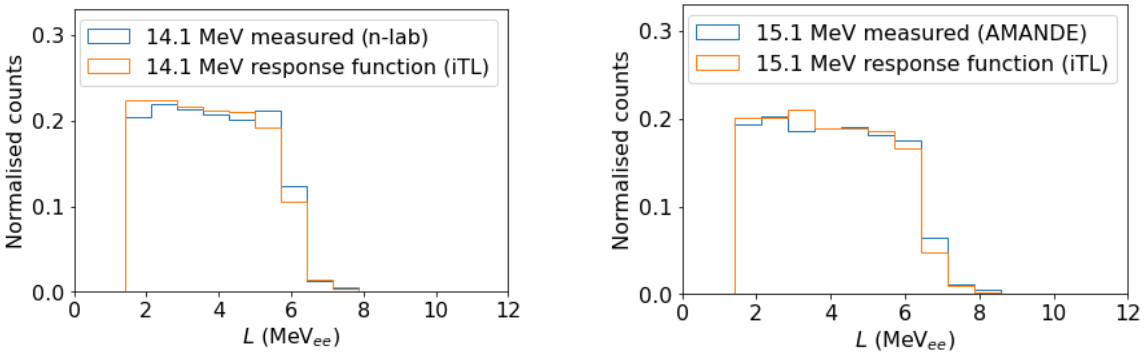

(a) (b)

Figure 5.2: The calibrated neutron light output spectra measured for (a) 14.1 MeV neutrons at n-lab and (b) 15.100 MeV neutrons at AMANDE and matched to the light output spectrum constructed for the same energy from the iThemba LABS (iTL) measurements for 66.0 MeV proton incident on a Li target.

For the n-lab and AMANDE data sets measured with the compact detector, lower energy gamma rays were available for the calibration process, however a measurement of an AmBe source was the only calibration measurement made with the compact spectrometer during the iThemba LABS campaign. Due to the absence of a Compton edge in the AmBe gamma ray light output spectrum, the light output was calibrated by comparing monoenergetic neutron light output spectra, as determined from time-of-flight analyses, to those measured for monoenergetic neutron sources at the n-lab and AMANDE with energies of 14.1 MeV and 15.100 MeV respectively, as shown in Figure 5.2. A scaling factor was applied to Q_L

measured at iThemba LABS with the compact detector such that the Compton edge matched with the equivalent light output spectrum measured at the n-lab and AMANDE. Since there were only two neutron spectra for the calibration a weighted average of the calibration factors was used.

5.2 Time-of-Flight

Time-of-flight measurements were made for the neutron fields produced by 1.84 MeV deuterons on a 793 μg cm^{-2} thick D target at AMANDE and 66.0 MeV protons on an 8.0 mm thick ^{nat}Li target at iThemba LABS. As described in Section 3.3 the time between the measured and the reference pulse from the accelerator is calculated to obtain the time-of-flight. The flight path, l, was defined as the distance between the target and detector, where the detector position is set to be at one third of the scintillator length, relative to the incident radiation direction.

Figures 5.3 and 5.4 show the distribution of events as a function of L and T for the measurements the radiation fields produced by 1.84 MeV deuterons on a D target and 66.0 MeV protons on a Li target. There is a significant difference in light output of the events indicating that the compact and reference detectors have a significantly different relationship between L and energy.

In Figures 5.3 (a) and 5.3 (b) the distributions at $T = 6.9$ ns and 7.4 ns respectively are associated with the gamma rays produced at the deuterium target and the distributions at $T = 66.5$ ns and 70.9 ns respectively are associated with the 5.000 MeV monoenergetic neutrons. The distribution at -53.4 ns is also associated with gamma rays, however these gamma rays are produced by the deuteron beam colliding with a material estimated to be 16.0 m before the target.

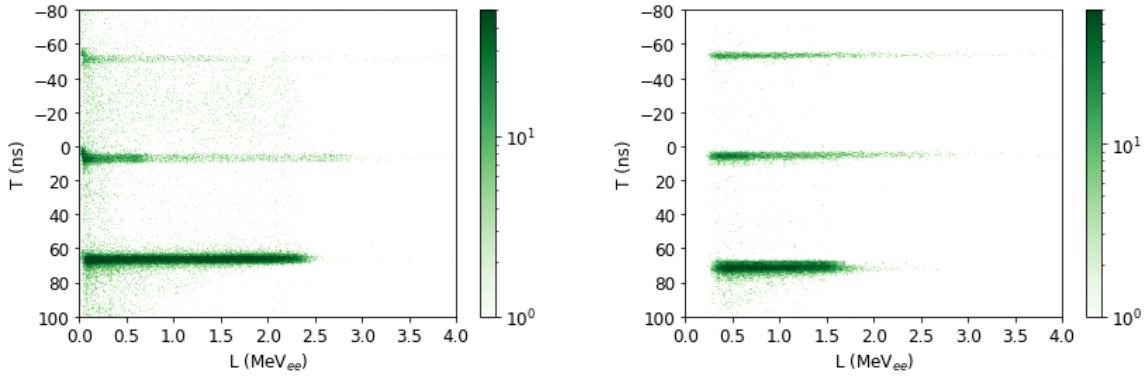

(a) BC-501A (b) EJ-276

Figure 5.3: Counts as a function of L and time-of-flight parameter T for the (a) BC-501A reference and (b) EJ-276 compact detectors from measurements of the radiation field produced by 1.84 MeV deuterons on a deuterium target at distances of 2.058 m and 2.168 m respectively.

In Figures 5.4 (a) and 5.4 (b) the distributions at $T = 27.1$ and 26.8 ns respectively are associated with the gamma rays produced at the Li target and the distribution of events at $T > 75$ ns are associated with the neutrons produced at the Li target. The measurements in Figures 5.4 (a) and (b) have a wide distribution of neutron events in T, in comparison to the localised distributions in 5.3 because the neutron field at iThemba LABS comprised of a broad range of energies while the neutron beam at AMANDE is monoenergetic.

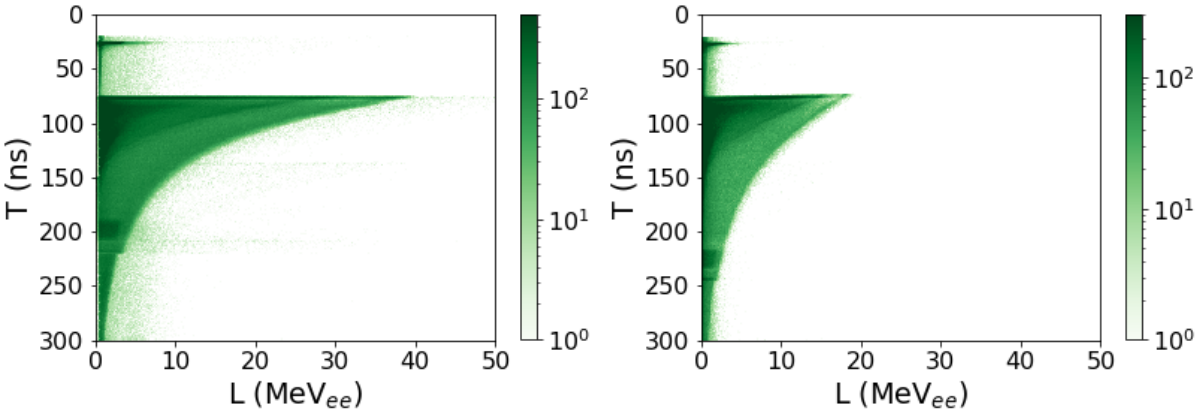

(a) BC-501A

(b) EJ-276

Figure 5.4: Counts as a function of L and time-of-flight parameter T for the (a) BC-501A reference and (b) EJ-276 compact detectors from measurements made using a 66.0 MeV proton beam irradiating an 8.0 mm Li target, at distances of 8.13 m and 8.04 m respectively.

5.3 Pulse Shape Discrimination

Pulse shape discrimination was implemented to separate the neutron events from the gamma ray events using the charge comparison method detailed in Section 4.3.2. The event density plots of the pulse shape parameter S as a function of L are shown in Figures 5.5, 5.6, 5.7 and 5.8. The green dashed lines, which were chosen by eye, were used to separate the majority of the events associated with recoil electrons (e) induced by gamma rays and the events associated with recoil heavy charged particles such as protons (p), deuterons (d), tritons (t) and alpha particles (α) from the neutron interactions in the scintillator.

In measurements of the 5.000 MeV neutron field produced 1.84 MeV deuterons on a deuterium target (Figures 5.5 (a) and (b)), the neutron energy is not high enough for the threshold reactions which produce heavier charged particles such as deuterons, tritons and alpha particles. Figure 5.5 (a) does however, have a bump in the proton recoil locus between 1 MeV$_{ee}$ and 2 MeV$_{ee}$ which is associated with multiple scatters in the detector. This is not seen in Figure 5.5 (b) due to its comparatively small volume. As discussed in Chapter 3, at energies above 6.5 MeV these inelastic reactions become possible and in

the measurements of the 14.1 MeV and 15.100 MeV neutron beams (Figure 5.6 (a,b) and Figure 5.7 (a,b) respectively) features associated with deuterons (d) and alpha particles (α) can be seen as indicated. The features associated with the deuterons can only be seen in the measurements taken with the reference detectors due to the comparatively poorer quality of PSD of the compact detector primarily associated with poorer light collection. The events that occur between the recoil electron and proton loci seen in Figures 5.6, 5.7 and 5.8 are associated with recoil protons which escape before depositing their full energy. Since the range of the protons increases with energy so does the number of escaping recoil protons. The bending at the high L region of the recoil proton locus in Figures 5.8 (a,b) is a result of pulse saturation, where the pulse height exceeds the voltage range of the digitiser, and the spread of single events around the outside of the high density region are due to event pile up [30].

The figure of merit was calculated for the measurements of the radiation field produced by the STNG at the n-lab performed with the EJ-301 reference and EJ-276 compact detectors shown in Figure 5.6. Since the two detectors have different L scales the events for the FoM calculation were selected such that they fell between 0.29 and 0.33 of the recoil proton edge. The reference detector and compact detector exhibited FoMs of 2.52 $\pm$ 0.03 and 1.43 $\pm$ 0.04 respectively. The compact detector displays inferior PSD quality in comparison to the reference detector systems in all of the measurements presented. This is attributed predominantly to the characteristics of the scintillators [157, 195] and light collection geometry. However, the compact detector still displays PSD that is sufficient for n-γ separation.

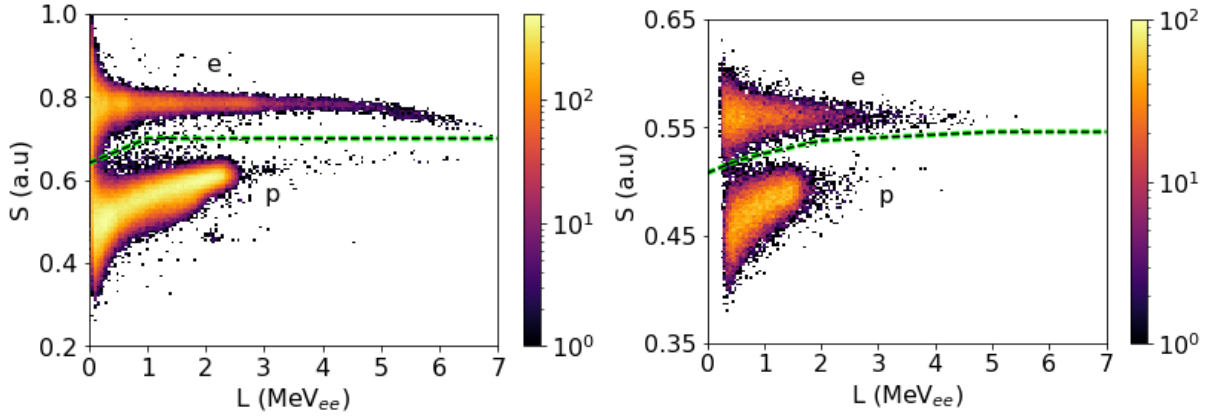

(a) (b)

Figure 5.5: Counts as a function of light output parameter L and pulse shape parameter S for events in the (a) reference detector and (b) compact detector when irradiated by the neutrons and gamma rays produced by 1.84 MeV deuterons irradiating a deuterium target. Loci associated with recoiling electrons (e) and protons (p) are indicated. The green dashed line indicates the cut used to separate neutron and gamma ray events.

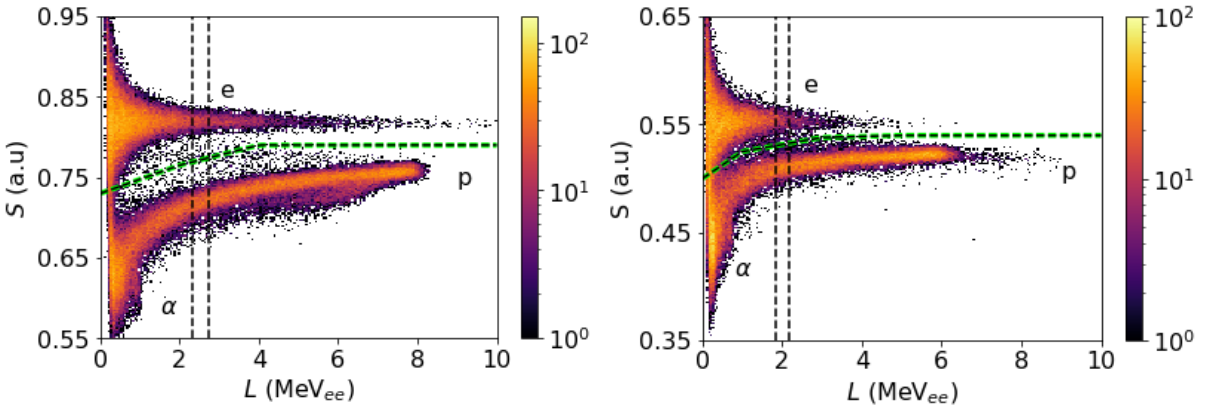

(a) (b)

Figure 5.6: Counts as a function of light output parameter L and pulse shape parameter S for events in the (a) reference detector and (b) compact detector when irradiated by the neutrons and gamma rays produced by the STNG embedded in a HDPE cave. Loci associated with recoiling electrons (e), protons (p), deuterons (d) and alpha particles (α) are indicated. The green dashed line indicates the cut used to separate neutron and gamma ray events. The figure of merit was calculated for the region indicated with the black dashed lines.

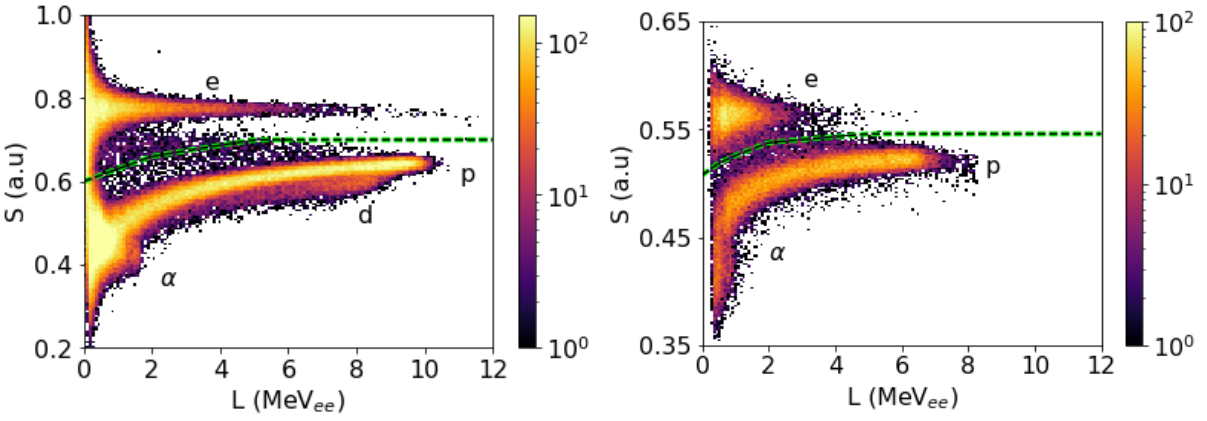

(a) (b)

Figure 5.7: Counts as a function of light output parameter L and pulse shape parameter S for events in the (a) reference detector and (b) compact detector when irradiated by the neutrons and gamma rays produced by 0.43 MeV deuterons irradiating a tritium target. Loci associated with recoiling electrons (e), protons (p), deuterons (d) and alpha particles (α) are indicated. The green dashed line indicates the cut used to separate neutron and gamma ray events.

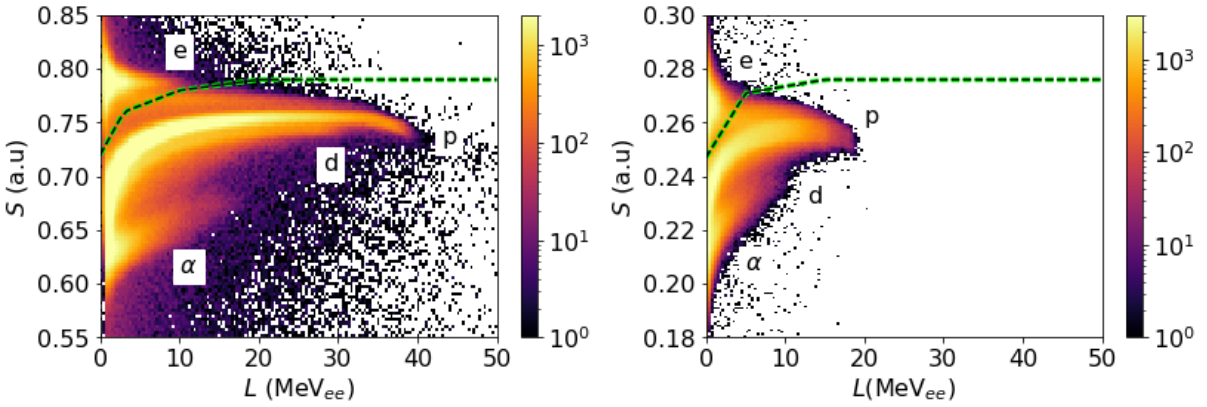

(a) (b)

Figure 5.8: Counts as a function of light output parameter L and pulse shape parameter S for events in the (a) reference detector and (b) compact detector when irradiated by the neutrons and gamma rays produced by 66.0 MeV protons irradiating a 8.0 mm Li target. Loci associated with recoiling electrons (e), protons (p), deuterons (d) and alpha particles (α) are indicated. The green dashed line indicates the cut used to separate neutron and gamma ray events.

5.4 Neutron Light Output Spectra

Figure 5.9 shows the neutron light output spectra obtained after excluding the gamma ray events through the cuts shown in Figures 5.5 to 5.8. As seen in the previous sections, the two detectors exhibit very different light output responses indicating a significant difference in the relationship between L and the neutron energy. Additionally the shapes of the spectra are distinctly different. The edges of the spectra measured with the compact detector are very sharp, however the lower portion of the edge is drawn out. In Figure 5.9 (a) for 5.000 MeV neutrons the spectrum also lacks the characteristic proton recoil continuum. The spectra measured with the reference detectors have rounded but well defined edges, with the spectra measured by the reference detector at AMANDE, shown in 5.9 (a) and (c), exhibiting a slightly rounder shaped edge. In the light output spectrum from the 5.000 MeV neutrons (Figure 5.9 (a)) the small increase at approximately 1.8 MeV_{ee} associated with multiple scatters is visible. In Figure 5.9 (d) the light output spectrum from the compact detector is significantly different in shape to that of the reference detector. Considering the edge positions of the light output spectra in Figures 5.9 (a), (b) and (c) in comparison to the end of the events in (d), the light output response of the compact detector is clearly not linear as expected. This, and the different relationship between the gamma ray and neutron light output in comparison to the reference detector, requires further investigation to understand the origin. From a neutron spectroscopy standpoint these unexpected behaviours did not prevent unfolding analyses since they were incorporated in the detector response functions.

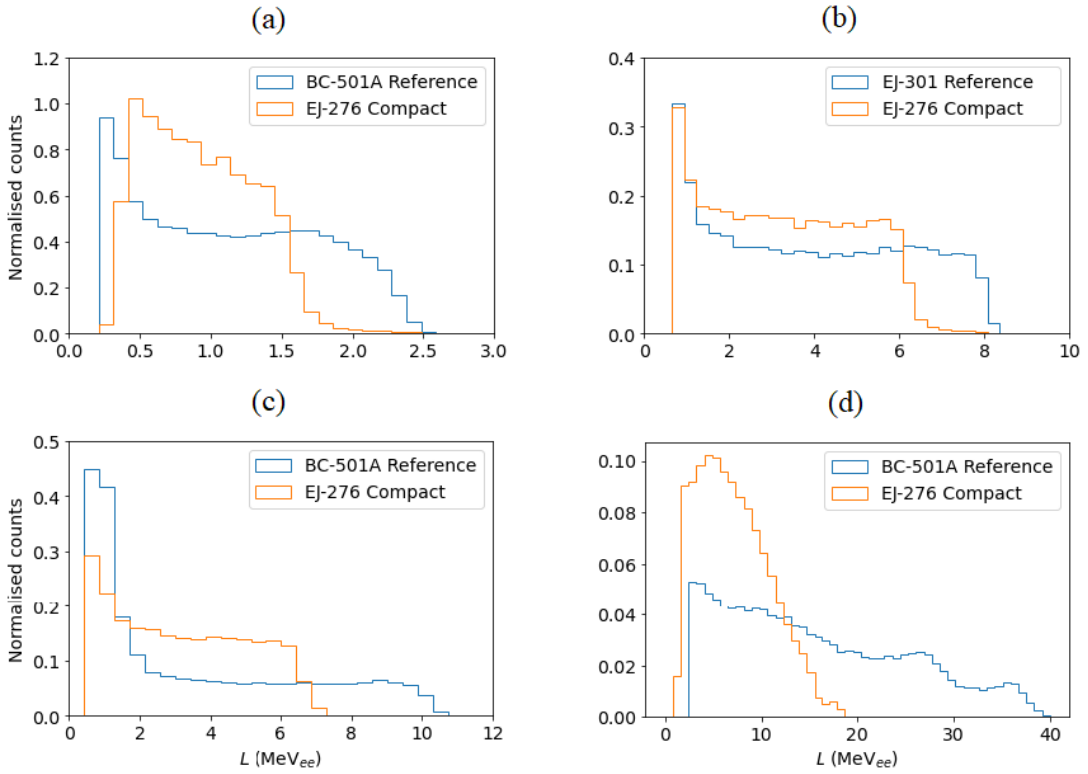

Figure 5.9: The neutron light output spectra of the measurements taken with the compact spectrometer (orange) and the reference detectors (blue) of (a) 5.000 MeV, (b) 14.1 MeV and (c) 15.100 MeV monoenergetic neutron fields and (d) the neutrons within the peak centered at 62.5 MeV (selected via ToF) from neutron field produced by 66.0 MeV protons on a 8.0 mm Li target.

The edge resolution of the monoenergetic light output spectra in Figures 5.9 were calculated using:

$$R_L = \frac{\Delta L}{L_e} \cdot 100\% \tag{5.1}$$

where ΔL is the FWHM of the half Gaussian distribution fitted to the edge of the spectrum and L_e is the L value of the Compton edge. The calculated edge resolution of the spectra are shown in Table 5.1. The degradation of edge resolution in the compact detector system relative to the reference detector systems could be attributed to poorer light collection characteristics.

Table 5.1: Edge resolution of the neutron light output spectra of monoenergetic neutron fields measured with the reference detector and the liquid scintillator compact detector.

Neutron energy (MeV)	**Reference detector** (%)	**Compact detector** (%)
5.000	22.2 ± 1.5	33.0 ± 1.6
14.1	10.3 ± 0.9	16.0 ± 0.8
15.100	15.2 ± 1.7	23.9 ± 1.9

5.5 Neutron Energy Spectra from Time-of-Flight

Figure 5.10 shows the neutron energy spectra that were calculated from time-of-flight at AMANDE and iThemba LABS for events with $L > 2.5$ MeV$_{ee}$ for the reference detectors and $L > 1.0$ MeV$_{ee}$ for the compact detector after the exclusion of the gamma ray events. Due to the reference and compact detectors having L scales that are not equivalent, the lower L threshold used for the compact detector was lowered until the shape of the continuum region in the neutron energy spectrum was in good agreement with the spectrum measured with the reference detector as shown in Figure 5.10 (b).

A Gaussian distribution was fitted to each peak in the energy spectra to determine the average energy and the energy resolution. The energy resolution R_E was calculated using

$$R_E = \frac{\Delta E}{E_{av}} \cdot 100\%, \tag{5.2}$$

where ΔE is the FWHM and E_{av} is the centroid associated with the fitted Gaussian distribution. The uncertainties for the average energy of the peak were calculated using a combination of the uncertainty of the fit and the uncertainty associated with the distance between the detector and the source which was propagated through the kinetic energy calculation using Eq. 3.6. Similarly, the uncertainty of energy resolution was calculated by taking a combination of uncertainty on the average energy and the FWHM of the fit.

The energy spectra of the 5.000 MeV neutron field measured at AMANDE are shown in Figure 5.10 (a). The energy spectra measured with the two detectors demonstrate good agreement with each other and the expected energy. The peak in the energy spectrum measured by the BC-501A reference detector is centered at 5.09 ± 0.05 MeV and at 5.11 ± 0.09 MeV in the spectrum from the EJ-276 compact spectrometer. The detectors display comparable energy resolutions at 5.000 MeV of 12.81 ± 0.29% (BC-501A) and 13.11 ± 0.38% (EJ-276). The timing resolution of the detector system plays the largest role in determining the energy resolution when using ToF. Since both detector systems use the same data acquisition system which has a set sampling rate, the timing resolution of the systems are likely to be similar. The asymmetry in the energy spectra is attributed to energy loss of the deuteron in the target.

The 66.0 MeV protons irradiating an 8.0 mm Li target produce a broad neutron field with a calculated primary peak energy of 62.5 MeV. The energy spectra measured with the BC-501A reference and EJ-276 compact detectors shown in Figure 5.10 (b) have peaks centered at 62.49 ± 0.24 MeV and 62.59 ± 0.31 MeV respectively, which are in agreement with each other and the predicted value. The variation in spectrum shape at lower energy is likely due to the lower L thresholds applied to the data sets not being equivalent. Additionally, the measurements were made in parasitic mode during a beam conditioning campaign at the fast neutron facility at iThemba LABS which could have attributed to some of the differences at low energies. With an energy resolution of 7.25 ± 0.26 % at 62.5 MeV the BC-501A reference detector performs marginally better than the EJ-276 compact detector which has an energy resolution of 8.21 ± 0.29 %. The

decreased energy resolution of the compact detector is likely due to a combination of lower statistics and the poor pulse quality affecting the consistency of the CFD timing.

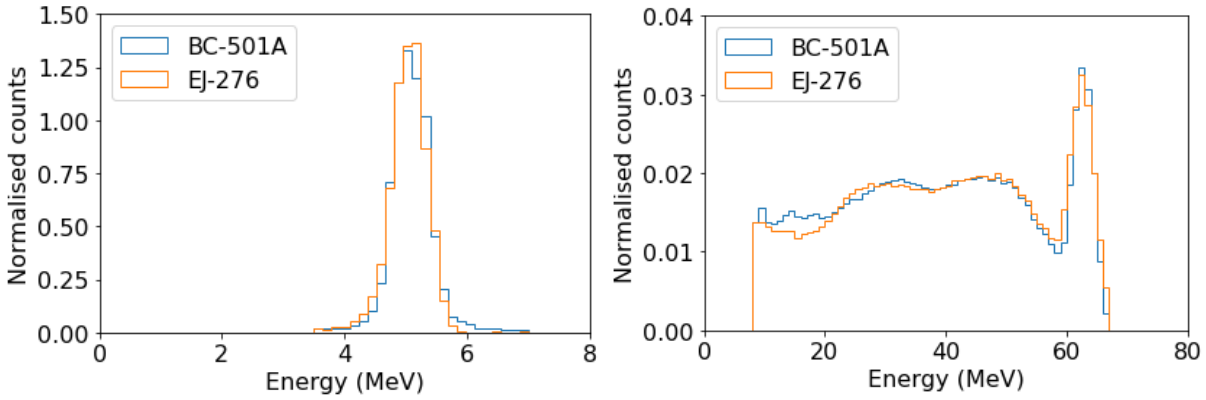

(a) (b)

Figure 5.10: Neutron energy spectra determined via time-of-flight measurements of the (a) 5.000 MeV neutron field at AMANDE produced by irradiating a deuterium target with 1.84 MeV deuteron at 0° relative the beam line and the (b) neutron field produced at iThemba LABS by a 66.0 MeV proton beam irradiating an 8.0 mm Li target measured at 16° from the beam line, using a BC-501A reference detector and EJ-276 compact detector. The spectra have been normalised to have the same total number of counts.

5.6 Neutron Response Functions

Response functions for both the iThemba LABS BC-501A reference detector and the compact detector were constructed for neutrons with energies between 11 MeV and 62 MeV using the measurements of the field produced by 66.0 MeV protons on an 8.0 mm Li target at iThemba LABS. Figure 5.11 shows a subset of the response functions constructed for both detectors which have been normalised to have equivalent areas. The response matrices were constructed using the light output spectra produced by neutron events within consecutive 3 MeV wide energy ranges as determined by ToF centered at energies between 11 MeV and 62 MeV. A 3 MeV wide energy range was used such that the response functions were sufficiently populated with events at all energies for unfolding.

By only selecting events within a small energy range the response function produced is considered a good approximation of a monoenergetic neutron with the energy of the center of the bin, as illustrated in Figure 5.12 which shows the comparison of the 14 MeV response function and the measured 14.1 MeV monoenergetic neutron light output spectrum for the compact spectrometer. The measured spectrum has far superior edge resolution than the response function, however the edge position (at half height) are in good agreement. The nearly monoenergetic response functions were used to construct a response matrix for each detector in the format required for the GRAVEL and MAXED unfolding packages.

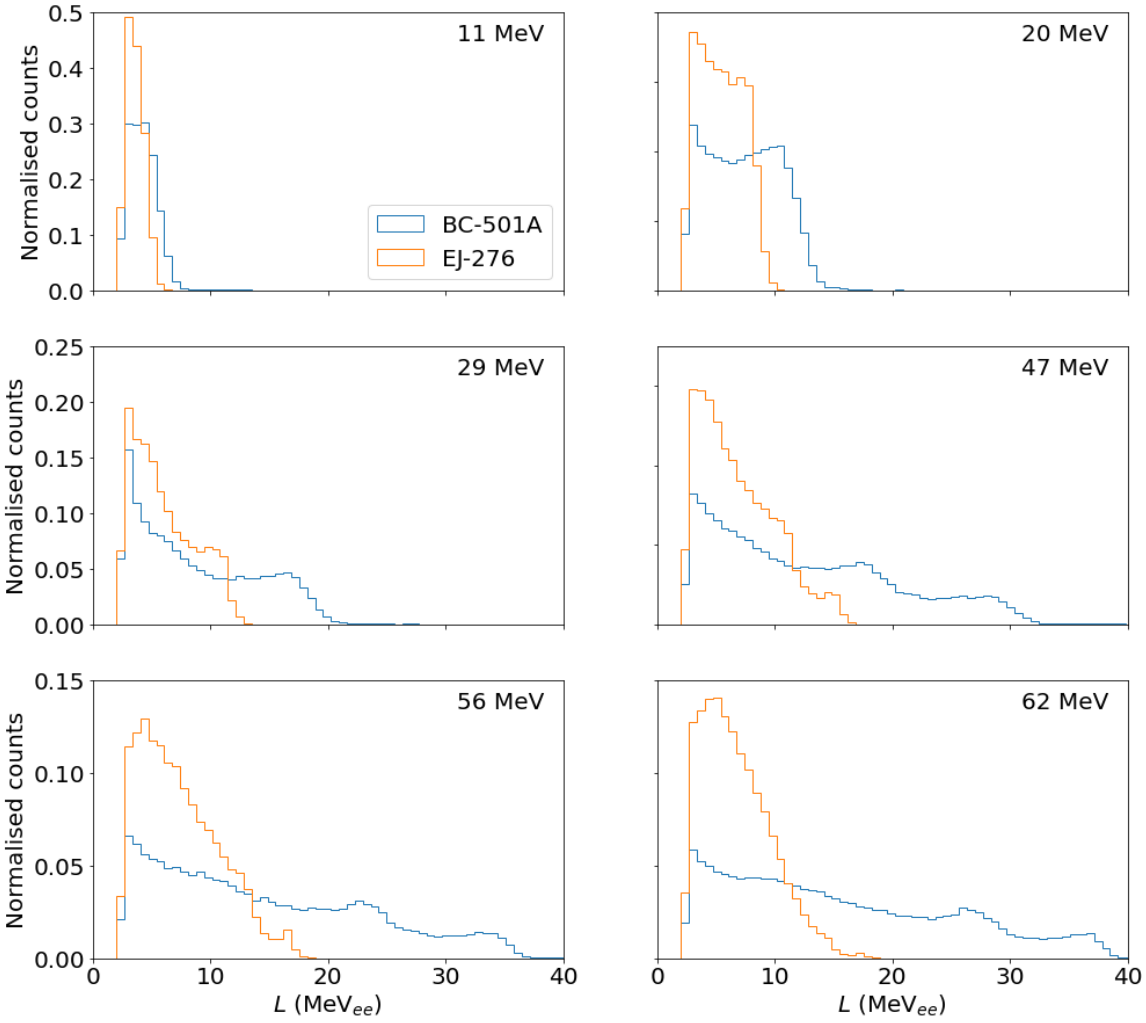

Figure 5.11: Comparison of the response functions for the EJ-276 compact spectrometer and BC-501A reference detector produced from 3 MeV wide energy cuts in the energy spectrum defined from time-of-flight analyses. The response functions shown are centered at 11 MeV, 20 MeV, 29 MeV, 47 MeV, 56 MeV and 62 MeV.

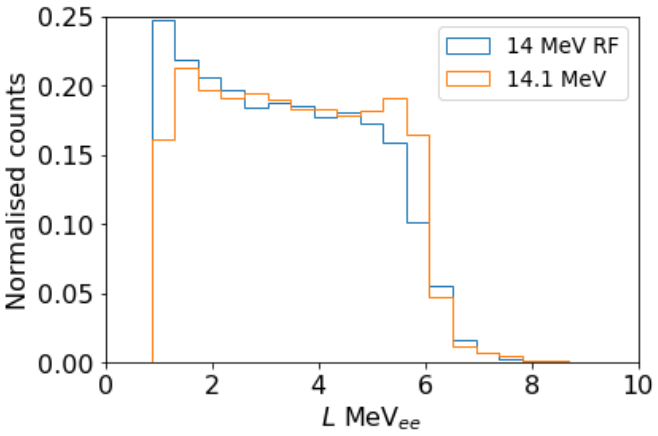

Figure 5.12: Comparison between the 14 MeV response function (RF) and the 14.1 MeV neutron light output spectrum measured with the compact spectrometer.

5.7 Spectrum Unfolding

The response functions presented in the previous section will ultimately be used to unfold the energy spectra from neutron light output spectra measured outside of the laboratory. However, the response functions first need to be validated by unfolding known energy spectra.

A light output spectrum using equal ratios of the 11, 29, 44 and 62 MeV response functions was constructed and unfolded. Figures 5.13 (a) and (b) show the light output spectra constructed from the response functions of the reference and compact detectors respectively. Unless otherwise specified, the unfolding presented in this section the light output spectra were initially unfolded using GRAVEL with a uniformly flat default spectrum. The unfolding with GRAVEL is discussed in greater detail in Appendix B. Since MAXED unfolding is highly sensitive to both the default spectrum and the χ^2_{dof} supplied, the energy spectrum from the GRAVEL unfolding was used as the default spectrum and to indicate a realistic χ^2_{dof} value. The constructed light output spectra were compared with the re-folded light output spectra and in both Figure 5.13 (a) and (b) the algorithm converged on these solutions with a χ^2_{dof} of 0.1. Considering the light output spectrum was constructed from the response functions a χ^2_{dof} value close to zero (which implies perfect agreement) is expected. Figure 5.13 (c) shows the unfolded energy spectra. For both the reference and compact detectors the unfolding procedure produced an energy spectrum with peaks at the expected energies, however at higher energies the peaks become less defined. Figure 5.14 shows the response functions of both detectors for energies above 40 MeV and, particularly in the response functions of the compact detector, there is only a small difference between consecutive response functions. This makes it difficult for the algorithm to differentiate between the response functions resulting in the lowered accuracy as the energy increases seen in Figure 5.13 (c).

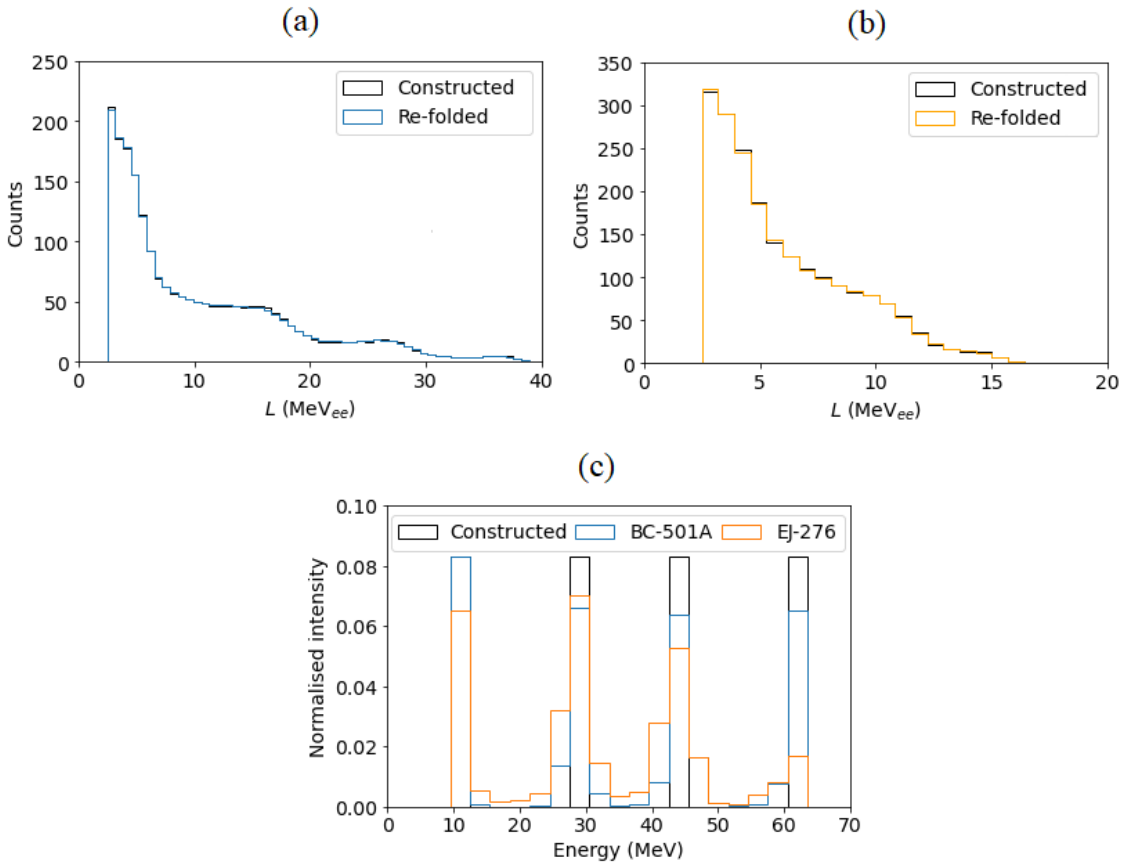

Figure 5.13: The light output spectra constructed using equal ratios of the 11 MeV, 29 MeV, 44 MeV and 62 MeV response functions for the (a) BC-501A reference detector and (b) EJ-276 compact detector and the respective re-folded light output spectra. In both cases the constructed and re-folded light output spectra have a χ^2_{dof} of 0.1. (c) The energy spectra unfolded with MAXED for the reference and compact detectors in comparison to the constructed energy spectrum.

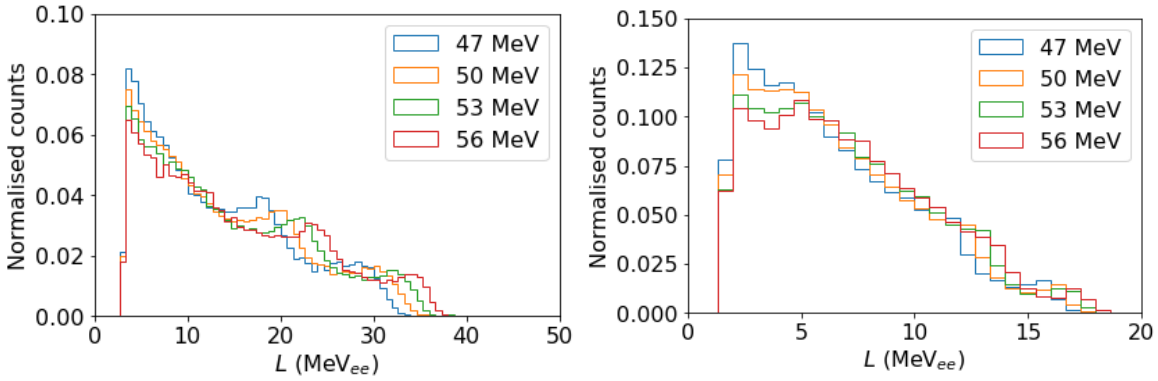

(a) (b)

Figure 5.14: The response functions from 47 MeV up to 56 MeV for the (a) BC-501A reference detector and (b) the EJ-276 compact detector.

The response functions were then used to unfold the measurements of 14.1 MeV and 15.100 MeV monoenergetic neutrons that were measured at the n-lab and AMANDE facilities. The unfolding of the 14.1 MeV neutron spectra are discussed in Appendix B. The light output spectrum of the 15.100 MeV neutron field measured with the compact detector at AMANDE (Figure 5.15 (a)) was unfolded to produce the energy spectrum in Figure 5.15 (b). The unfolded spectrum is in good agreement with the expected energy spectrum, having its most significant contribution in the bin centered at 14 MeV which covers the range of 12.5 MeV to 15.5 MeV. The expected energy spectrum is based on the assumption that the detector has as similar energy resolution at 15.100 MeV as it did at 5.000 MeV. The energy spectrum was modelled as a Gaussian distribution with $\mu = 15.100$ MeV and a FWHM of 2.0 MeV. The measured energy spectrum is presented as the Gaussian estimate binned using the same binning structure as the unfolded energy spectrum. The re-folded light output spectrum and measured input spectrum shown in Figure 5.15 (a) have a χ^2_{dof} agreement of 1300, which is very high. The large difference in the edge resolution of the light output measured for a 15.100 MeV monoenergetic source light output spectrum and the response functions with a bin width of 3 MeV means the lower resolution re-folded spectrum and high χ^2_{dof} value are not unreasonable in this context.

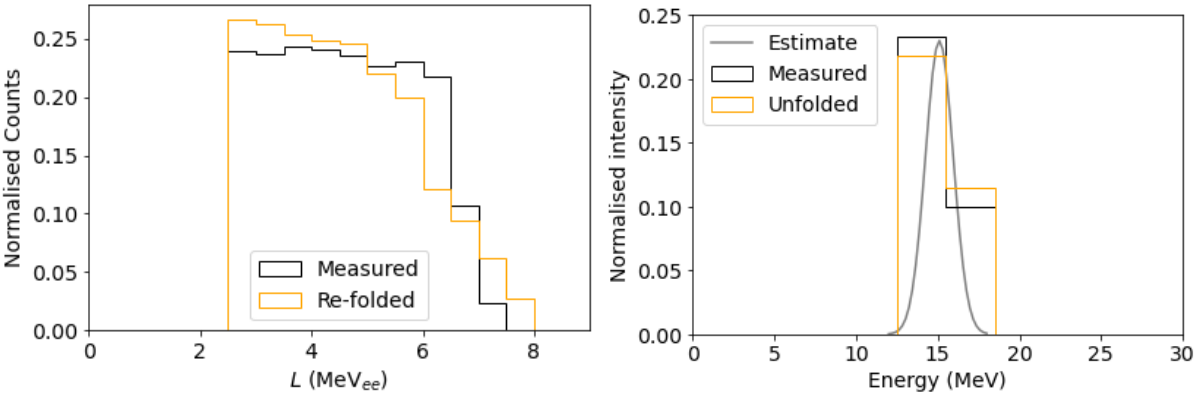

(a) (b)

Figure 5.15: (a) The light output spectrum of 15.100 MeV neutrons measured with the compact detector in comparison to the re-folded light output spectrum. The spectra agree with a χ^2_{dof} of 1300. (b) The energy spectrum unfolded with MAXED for the 15.100 MeV neutrons and the measured energy spectrum which is estimated to be a Gaussian distribution centered at 15.100 MeV with a FWHM of 2.0 MeV.

At this point it is worth noting that MAXED is highly sensitive to the default spectrum it is supplied, particularly for complex fields such as the neutron field measured at iThemba LABS. The unfolding of the light output spectra of the neutron field produced by 66.0 MeV protons on an 8.0 mm Li target measured at iThemba LABS yielded the best results (Figure 5.16) when using an energy spectrum calculated from ToF as the default spectrum. The effect that the choice of default spectrum and χ^2_{dof} value have on the unfolded solution are discussed in greater detail in Appendix B.

Figure 5.16 shows the unfolded energy spectra compared to the energy spectrum determined by ToF. The energy spectrum calculated by ToF with a L threshold of 1 MeV$_{ee}$ was used as the default spectrum (Figure 5.10 (b)). The measured and re-folded light output spectra in Figure 5.16 (a) have a χ^2_{dof} of 58. The high χ^2_{dof} value is likely due to a combination of the differences in the measured and re-folded spectra in the low and high L regions and an underestimate of the uncertainty. The unfolded energy spectrum in Figure 5.16 (b) is in good agreement with the expected energy spectrum with the most significant differences occurring below 20 MeV and above 50 MeV. The differences in the energy spectrum above 50 MeV are attributed to the similarity in the response functions at those energies (Figure 5.14. Since the L spectra of the low energy neutrons overlap with those of the higher energy neutrons the lack of definition between the high energy response functions can also affect the quality of the unfolding at lower energies.

In scenarios where measurements of a neutron field outside of a laboratory environment are taken, the neutron field is very rarely completely unknown, as measurements of similar neutron fields or computational simulations of the field will often be available. A default spectrum with a slightly different shape to the input spectrum (achieved through the use of a different lower L threshold) was therefore chosen to highlight that with a default spectrum that is similar but not identical to the input spectrum, as could be expected in out-of-lab measurements, the algorithm is capable of finding an acceptable solution.

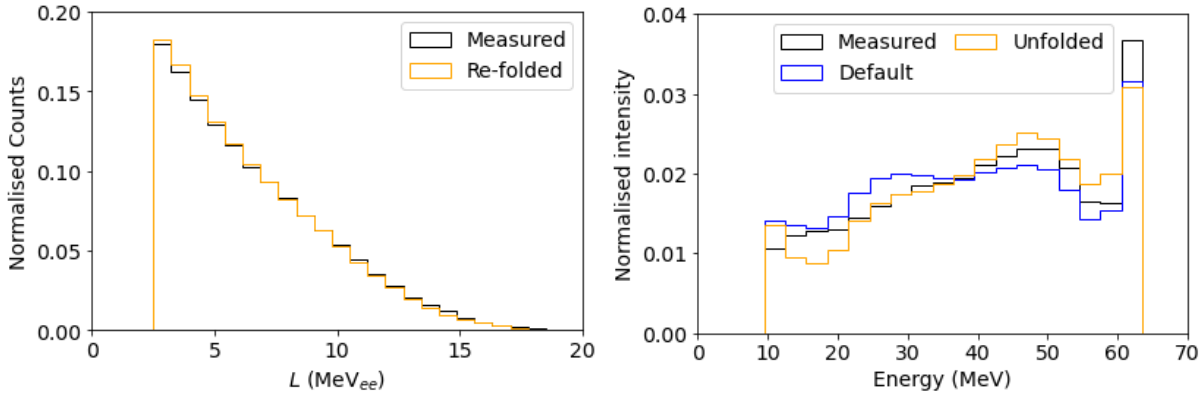

(a) (b)

Figure 5.16: (a) The light output spectrum measured with the EJ-276 compact detector of the neutron field produced by 66.0 MeV protons on an 8.0 mm Li target at 16° in comparison to the re-folded light output spectrum. The spectra agree with a χ^2_{dof} of 58. (b) The associated energy spectrum unfolded with MAXED in comparison to the expected energy spectrum determined from ToF analyses using a lower L threshold of 2.5 MeV$_{ee}$ and the default spectrum which is the energy spectrum determined from ToF analyses using a lower L threshold of 1 MeV$_{ee}$.

5.8 Further Characterisations

5.8.1 Detector efficiency

The efficiency of the BC-501A detector at iThemba LABS, shown in Figure 5.17 (a), was previously calculated for a threshold of 2.5 MeV_{ee} [196] over the full energy range using MCNPX [197] by calculating the energy deposition and light production for each charged particle event and summing all contributions associated with each incident neutron. The calculated efficiency was then re-normalised to agree with the results from the code SCINFUL [198] at 100 MeV. This efficiency calculation has been used consistently, over a wide range of measurements with this detector [199]. The neutron energy spectra in Figure 5.10 (b) do not represent the neutron fluence since they have not been corrected for the efficiency of the detectors. The known efficiency of the BC-501A reference detector shown in Figure 5.17 (a) was applied to the the uncorrected energy spectrum in Figure 5.10 (b) to produce the spectrum in Figure 5.17 (b). The efficiency corrected spectrum in Figure 5.17 (b) has been normalised to have an area of unity; however, since this spectrum has been corrected for the efficiency of the detector it is considered to be proportional to the neutron fluence.

Since the efficiency of the compact detector was unknown, an estimate was calculated by comparing the energy spectrum measured with the compact detector in Figure 5.10 (b) and the efficiency corrected spectrum in Figure 5.17 (b). The calculated efficiency is shown in Figure 5.17 (a). The enhancement in the efficiency at $\sim$ 60 MeV is due to the reduced energy resolution of the compact detector around the peak. The efficiency of the compact detector is expected to be similar to that of the BC-501A. While the BC-501A scintillator has a higher cross section for neutron interactions than EJ-276, the additional 2 cm of length in the compact detector should off set this difference resulting in a similar efficiency per cm^2.

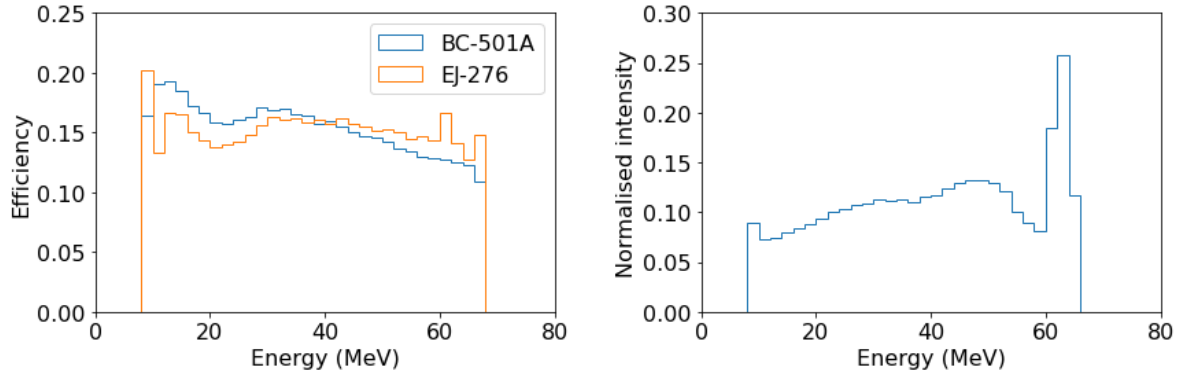

(a) (b)

Figure 5.17: (a) The efficiency as a function of energy for the BC-501A reference detector at iThemba LABS and the EJ-276 scintillator. (b) The efficiency neutron energy spectrum produced by a 66.0 MeV proton beam incident on an 8.0 mm Li target at 16° from the target measured with the BC-501A reference detector.

5.8.2 Direction sensitivity

Given that the overarching aim of this project is to create a compact spectrometer for the measurement of cosmic ray neutrons, the device may be exposed to a diffuse neutron field with neutrons entering from all directions. Due to the extreme difference in profile and length of the scintillator there is expected to be a directional sensitivity. Measurements of the 15.100 MeV neutron field at AMANDE were made with the compact spectrometer at three different angles to the beam line to investigate the directional sensitivity of the device.

The rotation of the detector relative to the beam line θ affects the effective area of the scintillator that is exposed to the radiation field from the source and the extended width x of the scintillator that the neutrons pass through, as demonstrated in Figure 5.18. Both of these factors affect the absolute efficiency of the device.

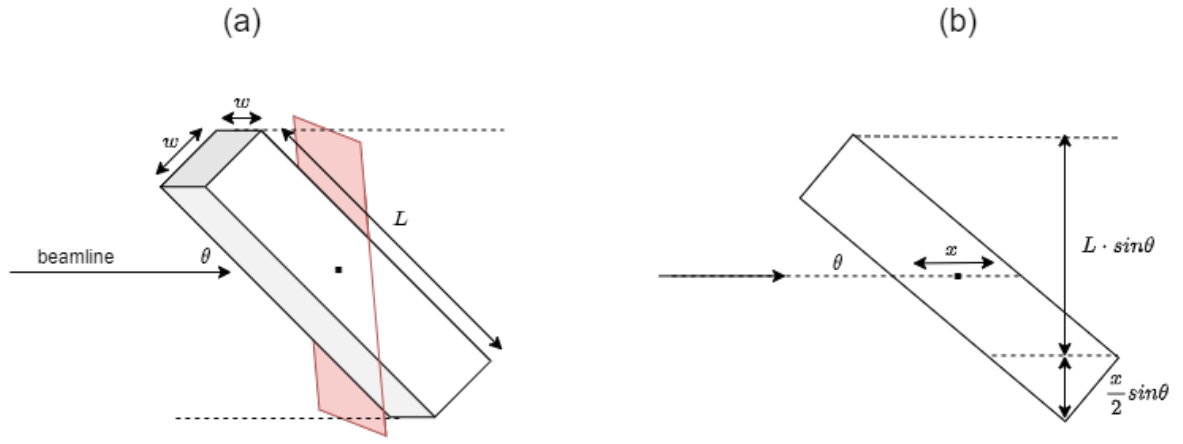

Figure 5.18: Diagrams of the scintillator illustrating (a) the physical dimensions w and L and the effective area represented by the area shaded in red and (b) the extended width x and the height of the effective area. The axis of the beam line is represented as an arrow and the angle of rotation θ is measured between the axis of the beam line and the long axis of the detector.

The detection efficiency ϵ_{det} is dependent on the probability of interaction within the scintillator. The probability distribution for interaction is given by:

$$\epsilon_{det}(x) = 1 - e^{-\frac{1}{\lambda}x}, \qquad \lambda = \frac{1}{\Sigma_{tot}}, \qquad \Sigma_{tot} = \frac{\rho N_A \sigma_{tot}}{M}, \tag{5.3}$$

where x is the extended width of the scintillator, λ is the mean free path of the neutron, Σ_{tot} is the total macroscopic cross section, ρ is the density of the scintillator, N_A is Avagadro's constant, and M is the molar mass of the scintillator. The mean free path for a 15 MeV neutron in EJ-276 was calculated to be $\sim$ 12.7 cm using the nuclear data libraries and material properties of the scintillator.

The extended width of the scintillator varies as the scintillator is rotated such that:

$$x = \frac{w}{sin(\theta)} \ [\theta > 0], \tag{5.4}$$

where w is the width of the scintillator (0.6 cm), θ is the angle of the detector relative to the beam line.

With the increase in θ the extended width x of the scintillator, shown in Figure 5.18 (b), decreases, resulting in a decrease in the probability of interaction within the detection volume, ϵ_{det}.

The geometric efficiency is a measure of the proportion of neutrons in the field that are incident on the detector. Assuming the center of the scintillator is at a constant position, the relative geometric efficiency of the detector will be equivalent to the surface area that the scintillator extends, illustrated in Figure 5.18 (a) in red. The relative geometric efficiencies are therefore described by Eq. 5.5:

$$\epsilon_{geom} = w \cdot sin\theta \cdot (L + \frac{x}{2}) \ [\theta > 0], \tag{5.5}$$

where L is the length of the scintillator (12.0 cm). By increasing the angle of rotation θ the geometric efficiency ϵ_{geom} increases as more neutrons are incident on the scintillator.

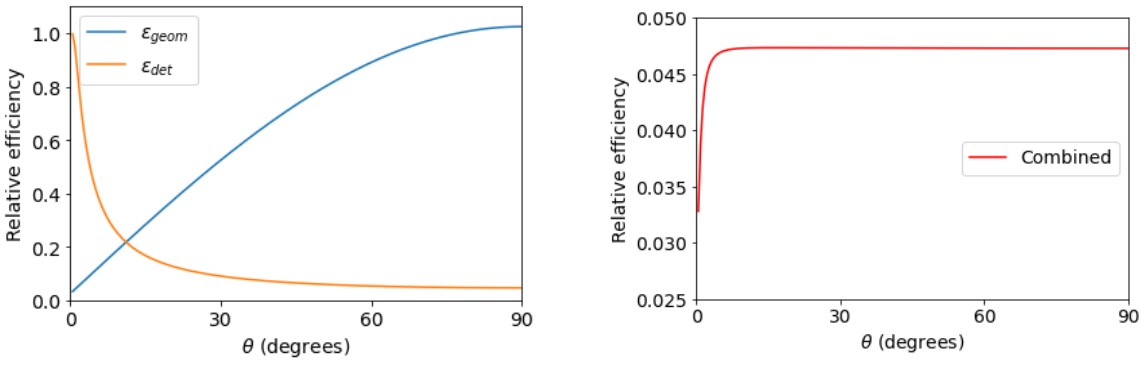

(a) (b)

Figure 5.19: The predicted trend of (a) the relative detection and geometric efficiencies and (b) the total efficiency for $0° < \theta \leq 90°$ using Equations 5.5 and 5.3, were θ is the angle of the detector relative to the axis of the source.

The predicted behaviour of the relative geometric and detection efficiencies for the compact spectrometer in an isotropic field of 15 MeV neutrons are shown in Figure 5.19. The combined efficiency, shown in Figure 5.19 (b), is calculated by taking the product of the geometric and detection efficiencies, which are shown in Figure 5.19 (a). At small angles the total efficiency rapidly increases as the effective area begins to increase and the extended width of the scintillator is close to the maximum. At approximately 10° the combined efficiency begins to plateau and becomes insensitive to θ.

In an experimental setting the combined efficiency affects the measured event rate of the detector. As seen in Table 5.2, the measured event rate of the compact spectrometer as a function of θ agrees with the general trend predicted in Figure 5.19 (b). The event rate at 45° and 90° are within uncertainty of each other and higher than the event rate at 0°. The event rates were calculated as the number of events with L greater than 1 MeV_{ee} normalised by the elapsed time of the acquisition.

Table 5.2: The measured neutron event rate with $L > 1$ MeV_{ee} for 15.100 MeV neutron field with the compact detector rotated at varying angles with respect to the axis of the incident ion beam.

Angle (°)	**Event rate (events/sec)**
0	51 ± 1
45	65 ± 2
90	67 ± 3

The rotation of the detector increases the count rate due to the increase in number of neutrons incident on the scintillator, as defined by ϵ_{geom}. However, the decrease in available path length through the scintillator for large angle scatters when the detector is rotated results in an increase in the number of recoil protons that exit the scintillator before depositing their full energy. Figure 5.20 shows the L-S plots for the measurements taken at the three angles. The regions enclosed in the green dashed lines represent the escaping recoil protons. As seen in both the plots and Table 5.3, the number of events in this region increases as the angle increases. This becomes an issue at higher energies when the range of the recoil protons exceeds the path length available in the scintillator. At 90° the extended width of the scintillator is 0.6 cm, the range of protons with energies greater than 22 MeV exceeds 0.6 cm [165] and as a result all of the recoil protons would escape making it difficult to perform effective spectroscopy.

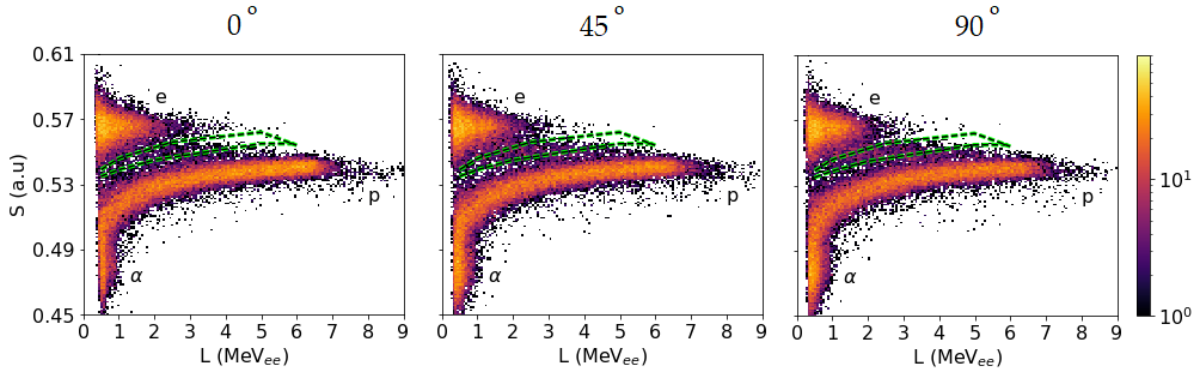

Figure 5.20: Counts as a function of light output parameter L and pulse shape parameter S for events in the compact spectrometer when rotated 0°, 45° and 90° from the axis of the beamline and irradiated with a 15.100 MeV neutron field. The regions enclosed by the green dashed line represent the events associated with escaping recoil protons.

Table 5.3: The percentage of the total events enclosed in the cuts selecting the events associated with escaped protons shown in Figure 5.20, for measurements of 15.100 MeV neutrons made at $\theta = 0°$, 45° and 90° from the beam line.

Angle (°)	**Escaped protons (%)**
0	1.70 ± 0.06
45	2.37 ± 0.07
90	2.67 ± 0.08

Figure 5.21 shows the neutron light output spectra measured with the detector at 0°, 45° and 90° to the beam. There is a slight decrease in edge resolution and a shift to lower L values as the angle relative to the beam increases which is attributed to the increased number of recoil protons which escape without depositing their full energy.

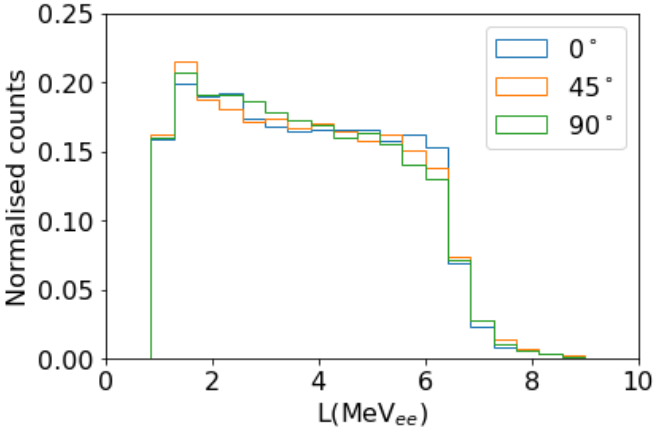

Figure 5.21: Neutron light output spectra of a 15.100 MeV neutron field measured with the compact detector oriented at 0° , 45° and 90° with respect to the beam at 0.655 m from the target normalised to have an area unity.

5.8.3 Multiple SiPMs

It was demonstrated in Section 5.7 that the L resolution has a direct impact on the quality of the unfolded energy spectra. A modified version of the compact spectrometer was constructed using a second SiPM placed on the opposite end of the scintillator. By adding a second SiPM the light collection in the detector improves since the active area for scintillation photon collection was doubled. To utilise the information from both SiPMs and reduce variations in digitised pulse integrals the geometric mean Q_{mean} described by:

$$Q_{mean} = \sqrt{Q_A \times Q_B} \tag{5.6}$$

where Q_A and Q_B are the long integrals of the signals from the two SiPMs A and B respectively [29].

A measurement of the gamma ray field produced by a ^{137}Cs source was made with the modified spectrometer. Figure 5.22 shows the light output spectra obtained from these measurements. Using the geometric mean of the digitised pulses from both SiPMs results in a clear increase in the edge resolution. From a spectroscopy standpoint this is advantageous since it will improve the resolution of the response functions and as a result improve the energy resolution of the unfolded energy spectrum.

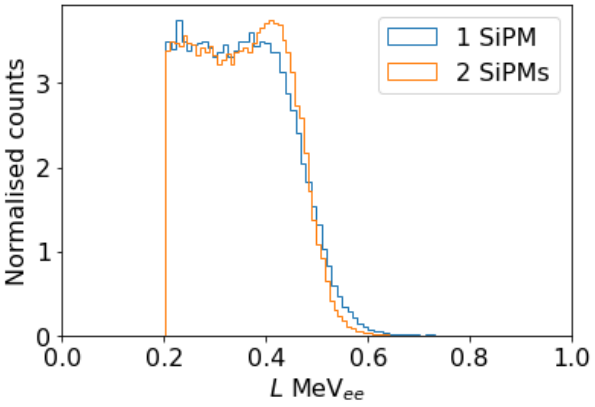

Figure 5.22: Light output spectra of a ^{137}Cs source measured with the modified compact spectrometer with two SiPMs, showing the spectrum obtained from a single SiPM and the spectrum obtained when taking the geometric average of the pulse integrals from both SiPMs.

Chapter 6

Conclusion

A compact neutron spectrometer consisting of a 0.6 × 0.6 × 12 cm^3 EJ-276 plastic scintillator coupled to a single SensL C-series SiPM was constructed. The detector was characterised using measurements of neutrons with energies ranging up to 62.5 MeV performed at three different facilities: the UCT n-lab, IRSN AMANDE and iThemba LABS, with digital data acquisition using a CAEN DT5730 digitiser. The measurements performed at each of the three facilities displayed significant differences in pulse quality due to differing experimental conditions particularly associated with cable length and quality. The differing pulse quality resulted in different optimised short and long integration times intervals being used for the data acquired at each of the three facilities. The detector also exhibited some unexpected and unresolved characteristics in the light output response. For example, the lack of events above 3 MeV_{ee} in measurements of the AmBe gamma ray spectrum which is expected to have a Compton edge at 4.2 MeV_{ee}; and the relationship between the L of gamma rays and neutrons being different to what was observed using the reference detectors.

Despite these challenges the compact detector displayed good quality PSD with the neutron and gamma ray events being easily distinguished from each other. Although, due to the PSD characteristics of the plastic scintillator, the PSD quality was not to the same standard as the reference detectors consisting of a BC-501A or equivalent EJ-301 liquid scintillator coupled to a 12-stage PMT.

Time-of-flight measurements were performed with the neutron field produced by 1.84 MeV deuterons irradiating a deuterium target at AMANDE, and the neutron field produced by 66.0 MeV protons on an 8.0 mm Li target at iThemba LABS. The neutron energy spectra calculated from the ToF with both detector were in good agreement with each other. The compact spectrometer displayed comparable energy resolution to the reference at 5.000 MeV and a marginally lower energy resolution at 62.5 MeV. Using the energy spectrum calculated from the ToF measurements at iThemba LABS and the well known efficiency function of the BC-501A reference, an estimate of the efficiency function for the compact detector was calculated.

Response functions for both detectors were constructed using events at 3 MeV intervals for energies ranging from 11 to 62 MeV. The events were selected using ToF analyses of the measurements performed at iThemba LABS. The response functions were used to unfold the light output spectrum of a field constructed of known quantities of a selection of the response functions, the light output of the 15.100 MeV neutron field at AMANDE and the broad spectrum neutron field at iThemba LABS using the UMG-3.3 unfolding algorithms GRAVEL and MAXED. All three light output spectra were unfolded successfully with the energy spectra being in good agreement with the expected energy spectra. However, the 3 MeV wide range of energies used to build the response functions is quite large and resulted in response functions with significantly lowered edge resolution. The low edge resolution, similarity between response functions at high energies and large energy bins resulted in low resolution unfolded energy spectra. Both the constructed energy spectrum and the 15.100 MeV energy spectrum were unfolded with MAXED using the energy spectrum from GRAVEL unfolding as the default spectrum. The neutron field produced by 66.0 MeV protons on an 8.0 mm Li target at iThemba LABS had limited success when unfolding with GRAVEL and therefore the energy spectrum calculated with ToF with a lower L limit of 1 MeV_{ee} was used as the default spectrum. The unfolded energy spectrum was in good agreement with the expected energy spectrum, the energy spectrum calculated from ToF using a lower L limit of 2.5 MeV_{ee}; indicating that for complex radiation fields a default spectrum that is similar to the expected spectrum should be used for optimum results.

The angular dependence of the compact spectrometer was investigated through measurements of 15.100 MeV neutrons with the detector rotated about its own axis. Larger angles of rotation were found to increase the efficiency of the detector due to the increase in the number of incident neutrons associated with increasing the effective area. Due to the dimensions of the scintillator, the rotation of the detector also resulted in a decrease in the extended width of the scintillator which causes an increase in the number of protons that escape before depositing their full energy. This puts a limitation on the effectiveness of the detector as a spectrometer at larger angles. For example at an angle of 90° the maximum energy that can be effectively detected is roughly 20 MeV. It was found that larger angles of rotation resulted in a lowering of the edge resolution of the neutron light output spectra due to the increase in escaping protons.

6.1 Recommendations and Future Work

The largest impediment to performing high quality neutron spectroscopy with this compact detector was the poor energy and edge resolution of the response functions. The edge resolution of the response functions could be improved by improving the resolution of the detector as a whole. As was demonstrated, the addition of a second SiPM greatly improves the light output resolution. Additionally, acquiring a larger number of events so that well defined response functions can be constructed using a smaller range of neutron energies. The poor pulse quality acquired during the campaign at iThemba LABS is likely to have negatively affected the resolution of the light output. While the pulse quality could be

improved in future measurement campaigns at the facility through using shorter signal cables, an acquisition system in which the signal quality does not vary between facilities would be ideal. Additionally, incorporating a pulsed LED within the detector housing would be beneficial in calibrating the detector. The LED would provide a convenient method of calibrating the detector at any point once an initial gamma ray calibration has been performed. This would mitigate the difficulties with calibration seen in this work and accommodate any changes in the detector response over time or associated with environmental factors such as temperature. Given the context of this project the response matrix should be extended to include energies between 1 and 11 MeV and more measurements should be performed to construct response functions for energies up to 100 MeV.

In an aviation environment the neutron field is disperse and the low efficiency of this detector would result in a very low event rate. Ultimately the efficiency needs to be improved through the use of a larger scintillator for the detector to be effective in such an environment, since a well defined light output spectrum with high statistics is required for spectrum unfolding. Additionally, work needs to be done in making the device more compact. There has already been development on a compact battery-powered power supply which was not discussed in this work. The acquisition system is currently the largest component of the device and is operated using a standard power supply. By having an acquisition contained within the detector, that transfers information through a wireless connection, the detector will not only be more compact but this would also avoid the differences in pulse quality that were observed due to facility-specific factors.

In this thesis the first measurements of neutron fields with energies between 5.000 MeV and 62.5 MeV with this design of the compact detector were presented. The detector system exhibited good quality PSD, excellent timing resolution for obtaining energy spectra through time-of-flight analyses and energy spectra were successfully unfolded using response functions measured with the detector. This work ultimately demonstrated that the simplified, one SiPM design can be effective with a longer scintillator and at higher energies. The low energy resolution from unfolding can be largely improved by simply undertaking an additional measurement campaign at iThemba LABS. Overall, this concept of detector design shows promise and this work provides a robust starting point for future development of the device.

Bibliography

[1] P. Goldhagen, J. Clem, and J. Wilson. The energy spectrum of cosmic-ray induced neutrons measured on an airplane over a wide range of altitude and latitude. *Radiation Protection Dosimetry*, 110:387, 2004.

[2] J. Clem et al. New calculations of the atmospheric cosmic radiation field—results for neutron spectra. *Radiation Protection Dosimetry*, 110:423–428, 2004.

[3] P. Grieder. *Cosmic Rays at Earth: Researcher's reference manual and data book*. Elsevier, 2001.

[4] J. Lochard, D.T. Bartlett, W. Rühm, H. Yasuda, and J.F. Bottollier-Depois. ICRP publication 132: radiological protection from cosmic radiation in aviation. *Annals of the ICRP*, 45(1):5–48, 2016.

[5] D.T. Bartlett. Radiation protection aspects of the cosmic radiation exposure of aircraft crew. *Radiation Protection Dosimetry*, 109(4):349–355, 2004.

[6] M. Bagshaw and P. Illig. The aircraft cabin environment. In *Travel Medicine (Fourth Edition)*, pages 429–436. Elsevier, London, fourth edition edition, 2019.

[7] J.W. Wilson, M. Kim, W. Schimmerling, F.F. Badavi, S.A. Thibeault, F.A. Cucinotta, J.L. Shinn, and R. Kiefer. Issues in space radiation protection: Galactic Cosmic Rays. *Radiation and Environmental Biophysics*, 34:217–222, 1995.

[8] S. Roesler, W. Heinrich, and H. Schraube. Monte carlo calculation of the radiation field at aircraft altitudes. *Radiation Protection Dosimetry*, 98(4):367–388, 2002.

[9] V. Lacoste and S. Taylor, G .and Röttger. Simulated workplace neutron fields. *Metrologia*, 48(6):S304, 2011.

[10] J.F. Bottollier-Depois, E. Allain, G. Baumont, N. Berthelot, G. Darley, F. Ecrabet, T. Jolivet, A. Lebeau-Livé, V. Lejeune, F. Quéinnec, et al. The OpenRadiation project: monitoring radioactivity in the environment by and for the citizens. *Radioprotection*, 54(4):241–6, 2019.

[11] F. Trompier et al. Citizen science approach for galactic cosmic radiation and SEP monitoring at commercial flight altitude: Scientific context, data collected and calibration aspects [online]. http://dx.doi.org/10.13140/RG.2.2.32620.03208.

[12] The cosmic on air project. https://cosmic-on-air.org/.

[13] B.J. Clewer, K.A. Ryden, A.C.R. Dyer, A.D.P. Hands, and D.R. Jackson. A citizen science network for measurements of atmospheric ionizing radiation levels. *Space Weather*, 17(6):877–893, 2019.

[14] J.M. Clem, G. De Angelis, P. Goldhagen, and J.W. Wilson. New calculations of the atmospheric cosmic radiation field—results for neutron spectra. *Radiation Protection Dosimetry*, 110(1-4):423–428, 2004.

[15] V. Kortov. Materials for thermoluminescent dosimetry: Current status and future trends. *Radiation Measurements*, 42(4-5):576–581, 2007.

[16] T. Straume, L.A. Braby, T.B. Borak, T. Lusby, D.W. Warner, and D. Perez-Nunez. Compact tissue-equivalent proportional counter for deep space human missions. *Health Physics*, 109(4):277, 2015.

[17] B.M. Hayes, O.I. Causey, B.B. Gersey, and E.R. Benton. Active Tissue Equivalent Dosimeter: A Tissue Equivalent Proportional Counter flown onboard the International Space Station. *Nuclear Instruments and Methods in Physics Research Section A: Accelerators, Spectrometers, Detectors and Associated Equipment*, 1028:166389, 2022.

[18] P. Goldhagen, M. Reginatto, T. Kniss, J.W. Wilson, R.C. Singleterry, I.W. Jones, and W. Van Steveninck. Measurement of the energy spectrum of cosmic-ray induced neutrons aboard an ER-2 high-altitude airplane.

[19] T. Nakamura, T. Nunomiya, and M. Sasaki. Development of active environmental and personal neutron dosemeters. *Radiation Protection Dosimetry*, 110(1-4):169–181, 2004.

[20] M. Takada, K. Yajima, H. Yasuda, T. Sato, and T. Nakamura. Measurement of atmospheric neutron and photon energy spectra at aviation altitudes using a phoswich-type neutron detector. *Journal of Nuclear Science and Technology*, 47(10):932–944, 2010.

[21] S Agosteo, C Birattari, Giovanni D'Angelo, F Dal Corso, A Foglio Para, I Lippi, Andrea Pola, and Pierluigi Zotto. Neutron spectrometry with a recoil radiator-silicon detector device. *Nuclear Instruments and Methods in Physics Research Section A: Accelerators, Spectrometers, Detectors and Associated Equipment*, 515(3):589–604, 2003.

[22] Alberto Fazzi, Stefano Agosteo, Andrea Pola, Vincenzo Varoli, and Pierluigi Zotto. Pulse discrimination between recoil protons and secondary electrons for a silicon diode based neutron spectrometer. *IEEE Transactions on Nuclear Science*, 51(3):1049–1055, 2004.

[23] D.J. Lawrence, B.J. Anderson, D.N. Baker, W.C. Feldman, G.C. Ho, H. Korth, R.L. McNutt Jr, P.N. Peplowski, S.C. Solomon, R.D. Starr, et al. Comprehensive

survey of energetic electron events in Mercury's magnetosphere with data from the MESSENGER Gamma-Ray and Neutron Spectrometer. *Journal of Geophysical Research: Space Physics*, 120(4):2851–2876, 2015.

[24] T.H. Prettyman et al. Gamma-ray and neutron spectrometer for the Dawn mission to 1 Ceres and 4 Vesta. *IEEE Transactions on Nuclear Science*, 50(4):1190–1197, 2003.

[25] L.H. Heilbronn, T.B. Borak, L.W. Townsend, P. Tsai, C.A. Burnham, and R.A. McBeth. Neutron yields and effective doses produced by galactic cosmic ray interactions in shielded environments in space. *Life Sciences in Space Research*, 7:90–99, 2015.

[26] E.R. Benton, E.V. Benton, and A.L. Frank. Neutron dosimetry in low-earth orbit using passive detectors. *Radiation Measurements*, 33(3):255–263, 2001.

[27] J. Köhler et al. Measurements of the neutron spectrum on the Martian surface with MSL/RAD. *Journal of Geophysical Research: Planets*, 119(3):594–603, 2014.

[28] A. Buffler, A.C. Comrie, F.D. Smit, and H.J. Wörtche. Neutron Spectrometry with EJ299-33 Plastic Scintillator for $E_n = 10-100$ MeV. *IEEE Transactions on Nuclear Science*, 62(3):1422–1428, 2015.

[29] A. Comrie. *A new compact neutron spectrometer*. PhD thesis, University of Cape Town, 2016.

[30] C. Sole. *A new digital data acquisition system for neutron metrology*. Master's thesis, University of Cape Town, 2022.

[31] A.C. Comrie, A. Buffler, F.D. Smit, and H.J. Wörtche. Digital neutron/gamma discrimination with an organic scintillator at energies between 1 MeV and 100 MeV. *Nuclear Instruments and Methods in Physics Research Section A: Accelerators, Spectrometers, Detectors and Associated Equipment*, 772:43–49, 2015.

[32] A. Comrie, A. Buffler, R. Smit, and H. Wörtche. Tests of pulse shape discrimination with EJ299-33 plastic scintillator for use in portable spectroscopy. *Proceedings of Technology and Instrumentation in Particle Physics 2014 (TIPP2014). 2-6 June 2014. Amsterdam*, page 251, 2014.

[33] A. Buffler, A.C. Comrie, T. Hutton, F.D. Smit, and R. Nolte. Towards a new compact scintillation spectrometer for 100 MeV neutrons: A case study for reference neutron beams. *IAEA TECDOC SERIES*, page 209, 2020.

[34] E. Jarvie, A. Buffler, T. Hutton, Z. Ndabeni, R. Nndanganeni, and C. Vandevoorde. A compact neutron spectrometer for neutrons produced by cosmic rays. *Proceedings of South African Institute of Physics (SAIP) Conference*, pages 157–162, 2021.

[35] E. Jarvie. A new compact neutron spectrometer. Honours Thesis, University of Cape Town, 2020.

[36] E. Jarvie, T. Hutton, A. Buffler, Z. Ndabeni, R. Nndanganeni, and C. Vandevoorde. Measuring response functions for a new compact neutron spectrometer. In *The proceedings of the 28th International Nuclear Physics Conference (INPC 2022), Cape Town, South Africa, 11-16 September 2023*. Under review.

[37] E. Regener and G. Pfotzer. Intensity of the cosmic ultra-radiation in the stratosphere with the tube-counter. *Nature*, 133(364), 1934.

[38] O.A. Danilova, I.M. Demina, N.G. Ptitsyna, et al. Mapping of Geomagnetic Cutoff Rigidity of Cosmic Rays during the Main Phase of the Magnetic Storm of November 20, 2003. *Geomagnetism and Aeronomy*, 59:147–154, 2019.

[39] M. Gerontidou, N. Katzourakis, H. Mavromichalaki, V. Yanke, and E. Eroshenko. World grid of cosmic ray vertical cut-off rigidity for the last decade. *Advances in Space Research*, 67(7):2231–2240, 2021.

[40] P. Bilski, P. Olko, and T. Horwacik. Air-crew exposure to cosmic radiation on board of Polish passenger aircraft. *NUKLEONIKA*, 49(2), 2004.

[41] J.J. Aw et al. Cosmic radiation and commercial air travel. *Journal of Travel Medicine*, 10(1):19–28, 2003.

[42] W. Heinrich, S. Roesler, and H. Schraube. Physics of cosmic radiation fields. *Rad. Prot. Dosim.*, 86(4):253–258, 1999.

[43] EURADOS Working Group 5. Cosmic Radiation Exposure of Aircraft Crew. Technical report, European Commission, 2004.

[44] A.M. Hillas. Cosmic rays: Recent progress and some current questions. *arXiv preprint astro-ph/0607109*, 2006.

[45] J.A. Simpson. Elemental and isotopic composition of the galactic cosmic rays. *Annual Review of Nuclear and Particle Science*, 1983.

[46] M.J. Aschwanden. Chapter 11 - The Sun. In *Encyclopedia of the Solar System (Third Edition)*, pages 235–259. Elsevier, Boston, 2014.

[47] S.I. Akasofu. An essay on sunspots and solar flares. *Planetary and Space Science*, 32(11):1469–1496, 1984.

[48] M.J. Owens and R.J. Forsyth. The heliospheric magnetic field. *Living Reviews in Solar Physics*, 10(5), 2013.

[49] C.T. Russell. The solar wind interaction with the Earth's magnetosphere: A tutorial. *IEEE Transactions on Plasma Science*, 28(6):1818–1830, 2000.

[50] M. Potgieter. Solar Modulation of Cosmic Rays. *Living Reviews in Solar Physicss*, 10(3), 2013.

[51] E.N. Parker. The passage of energetic charged particles through interplanetary space. *Planetary and Space Science*, 13(1):9–49, January 1965.

[52] Cosmic Ray Station of the University of Oulu/Sodankyla Geophysical Observatory. Website: http://cosmicrays.oulu.fi/.

[53] K.L. Klein and S. Dalla. Acceleration and Propagation of Solar Energetic Particles. *Space Science Reviews*, 212(3-4):1107–1136, 2017.

[54] D.V. Reames. *[Lecture Notes in Physics] Solar Energetic Particles*, volume 932. Springer, 2017.

[55] M.G. Mosotho, R.D. Strauss, R.R. Nndanganeni, and J.P. van den Berg. The North-West University's High Altitude Radiation Monitor programme. *South African Journal of Science*, 117(7561), 2021.

[56] B. Klecker. Current understanding of SEP acceleration and propagation. *Journal of Physics: Conference Series*, (409), 2013.

[57] L. Miroshnichenko and J. Perez-Peraza. Astrophysical aspects in the studies of solar cosmic rays. *International Journal of Modern Physics A*, 23(1):1–141, 2007.

[58] D. Reames. Helium Suppression in Impulsive Solar Energetic-Particle Events. *Solar Physics*, 294, 03 2019.

[59] D.V. Reames. Particle acceleration at the Sun and in the heliosphere . *Space Science Reviews*, 90:413–491, 1999.

[60] R. Schwenn. Space Weather: The Solar Perspective. *Living Reviews in Solar Physics*, 3(2), 2006.

[61] C. Salas-Matamoros and K.L. Klein. On the statistical relationship between CME speed and soft X-ray flux and fluence of the associated flare. *Solar Physics*, 290(5):1337–1353, 2015.

[62] M. Tokumaru, M. Kojima, and K. Fujiki. Solar cycle evolution of the solar wind speed distribution from 1985 to 2008. *Journal of Geophysical Research: Space Physics*, 115(A4), 2010.

[63] J.T. Gosling, J.R. Asbridge, S.J. Bame, and W.C. Feldman. Solar wind speed variations: 1962–1974. *Journal of Geophysical Research*, 81(28):5061–5070, 1976.

[64] K.L. Klein and G. Mann. Shock waves and coronal mass ejections. In *Coronal Physics from Radio and Space Observations*, pages 161–180. Springer, 1997.

[65] D. Reames. Solar Energetic Particles: Is there time to hide? *Radiation Measurements*, 30(3):297–308, 1999.

[66] Geomagnetic storms. The National Oceanic and Atmospheric Administration, Space weather prediction center. Accessed online: https://www.swpc.noaa.gov/phenomena/geomagnetic-storms.

[67] G.S. Lakhina and B.T. Tsurutani. Geomagnetic storms: historical perspective to modern view. *Geoscience Letters*, 3(5):1–11, 2016.

[68] W. D. Gonzalez, J. A. Joselyn, Y. Kamide, H. W. Kroehl, G. Rostoker, B. T. Tsurutani, and V. M. Vasyliunas. What is a geomagnetic storm? *Journal of Geophysical Research: Space Physics*, 99(A4):5771–5792, 1994.

[69] G. Rostoker, E. Friedrich, and M. Dobbs. *Physics of magnetic storms*, pages 149–160. AGU, 1997.

[70] J.B. Zirker. Coronal holes and high-speed wind streams. *Reviews of Geophysics*, 15(3):257–269, 1977.

[71] J.P. Eastwood, T.D. Phan, M. Øieroset, M.A. Shay, K. Malakit, M. Swisdak, J.F. Drake, and A. Masters. Influence of asymmetries and guide fields on the magnetic reconnection diffusion region in collisionless space plasmas. *Plasma Physics and Controlled Fusion*, 55(12):124001, 2013.

[72] T. Kuwabara, J.W. Bieber, J. Clem, et al. Real-time cosmic ray monitoring system for space weather. *Space Weather: The International Journal of Research and Applications*, 4(8), 2006.

[73] I.G. Usoskin, A. Gil, G.A. Kovaltsov, A.L. Mishev, and V.V. Mikhailov. Heliospheric modulation of cosmic rays during the neutron monitor era: Calibration using PAMELA data for 2006-2010. *Journal of Geophysical Research: Space Physics*, 122(4):3875–3887, 2017.

[74] D.T. Strauss et al. The mini-neutron monitor: a new approach in neutron monitor design. *Journal of Space Weather and Space Climate*, 10:39, 2020.

[75] R. Bütikofer. Ground-based measurements of energetic particles by neutron monitors. *Solar Particle Radiation Storms Forecasting and Analysis: The HESPERIA HORIZON 2020 Project and Beyond*, pages 95–111, 2018.

[76] H. Moraal. Cosmic-ray modulation equations. *Space Science Reviews*, 176(1):299–319, 2013.

[77] R.M. Robinson and R.A. Behnke. The US National Space Weather Program: A retrospective. *Washington DC American Geophysical Union Geophysical Monograph Series*, 125:1–10, 2001.

[78] What is space weather? South African National Space Agency, https://spaceweather.sansa.org.za/space-weather-information/about-space-weather/what-is-space-weather.

[79] A. Hanslmeier. The sun and space weather. In *Heliophysical Processes*, pages 233–249. Springer, 2010.

[80] F.A. Cucinotta and M. Durante. Cancer risk from exposure to galactic cosmic rays: implications for space exploration by human beings. *The Lancet Oncology*, 7(5):431–435, 2006.

[81] E.M. Kennedy, D.R. Powell, Z. Li, et al. Galactic Cosmic Radiation Induces Persistent Epigenome Alterations Relevant to Human Lung Cancer. *Scientific Reports*, 8(6709), 2018.

[82] F.A. Cucinotta, W. Schimmerling, E.A. Blakely, and T.K. Hei. A proposed change to astronaut exposures limits is a giant leap backwards for radiation protection. *Life Sciences in Space Research*, 31:59–70, 2021.

[83] T. Straume. *Medical concerns with space radiation and radiobiological effects*, pages 243–257. Springer International Publishing, 2015.

[84] G. Baiocco et al. The origin of neutron biological effectiveness as a function of energy. *Scientific Reports*, 22(6), 2016.

[85] E.C. Friedberg, G.C. Walker, W. Siede, R.D. Wood, R.A. Schultz, and T. Ellenberger. *DNA repair and mutagenesis*. ASM Press, 2006.

[86] R.A. Powsner, M.R. Palmer, and E.R. Powsner. *Essentials of nuclear medicine physics and instrumentation*. John Wiley & Sons, 2013.

[87] S.A. Lorimore, P.J. Coates, and E.G. Wright. Radiation-induced genomic instability and bystander effects: inter-related nontargeted effects of exposure to ionizing radiation. *Oncogene*, 22(45):7058–7069, 2003.

[88] J. Valentin. Relative biological effectiveness (RBE), quality factor (Q), and radiation weighting factor (w R) ICRP Publication 92: Approved by the Commission in January 2003. *Annals of the ICRP*, 33(4):1–121, 2003.

[89] W.W. Kuhne, B.B. Gerse, R. Wilkins, H. Wu, S.A. Wender, V. George, and W.S. Dynan. Biological effects of high-energy neutrons measured in vivo using a vertebrate model. *Radiation Research*, 172(4), 2009.

[90] P.P. Urone. *Physics with health science applications*. John Wiley & Sons, 1985.

[91] L.W. Townsend and R.J.M. Fry. Radiation protection guidance for activities in low-earth orbit. *Advances in Space Research*, 30(4):957–963, 2002.

[92] J.N. Pelton. Basics of Solar and Cosmic Radiation and Hazards. In *Handbook of Cosmic Hazards and Planetary Defense*, pages 243–257. Springer, 2015.

[93] J.W. Wilson. *Environmental geophysics and SPS shielding*. University of California, 1978.

[94] E. Lynge. Commentary: cancer in the air. *International Journal of Epidemiology*, 30(4):830–832, 2001.

[95] O. Tokumaru, K. Haruki, K. Bacal, T. Katagiri, T. Yamamoto, and Y. Sakurai. Incidence of cancer among female flight attendants: a meta analysis. *Journal of Travel Medicine*, 13(3):127–132, 2006.

[96] K. Kojo. Occupational cosmic radiation exposure and cancer in airline cabin crew. Dissertation, School of Health Sciences of the University of Tampere, Helsinki, Finiland, 2013.

[97] C. Savvidis and M. Koutsilieris. Circadian rhythm disruption in cancer biology. *Molecular Medicine*, 18(9):1249–1260, 2012.

[98] R.G. Stevens et al. Meeting report: the role of environmental lighting and circadian disruption in cancer and other diseases. *Environmental Health Perspectives*, 115(9):1357–1362, 2007.

[99] S. Gandini, E. Botteri, S. Iodice, M. Boniol, A.B. Lowenfels, P. Maisonneuve, and P. Boyle. Tobacco smoking and cancer: a meta-analysis. *International Journal of Cancer*, 122(1):155–164, 2008.

[100] T. Hirayama. Diet and cancer. *Nutrition and Cancer*, 1(3):67–81, 1979.

[101] F. Timischl. Interaction of Mixed High Energy Radiation with Semiconductor Materials and Electronic Components. Graz University of Technology.

[102] S.J. Pearton, F. Ren, E. Patrick, M.E. Law, and A.Y. Polyakov. Review—Ionizing Radiation Damage Effects on GaN Devices. *ECS Journal of Solid State Science and Technology*, 5(Q35), 2016.

[103] B. Todd and S. Uznanski. Radiation risks and mitigation in electronic systems. In *Proceedings of the CAS-CERN Accelerator School: Power Converters*, 2015.

[104] A. Karmakar, J. Wang, J. Prinzie, V. De Smedt, and P. Leroux. A review of semiconductor based ionising radiation sensors used in harsh radiation environments and their applications. *Radiation*, 1(3):194–217, 2021.

[105] J.G. Kappernman and V.D. Albertson. Bracing for the geomagnetic storms. *IEEE Spectrum*, 27(3):27–33, 1990.

[106] R. Pirjola. *Research of geomagnetically induced currents as ground effects of space weather*, pages 94–97. 2014.

[107] Recommendations of the International Commission on Radiological Protection. ICRP. *Annals of the ICRP*, 21(1-3), 1991.

[108] Ionizing radiation exposure of the population of the United States. Technical Report 160, 2009.

[109] Evaluation of the implementation of radiation protection measures for aircrew. European Commission. Radiation Protection, Report 156.

[110] National Nuclear Regulator Act. Republic of South Africa, Act 46, 1999.

[111] SAHPRA. Radiation control. https://www.sahpra.org.za/radiation-control/, 19 September 2022.

[112] R. Nndanganeni, South African National Space Agency. Private communication, 2023.

[113] M.M. Meier and D. Matthiä. Assessment of the skin dose for aircrew. *Journal of Radiological Protection*, 37(2):321, 2017.

[114] IAEA Safety Report Series No. 115. Neutron Monitoring For Radiation Protection. Technical report, International Atomic Energy Agency, 2021.

[115] D.T. Bartlett, L.G. Hager, D. Irvine, and M.F Bagshaw. Measurements on concorde of the cosmic radiation field at aviation altitudes. *Radiation protection dosimetry*, 91(4):365–376, 2000.

[116] P. Lantos, N. Fuller, and J.F. Bottollier-Depois. Methods for estimating radiation doses received by commercial aircrew. *Aviation, Space, and Environmental Medicine*, 74(7):746–752, 2003.

[117] C.J. Mertens, M.M. Meier, S. Brown, R.B. Norman, and X. Xu. NAIRAS aircraft radiation model development, dose climatology, and initial validation. *Space Weather*, 11(10):603–635, 2013.

[118] A. Mishev, F. Adibpour, I. Usoskin, and E. Felsberger. Computation of dose rate at flight altitudes during ground level enhancements no. 69, 70 and 71. *Advances in Space Research*, 55, 01 2015.

[119] Pierre Lantos and Nicolas Fuller. History of the solar particle event radiation doses on-board aeroplanes using a semi-empirical model and concorde measurements. *Radiation Protection Dosimetry*, 104(3):199–210, 2003.

[120] F.S. Preston. Eight years' experience of concorde operations: medical aspects. *Journal of the Royal Society of Medicine*, 78(3):193–196, 1985.

[121] DM Davies. Cosmic radiation in concorde operations and the impact of new icrp recommendations on commercial aviation. *Radiation Protection Dosimetry*, 48(1):121–124, 1993.

[122] IJ Wilson and RC Eustace. Evaluation of 2 possible further developments of the uk in-flight radiation warning meter for ssts. In *NASA, Washington Proc. of the Natl. Symp. on Nat. and Manmade Radiation in Space*, 1972.

[123] H. Kallmann. Natur und Technik, July, 1947. *Z. Naturforsch. 2a*, 439:642, 1947.

[124] G.N. Harding. A scintillation counter for detecting fast neutrons. *Nature*, 167(4246):437–437, 1951.

[125] L.M. Bollinger, G.E. Thomas, and R.R. Palmer. Application of a liquid scintillation neutron detector to time-of-flight spectroscopy. In *Physical review*, volume 91, pages 452–452. American Physical Soc., 1953.

[126] F.D. Brooks. Development of organic scintillators. *Nuclear Instruments and Methods*, 162(1-3):477–505, 1979.

[127] J.B. Birks. *The theory and practice of scintillation counting: International series of monographs in electronics and instrumentation*, volume 27. Elsevier, 2013.

[128] J.B. Birks. Scintillations from organic crystals: specific fluorescence and relative response to different radiations. *Proceedings of the Physical Society. Section A*, 64(10):874, 1951.

[129] T. Murai, T. Nakamura, and A. Yamamoto. A new method of integral dose measurement with a plastic scintillator phantom. *Journal of radiation research*, 5(1):23–34, 1964.

[130] H. Klein and S. Neumann. Neutron and photon spectrometry with liquid scintillation detectors in mixed fields. *Nuclear Instruments and Methods in Physics Research Section A: Accelerators, Spectrometers, Detectors and Associated Equipment*, 476(1-2):132–142, 2002.

[131] K.S. Krane and W.G. Lynch. Introductory nuclear physics. *Physics Today*, 42(1):78, 1989.

[132] G. Knoll. *Radiation Detection and Measurement*, chapter 2, Radiation Interactions. Wiley, 3rd edition, 2010.

[133] G. Knoll. *Radiation Detection and Measurement*, chapter 15, Fast Neutron Detection and Spectroscopy. Wiley, 3rd edition, 2010.

[134] T. Gozani et al. Principles and applications of neutron-based inspection techniques. *Nuclear Instruments & Methods in Physics Research*, 261(1-2):311–315, 2007.

[135] J.A. Lockwood, C. Chen, L.A. Friling, D. Swartz, R.N. Onge, A. Galonsky, and R.R. Doering. Response functions of organic scintillators to high energy neutrons. *Nuclear Instruments and Methods*, 138(2):353–362, 1976.

[136] H.A. Bethe and J. Ashkin. Experimental nuclear physics. *Wiley, New York*, 1953.

[137] G. Knoll. *Radiation Detection and Measurement*. Wiley, 3rd edition, 2010.

[138] O. Klein and Y. Nishina. The scattering of light by free electrons according to Dirac's new relativistic dynamics. *Nature*, 122(3072):398–399, 1928.

[139] F. Cottini, C. Raimondi, and E. Rapisarda. Compton effect measurements. Elementary Particle Laboratory, University of Milano, Italy, 2007.

[140] S.C. Curran and J. D. Craggs. *Counting tubes: theory and applications*. Academic Press, 1949.

[141] W.R. Leo. *Techniques for nuclear and particle physics experiments: a how-to approach*. Springer Science & Business Media, 2012.

[142] G. Knoll. *Radiation Detection and Measurement*, chapter 9, Photomultiplier Tubes and Photodiodes, pages 265–283. Wiley, 2010.

[143] Z.Y. Sadygov, M.K. Suleimanov, and T.Y. Bokova. Supersensitive avalanche silicon drift photodetector. *arXiv preprint hep-ex/9909017*, 1999.

[144] Z. Sadygov, A. Sadigov, and S. Khorev. Silicon photomultipliers: Status and prospects. *Physics of Particles and Nuclei Letters*, 17(2):160–176, 2020.

[145] onsemi, Introduction to the Silicon Photomultiplier (SiPM), AND9770/D. https://www.onsemi.com/pub/Collateral/AND9770-D.PDF.

[146] C. Piemonte and A. Gola. Overview on the main parameters and technology of modern silicon photomultipliers. *Nuclear Instruments and Methods in Physics Research Section A: Accelerators, Spectrometers, Detectors and Associated Equipment*, 926:2–15, 2019.

[147] P. Eckert, H.C. Schultz-Coulon, W. Shen, R. Stamen, and A. Tadday. Characterisation studies of silicon photomultipliers. *Nuclear Instruments and Methods in Physics Research Section A: Accelerators, Spectrometers, Detectors and Associated Equipment*, 620(2-3):217–226, 2010.

[148] B. Dolgoshein, V. Balagura, P. Buzhan, M. Danilov, L. Filatov, E. Garutti, M. Groll, A. Ilyin, V. Kantserov, V. Kaplin, et al. Status report on silicon photomultiplier development and its applications. *Nuclear Instruments and Methods in Physics Research Section A: Accelerators, Spectrometers, Detectors and Associated Equipment*, 563(2):368–376, 2006.

[149] J.R.D. Copley and T.J. Udovic. Neutron time-of-flight spectroscopy. *Journal of research of the National Institute of Standards and Technology*, 98(1):71, 1993.

[150] S. Lim, D. Kim, J. Kang, J. Dang, P. Lee, G. Kim, K. Chung, and Y.S. Hwang. Development of neutron time-of-flight measurement system for 1.7-mv tandem proton accelerator with lithium target. *Nuclear Engineering and Technology*, 54(2):437–441, 2022.

[151] M. Cavallaro, C. Agodi, M. Assié, F. Azaïez, F. Cappuzzello, D. Carbone, N. De Séréville, A. Foti, L. Pandola, J.A. Scarpaci, et al. Neutron decay of 15C resonances by measurements of neutron time-of-flight. *Physical Review C*, 93(6):064323, 2016.

[152] G. Knoll. *Radiation Detection and Measurement*, chapter 18, Spectrum Analysis, pages 704–706. Wiley, 3rd edition, 2010.

[153] C. Pioch, V. Mares, and W. Rühm. Influence of Bonner sphere response functions above 20 MeV on unfolded neutron spectra and doses. *Radiation Measurements*, 45(10):1263–1267, 2010.

[154] A. Cheminet, V. Lacoste, V. Gressier, G. Hubert, A. Martin, and M. Pépino. Characterization of the IRSN neutron multisphere spectrometer (HERMEIS) at European standard calibration fields. *Journal of Instrumentation*, 7(04):C04007, 2012.

[155] W. Rühm, V. Mares, C. Pioch, S. Agosteo, A. Endo, M. Ferrarini, I. Rakhno, S. Rollet, D. Satoh, and H. Vincke. Comparison of Bonner sphere responses calculated by different Monte Carlo codes at energies between 1 MeV and 1 GeV–Potential impact on neutron dosimetry at energies higher than 20 MeV. *Radiation Measurements*, 67:24–34, 2014.

[156] Eljen technologies, products. https://eljentechnology.com/products/plastic-scintillators/ej-276.

[157] F. Shen, Y. Pan, Q. Fu, S. Lin, T. Huang, and W. Wang. PSD performance of EJ-276 and EJ-301 scintillator readout with SiPM array. *Nuclear Instruments and Methods in Physics Research Section A: Accelerators, Spectrometers, Detectors and Associated Equipment*, 1039:167148, 2022.

[158] E.V. Ryabeva, I.V. Urupa, E.E. Lupar, V.V. Kadilin, A.V. Skotnikova, Y.A. Kokorev, and R.F. Ibragimov. Calibration of EJ-276 plastic scintillator for neutron–gamma pulse shape discrimination experiments. *Nuclear Instruments and Methods in Physics Research Section A: Accelerators, Spectrometers, Detectors and Associated Equipment*, 1010:165495, 2021.

[159] M.P. Taggart, C. Payne, and P.J. Sellin. Neutron-gamma discrimination via psd plastic scintillator and sipms. In *Journal of Physics: Conference Series*, volume 763, page 012007. IOP Publishing, 2016.

[160] SensL C-series data sheet. https://sensl.com/downloads/ds/DS-MicroCseries.pdf.

[161] G. Bondarenko, B. Dolgoshein, V. Golovin, A. Ilyin, R. Klanner, and E. Popova. Limited geiger-mode silicon photodiode with very high gain. *Nuclear Physics B-Proceedings Supplements*, 61(3):347–352, 1998.

[162] BK Precision Corporation, Products, Model 1550 power supply. https://www.bkprecision.com/products/power-supplies/1550.

[163] Eljen Technologies, Products. https://eljentechnology.com/products/liquid-scintillators/ej-301-ej-309.

[164] CAEN desktop digitizers. https://www.caen.it/desktop-digitizers/.

[165] P. Jipsen, J. Maritz, and D. Steyn. Program ELOSS V2.0.1.

[166] A new DT neutron facility at UCT.

[167] S. Mhlongo, A. Buffler, T. Hutton, and Z. Ndabeni. A new fast neutron facility for materials analysis at UCT. In *The Proceedings of the SAIP Conference 2021*, 2021.

[168] A. Buffler, T. Hutton, T. Leadbeater, M. Alexander, and S. Dlamini. Neutron transmission studies for concrete used in the nuclear industry. In *International Journal of Modern Physics: Conference Series*, volume 50, page 2060015. World Scientific, 2020.

[169] I. Murata, I. Tsuda, R. Nakamura, S. Nakayama, M. Matsumoto, and H. Miyamaru. Neutron and gamma-ray source-term characterization of AmBe sources in Osaka University. *Progress in Nuclear Science and Technology*, 4:345–348, 2014.

[170] K.W. Geiger and L. Van der Zwan. Radioactive neutron source spectra from 9Be (α, n) cross section data. *Nuclear Instruments and Methods*, 131(2):315–321, 1975.

[171] T. Hutton, E. Jarvie, and A. Buffler. A portable neutron spectrometer: first measurements and applications. Poster presented at: The IOP Joint APP, HEPP and NP Conference, 12-15 April 2021, Edinburgh.

[172] V. Gressier, J.F. Guerre-Chaley, V. Lacoste, L. Lebreton, G. Pelcot, J.L. Pochat, T. Bolognese-Milstajn, and D. Champion. AMANDE: a new facility for monoenergetic neutron fields production between 2 keV and 20 MeV. *Radiation Protection Dosimetry*, 110(1-4):49–52, 2004.

[173] V. Gressier, B. Asselineau, J.F. Guerre-Chaley, A. Martin, and H. Muller. AMANDE accelerator energy performances. *Proceedings of Science FNDA2006*, 61, 2006.

[174] Saint gobain crystals. https://www.crystals.saint-gobain.com/radiation-detection-scintillators/liquid-scintillators/neutron-gamma-psd-bc-501a-bc-519.

[175] J. Taforeau, S. Higueret, D. Husson, L. Lebreton, T. Lê, and M. Petit. A new recoil proton telescope for characterisation of energy and fluence of fast neutron fields. *Journal of Instrumentation - J INSTRUM*, 7, 04 2012.

[176] F. Azaïez, R. Nchodu, R.I Nemutudi, and M. Wiedeking. iThemba LABS. *Nuclear Physics News*, 30(4):5–11, 2020.

[177] M. Mosconi, E. Musonza, A. Buffler, R. Nolte, S. Röttger, and F.D. Smit. Characterisation of the high-energy neutron beam at iThemba LABS. *Radiation Measurements*, 45(10):1342–1345, 2010.

[178] N. Ndlovu, A. Boso, A. Buffler, D. Geduld, T. Hutton, V. Lacoste, T. Leadbeater, P. Maleka, F. Smit, et al. Upgrade of the iThemba LABS Neutron Beam Vault to a Metrology Facility. In *22nd Int. Conf. on Cyclotrons and their Applications (Cyclotrons' 19), Cape Town, South Africa, 23-27 September 2019*, pages 181–184. JACOW Publishing, Geneva, Switzerland, 2020.

[179] F.D. Brooks, R.W. Pringle, and B.L. Funt. Pulse shape discrimination in a plastic scintillator. *IRE Transactions on Nuclear Science*, 7(2/3):35–38, 1960.

[180] B. D'Mellow, M.D. Aspinall, R.O. Mackin, M.J. Joyce, and A.J. Peyton. Digital discrimination of neutrons and γ-rays in liquid scintillators using pulse gradient analysis. *Nuclear Instruments and Methods in Physics Research Section A: Accelerators, Spectrometers, Detectors and Associated Equipment*, 578(1):191–197, 2007.

[181] L.F. Miller, J. Preston, S. Pozzi, M. Flaska, and J. Neal. Digital pulse shape discrimination. *Radiation Protection Dosimetry*, 126(1-4):253–255, 2007.

[182] T.S. Sanderson, C.D. Scott, M. Flaska, J.K. Polack, and S.A. Pozzi. Machine learning for digital pulse shape discrimination. In *2012 IEEE Nuclear Science Symposium and Medical Imaging Conference Record (NSS/MIC)*, pages 199–202. IEEE, 2012.

[183] P.A. Söderström, J. Nyberg, and R. Wolters. Digital pulse-shape discrimination of fast neutrons and γ rays. *Nuclear Instruments and Methods in Physics Research Section A: Accelerators, Spectrometers, Detectors and Associated Equipment*, 594(1):79–89, 2008.

[184] S.D. Jastaniah and P.J. Sellin. Digital techniques for n/γ pulse shape discrimination and capture-gated neutron spectroscopy using liquid scintillators. *Nuclear Instruments and Methods in Physics Research Section A: Accelerators, Spectrometers, Detectors and Associated Equipment*, 517(1-3):202–210, 2004.

[185] SD Jastaniah and PJ Sellin. Digital pulse-shape algorithms for scintillation-based neutron detectors. *IEEE transactions on Nuclear Science*, 49(4):1824–1828, 2002.

[186] MP Taggart and PJ Sellin. Comparison of the pulse shape discrimination performance of plastic scintillators coupled to a sipm. *Nuclear Instruments and Methods in Physics Research Section A: Accelerators, Spectrometers, Detectors and Associated Equipment*, 908:148–154, 2018.

[187] B. Wan et al. Digital pulse shape discrimination methods for n-γ separation in an EJ-301 liquid scintillation detector. *Chinese Physics C*, 39(11):116201, 2015.

[188] M.J. Joyce, M.D. Aspinall, F.D. Cave, and A.D. Lavietes. Real-time, digital pulse-shape discrimination in non-hazardous fast liquid scintillation detectors: Prospects for safety and security. *IEEE Transactions on Nuclear Science*, 59(4):1245–1251, 2012.

[189] M.J. Joyce, S. Agar, M.D. Aspinall, J.S. Beaumont, E. Colley, M. Colling, J. Dykes, P. Kardasopoulos, and K. Mitton. Fast neutron tomography with real-time pulse-shape discrimination in organic scintillation detectors. *Nuclear Instruments and Methods in Physics Research Section A: Accelerators, Spectrometers, Detectors and Associated Equipment*, 834:36–45, 2016.

[190] S.A. Pozzi, M.M. Bourne, and S.D. Clarke. Pulse shape discrimination in the plastic scintillator EJ-299-33. *Nuclear Instruments and Methods in Physics Research Section A: Accelerators, Spectrometers, Detectors and Associated Equipment*, 723:19–23, 2013.

[191] M. Reginatto, P. Goldhagen, and S. Neumann. Spectrum unfolding, sensitivity analysis and propagation of uncertainties with the maximum entropy deconvolution code MAXED. *Nuclear Instrumentation and Methods in Physics Research Section A: Accelerators, Spectrometers, Detectors and Associated Equipment*, 476:242–246, 2002.

[192] S. Berg and W.N. McElroy. A computer-automated iterative method for neutron flux spectra determination by foil activation. volume II. SAND II (Spectrum Analysis by Neutron Detectors II) and associated codes. Technical Report, April 1966–July 1967.

[193] J.T. Routti and J.V. Sandberg. Unfolding activiation and multisphere detector data. *Radiation Protection Dosimetry*, 10(1-4):103–110, 1985.

[194] M. Reginatto and P. Goldhagen. MAXED, a computer code for maximum entropy deconvolution of multisphere neutron spectrometer data. *Health Physics*, 77(5):579–583, 1999.

[195] M. Grodzicka-Kobylka, T. Szczesniak, M. Moszyński, K. Brylew, L. Swiderski, J.J. Valiente-Dobón, P. Schotanus, K. Grodzicki, and H. Trzaskowska. Fast neutron and gamma ray pulse shape discrimination in EJ-276 and EJ-276G plastic scintillators. *Journal of Instrumentation*, 15(03):P03030, 2020.

[196] R. Nolte. Private communication, 2005.

[197] D.B. Pelowitz. MCNPX User's Manual Report LA-CP-07-1473. *Los Alamos National Laboratory*, 2008.

[198] J.K Dickens. Oak Ridge National Laboratory Report ORNL-6642. Technical report, 1998.

[199] R. Nolte and S. Röttger. Guidelines for Neutron Fluence Measurement at the TLABS Neutron Beam Facility Physikalisch-Technische Bundesanstalt. *unpublished*.

[200] S. Agostinelli, J. Allison, K. Amako, J. Apostolakis, H. Araujo, P. Arce, M. Asai, D. Axen, S. Banerjee, G. Barrand, et al. GEANT4—a simulation toolkit. *Nuclear Instruments and Methods in Physics Research Section A: Accelerators, Spectrometers, Detectors and Associated Equipment*, 506(3):250–303, 2003.

Appendix A

GEANT4 simulation for the optimisation of scintillator length

GEANT4 [200] is a toolkit developed by CERN for simulating the passage of particles through matter. For the work presented in this thesis a simulation of an EJ-276 scintillator in a 100 MeV neutron field was built to determine the optimum length of the scintillator for detecting 100 MeV neutrons.

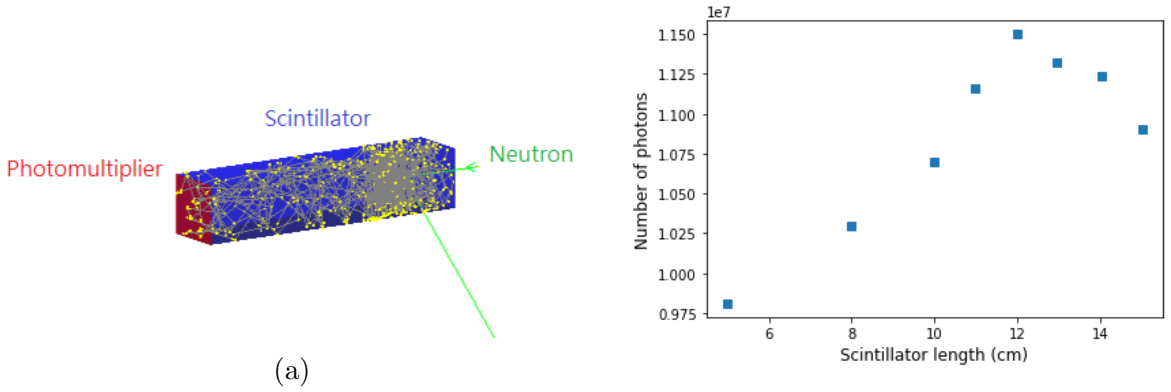

(a) (b)

Figure A.1: (a) The GEANT4 simulation of an EJ-276 scintillator when exposed to a 100 MeV neutron beam. The green lines represent neutrons, the grey lines represent the scintillation photons and the red surface at the end of the scintillator represents the photomultiplier device. (b) The number of photons incident on the photomultiplier as a function of scintillator length when the scintillator is irradiated with a beam of 100 MeV neutrons in the GEANT4 simulation.

There are two phenomena at play when it comes to determining the optimum length of the scintillator. First, is the probability of neutron interaction which, as seen in Section 3.1.1, improves as the length of the scintillator increases. Second is the transport of the scintillation light within the scintillator. While long scintillators are very good for

increasing the number of neutron interactions in the scintillator, which in return increases the number of photons produced, it does cause the attenuation of the scintillation photons before they can reach the photomultiplier device.

The simulation consisted of a EJ-276 scintillator with a 6×6 mm^2 profile covered in a diffuse reflector exposed to a beam of 100 MeV neutrons. The red end of the scintillator in Figure A.1 (a) was regarded as the photo multiplier device. When a photon exited the scintillator through this end the photon was considered 'detected'. Figure A.1 (b) shows the number of detected photons as a function of scintillator length, where the maximum number of photons detected occurs for a scintillator length of 12 cm.

Appendix B

Spectrum Unfolding

B.1 GRAVEL unfolding

The majority of the time GRAVEL unfolding is used to give a first estimate of the unfolded spectrum. The algorithm iteratively makes adjustments to the default spectrum until it arrives at a minimum χ^2_{dof} value. If supplied with a default spectrum which is not similar to the measured spectrum GRAVEL can still arrive at an accurate solution, however it is possible for the algorithm to converge on a local minimum which is not accurate to the measured spectrum. The algorithm is fairly insensitive to the χ^2_{dof} limit it is given since it will converge on a minimum value, given that minimum is above the limit set. However, the algorithm is sensitive to the limit on the number of iterations that is set. Too few iterations and it will not have arrived at the minimum χ^2_{dof}, too many iterations and it can over-converge. This is highlighted in Figure B.1 which shows the energy and light output spectra that result from under- and over-convergence. In the case where 1000 iterations were used the algorithm has over converged and produced an energy spectrum that is not physical. Conversely, when only 5 iterations are used the algorithm has not had enough iterations to arrive at a reasonable solution and therefore still somewhat resembles the flat spectrum it was given as a default spectrum. In Figure B.1 (c) the χ^2_{dof} starts to plateau at around 100 iterations making the optimum choice between 100 and 200 iterations. However, in Figure B.1 (b) the unfolded energy spectrum at 100 iterations has some significant variations from the input energy spectrum. Unfortunately it is not guaranteed that the algorithm will successfully converge on the correct solution.

When unfolding less complex spectra, such as the 14.1 MeV monoenergetic neutron field measured at the n-lab, over-convergence usually not an issue. In Figure B.2 the algorithm converges on near identical solutions at 100 iterations and 500 iterations. The solution that the algorithm converges on is in good agreement with the measured spectrum in these two cases. At 20 iterations the algorithm has not yet been able to converge on a solution, resulting poor agreement with the measured spectra.

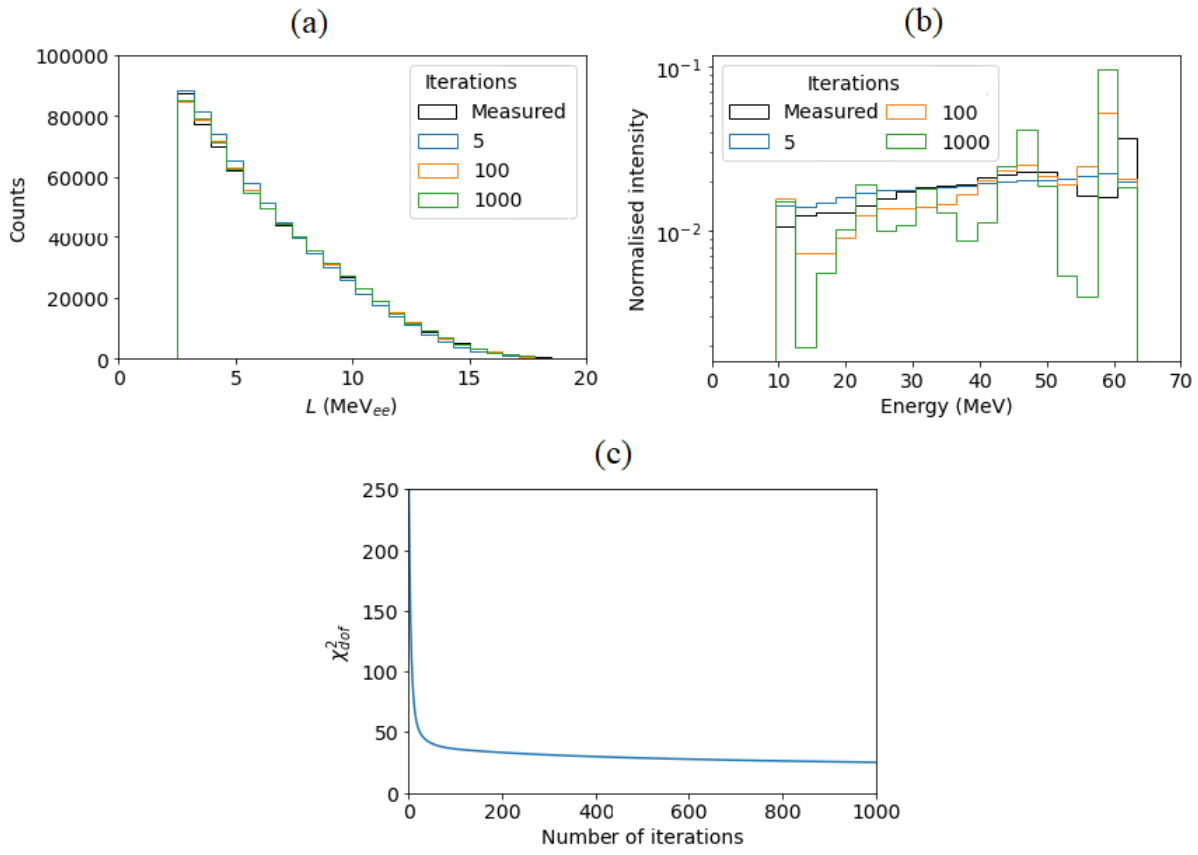

Figure B.1: The unfolding of the neutron field produced by 66.0 MeV protons on an 8.0 mm Li target measured at 16° with the EJ-276 compact detector using 5, 100 and 1000 iterations with the GRAVEL algorithm. (a) The measured light output spectrum in comparison to the re-folded light output spectra at the various number of iterations. The spectra agree with a χ^2_{dof} of 124 at 5 iterations, 34 at 100 iterations and 25 at 1000 iterations. (b) The unfolded energy spectra using the various number of iterations. (c) The χ^2_{dof} of input and re-folded light output spectra as a function of the number of iterations.

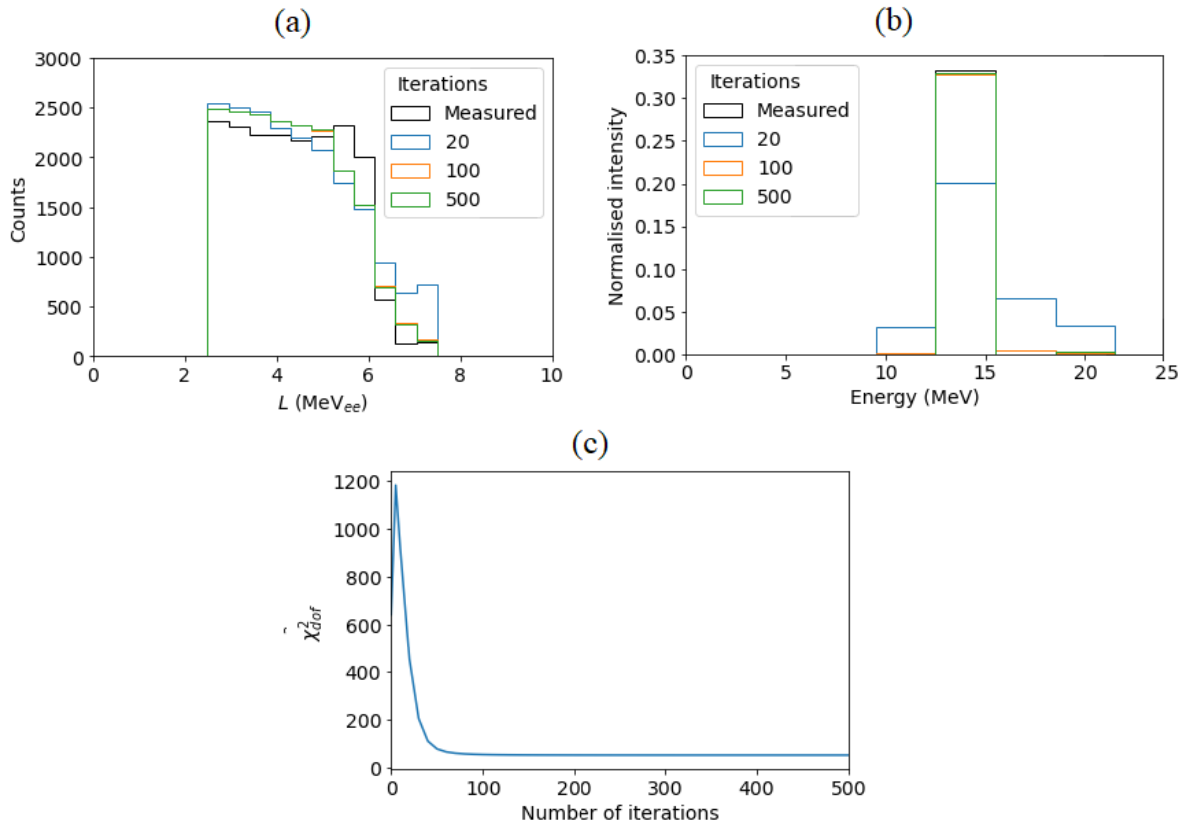

Figure B.2: The unfolding of the 14.1 MeV neutron field produced by a D-T fusion reaction measured with the EJ-276 compact detector using 20, 100 and 1000 iterations with the GRAVEL algorithm. (a) The measured light output spectrum in comparison to the re-folded light output spectra at the various number of iterations. The spectra agree with a χ^2_{dof} of 451 at 20 iterations, 54 at 100 iterations and 52 at 500 iterations. (b) The unfolded energy spectra using the various number of iterations. (c) The χ^2_{dof} of input and re-folded light output spectra as a function of the number of iterations.

B.2 The effects of default spectrum and χ^2_{dof} on MAXED unfolding

The maximum entropy approach of the MAXED unfolding algorithm is not iterative, it performs a search to find a solution with the specified χ^2_{dof}, making it highly sensitive to both the default energy spectrum and target χ^2_{dof} that it is given. Figures B.3 (a) and (b) show how the choice of default spectrum can affect the solution from the MAXED algorithm when the solutions have the same χ^2_{dof}. The solution using the flat spectrum is very similar to that achieved with the ToF spectrum for energies below 50 MeV, however with the flat spectrum the solution does not have the 62 MeV peak. Ultimately, the algorithm performs best when it is supplied a default spectrum that is similar to the expected spectrum.

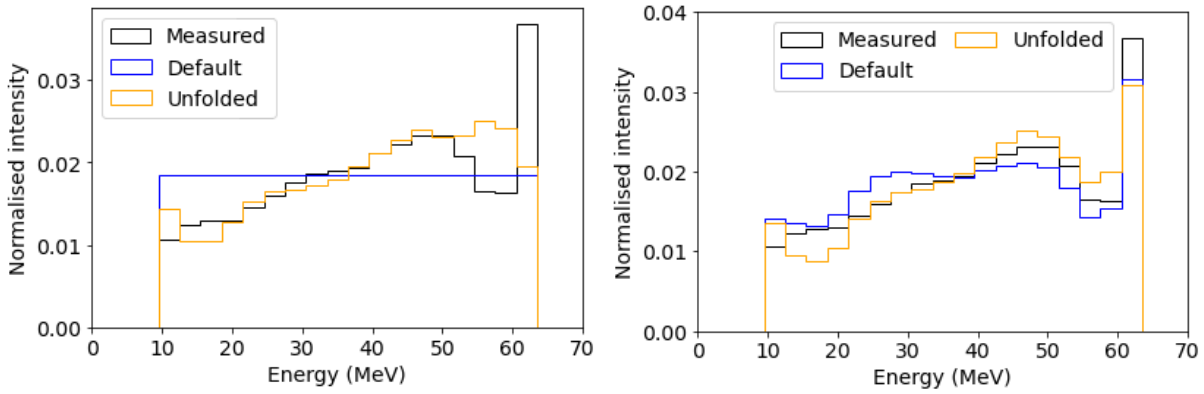

(a) (b)

Figure B.3: The energy spectra unfolded with MAXED using a (a) flat and (b) spectrum calculated from ToF using events with $L > 1$ MeV$_{ee}$ default spectrum and a χ^2_{dof} of 58.

The choice of χ^2_{dof} also has a large effect on the solution from MAXED unfolding. Figure B.4 (b) shows how the unfolded energy spectrum changes with the choice of χ^2_{dof}. The default spectrum has a χ^2_{dof} value of 149 and when a χ^2_{dof} that is not realisable is specified the algorithm will return the default spectrum. As seen previously, the best solution was found using a χ^2_{dof} of 58. Using a value higher than 58 or lower than 14 resulted in the algorithm returning the default spectrum.

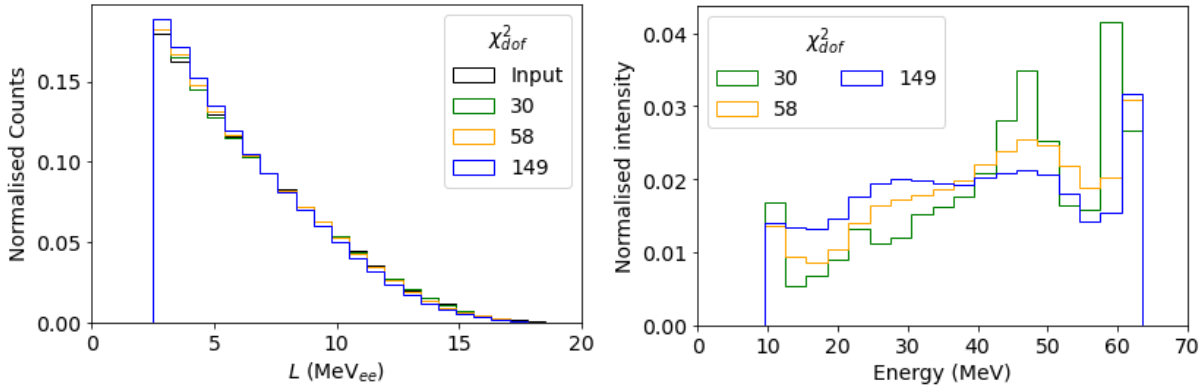

(a) (b)

Figure B.4: The unfolding of the neutron field produced by 66.0 MeV protons on an 8.0 mm Li target measured at 16° with the EJ-276 compact detector with the MAXED algorithm using χ^2_{dof} values of 30, 50 and 149. (a) The measured light output spectrum in comparison to the re-folded light output spectra at the various χ^2_{dof} values. (b) The unfolded energy spectra using the various χ^2_{dof} values.

Appendix C

Extension of the response matrix

One of the aspects of the future work on this project will be extending the response matrix to include energies between 1 MeV and 11 MeV using GEANT4 simulations. The measurements of the neutron fields with energies 3.225 MeV and 7.000 MeV performed at AMANDE, shown in Figures C.1 and C.2 will be used to verify the simulated response functions. Additionally, once the the response matrix includes these lower energies the well known neutron spectrum from the AmBe measurements shown in Figure C.3 and the monoenergetic 3.225 MeV and 7.000 MeV neutron fields, can be unfolded to test and characterise the unfolding in this region.

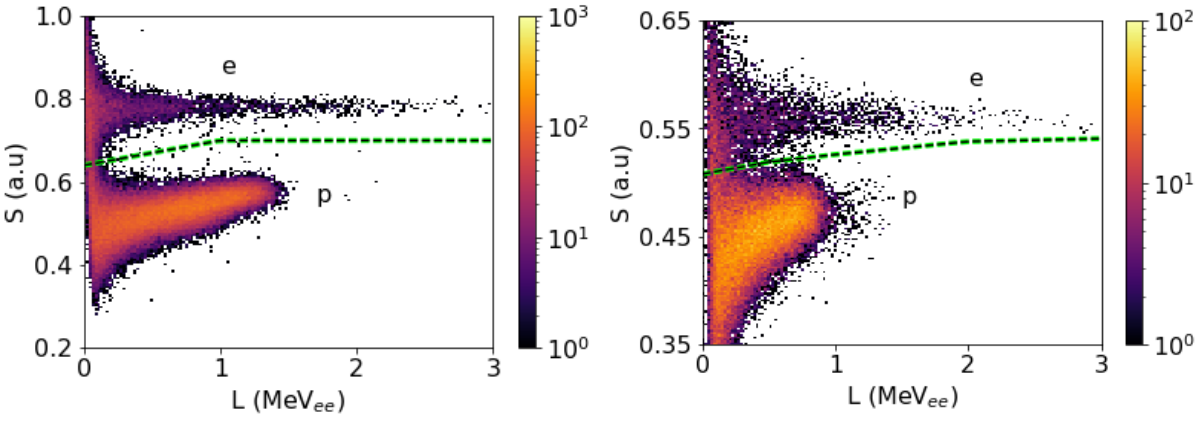

(a) (b)

Figure C.1: Counts as a function of light output parameter L and pulse shape parameter S for events in the (a) reference detector and (b) compact detector when irradiated by the neutrons and gamma rays produced by 0.432 MeV deuterons irradiating a deuterium target. Loci associated with recoiling electrons (e) and protons (p) are indicated. The green dashed line indicates the cut used to separate neutron and gamma ray events.

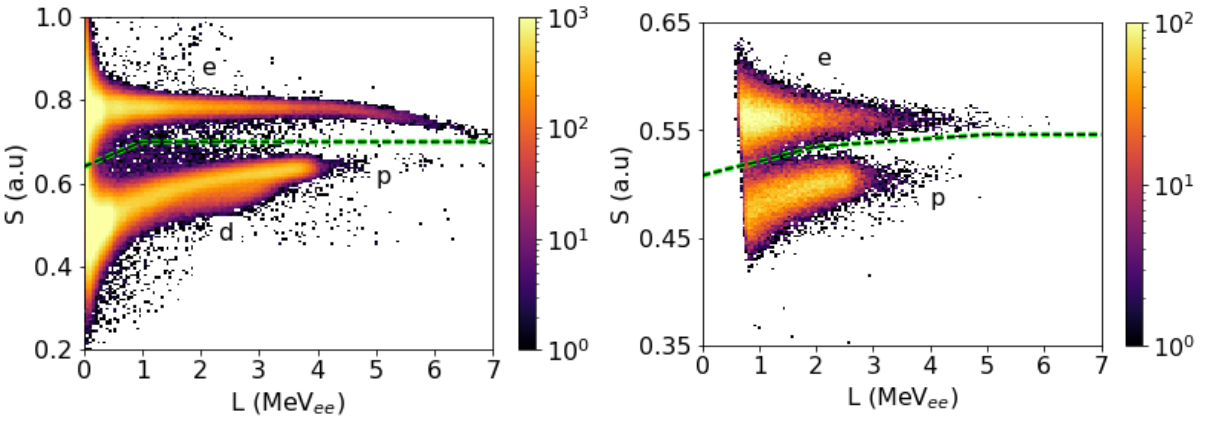

(a) (b)

Figure C.2: Counts as a function of light output parameter L and pulse shape parameter S for events in the (a) reference detector and (b) compact detector when irradiated by the neutrons and gamma rays produced by 3.777 MeV deuterons irradiating a deuterium target. Loci associated with recoiling electrons (e), protons (p) and deuterons (d) are indicated. The green dashed line indicates the cut used to separate neutron and gamma ray events.

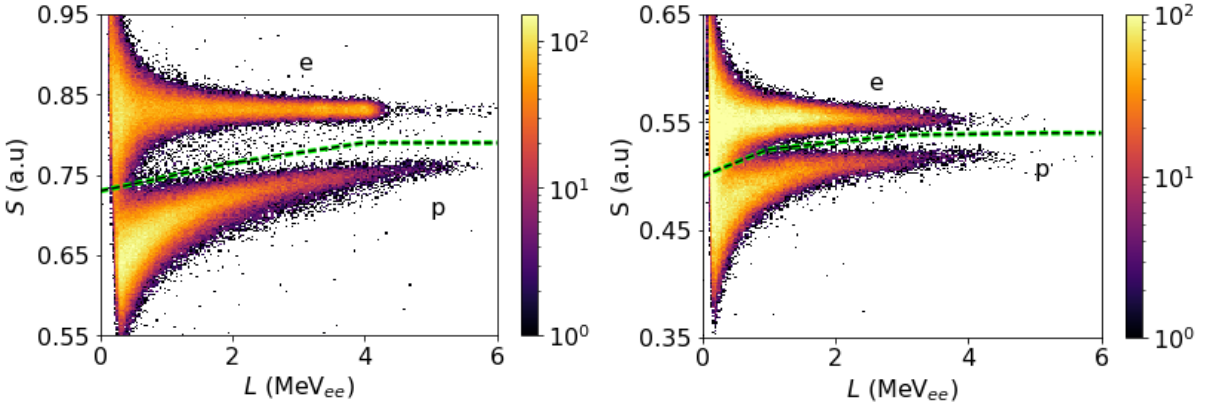

(a) (b)

Figure C.3: Counts as a function of light output parameter L and pulse shape parameter S for events in the (a) reference detector and (b) compact detector when irradiated by the neutrons and gamma rays produced by an AmBe source. Loci associated with recoiling electrons (e) and protons (p) are indicated. The green dashed line indicates the cut used to separate neutron and gamma ray events.

Appendix D

Paper presented at the International Nuclear Physics Conference

This paper has been submitted to the Proceedings of the 28th International Nuclear Physics Conference which was hosted in Cape Town (11-16 September 2022).

Measuring response functions for a new compact neutron spectrometer

E Jarvie[1*], A Buffler[1], T Hutton[1], Z Ndabeni[1,2], R Nndanganeni[3] and C Vandevoorde[4]

[1] Department of Physics, University of Cape Town, Rondebosch, 7700, South Africa.
[2] iThemba LABS, Faure, 7100, South Africa.
[3] South African National Space Agency, Hermanus, 7200, South Africa.
[4] GSI Helmholtz Centre for Heavy Ion Research, Darmstadt, 64291, Germany.

E-mail: erin.jarvie05@gmail.com

Abstract. A compact neutron spectrometer consisting of a (0.6 x 0.6 x 12.0 cm^2) EJ-276 plastic scintillator coupled to a silicon photomultiplier has been designed. An essential aspect of the characterisation of the spectrometer is the measurement of detector response functions for neutron energies between 1 - 100 MeV. The process of producing response functions for the compact detector using neutron time-of-flight measurements at iThemba LABS is presented.

1. Introduction

The high energy neutron fields found in medical, aviation [1,2] and space environments [3,4] have serious impacts on both biological and technological systems. These fields are not well studied and understood, in part, due to a lack of suitable instrumentation. A new compact spectrometer has been developed at the University of Cape Town (UCT) with the main focus on the detection of neutrons produced by cosmic rays at aviation altitudes and in space. The device is comprised of an EJ-276 plastic scintillator coupled to a silicon photomultiplier (SiPM) and has been characterised with neutrons of energy up to 63 MeV at iThemba LABS.

To measure neutron energy spectra with scintillators outside a laboratory environment the method of spectral unfolding must be used, which requires accurate, detector-specific response functions. For neutron energies <20 MeV response functions can be reliably simulated, however above 20 MeV the response functions must be measured due to poor knowledge of the cross sections for the many possible reaction channels. In this work the process of measuring response functions for the compact detector using ns-pulsed neutron beams at iThemba LABS is presented.

2. Methodology

2.1. Measurements

The spectrometer consists of an EJ-276 plastic scintillator (0.6 x 0.6 x 12 cm^3) capable of pulse shape discrimination coupled to a 0.6 x 0.6 cm^2 SensL C-series MicroFC-60035 silicon photomultiplier operated at +28.5 V using an external power supply. The measurements with the compact spectrometer are referenced to a 5⌀ x 10 cm^3 BC-501A liquid scintillator coupled

to a 12-stage photomultiplier tube (PMT). The data for both detectors were acquired digitally using a CAEN DT5730 digitiser and custom acquisition software [5,6].

The data presented in this paper were acquired during a measurement campaign at the iThemba LABS D-line fast neutron facility [7,8]. Neutron beams were produced via ^{7}Li(p,xn) reactions using proton beams available from the $k = 200$ separated sector cyclotron. During this campaign a 66 MeV proton beam was used, producing neutrons with a maximum energy of 63 MeV.

2.2. Time-of-flight

Time-of-flight (ToF) [9] is a commonly used technique for determining the energy spectrum of a neutron beam. A time-of-flight parameter may be defined from the time between the event pulse in the detector and reference pulse associated with the ns-pulsed proton beam. Figure 1 shows the ToF spectra measured at 16° relative to the proton beam for the two detectors with a peak centred at 26.7 ns corresponding to the gamma rays produced at the target and a distribution of neutron events from $\sim$ 80 ns. The gamma ray events are used as a calibration point for the ToF using the known distance (8.00 m) between the target and the front of the detector.

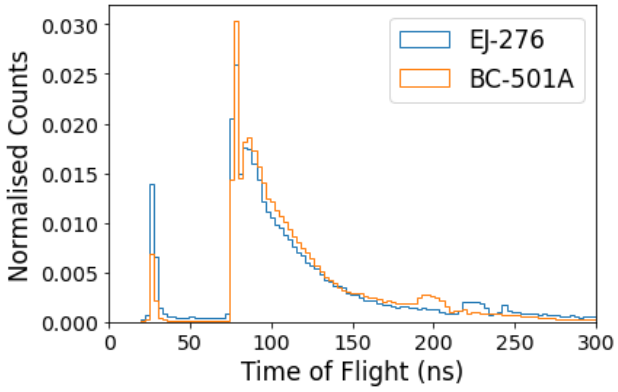

Figure 1: Time-of-flight spectra for a 66 MeV proton beam incident on a 8.0 mm Li target for the compact EJ-276 and reference BC-501A detectors.

2.3. Pulse shape discrimination

The EJ-276 plastic scintillator used in this project produce pulses with different rise time characteristics for events produced by electron excitation (gamma ray interactions) and events produced by recoil hadrons (neutron interactions). This property is utilised to separate the two event types in a technique known as pulse shape discrimination (PSD). There are several methods for performing digital PSD. In the data presented the charge comparison method was used:

$$S = k\frac{Q_s}{Q_L} + c \tag{1}$$

where S is the pulse shape parameter, Q_s is the integral of the pulse over a short time period (typically 10 ns for the BC-501A detector and 42 ns for the EJ-276 detector), Q_L is the integral of the pulse over a long time period (such as 800 ns for the BC-501A detector and 1400 ns for the EJ-276 detector) and k and c are scaling constants [10]. The long integral is also used a measure of the size of the pulse, which is related to the light output and energy of the event. Measurements of gamma rays with known energy are used to to calibrate the scaling between long integral and light output (L, units MeV$_{ee}$) which is linear. Figures 2 (a) and 2 (b) show density plots for pulse shape parameter S as a function of light output parameter L for both detectors and illustrate the cuts used to separate the gamma ray events from the neutron events.

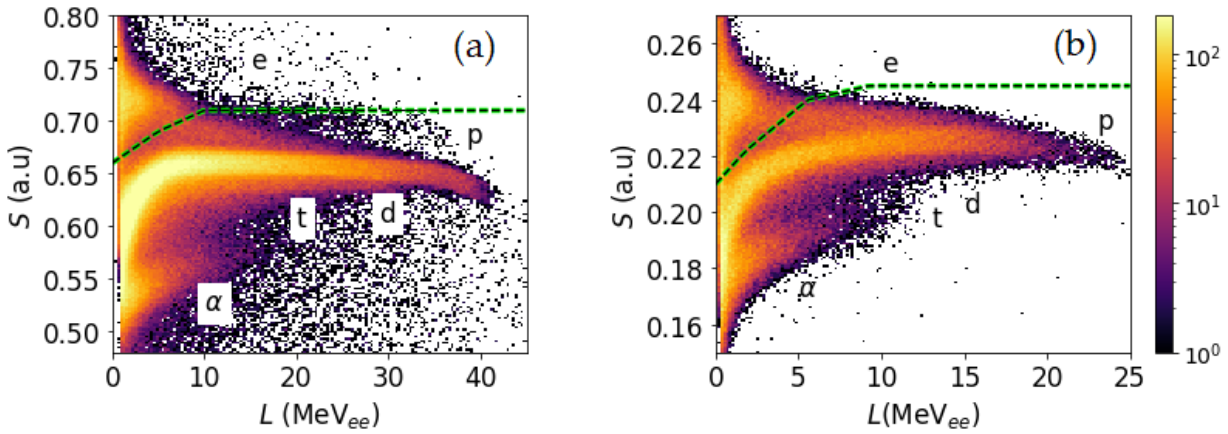

Figure 2: Counts as a function of light output parameter (L) and pulse shape parameter (S) for events in the (a) BC-501A and (b) EJ-276 detectors when exposed to neutrons and gamma rays produced by the irradiation of a 8.0 mm Li target by a proton beam of energy 66 MeV. Loci associated with recoiling electrons (e), protons (p), deuterons (d), tritons (t) and alpha-particles (α) are indicated. The dotted lines indicates the cuts used to separate neutron and gamma ray events.

2.4. Calculation of neutron energy spectrum

After the neutrons have been separated from the gamma ray events using PSD, the neutron ToF spectrum can be transformed to an energy spectrum by calculating the relativistic kinetic energy of the neutrons [11]. A comparison of the energy spectra obtained from the ToF measurements for the two detectors after correcting for efficiency is shown Figure 3.

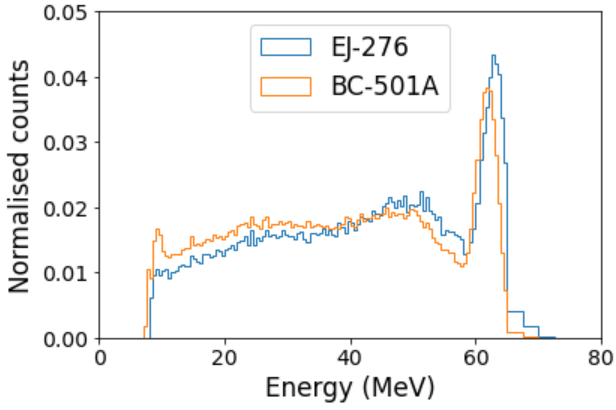

Figure 3: Neutron energy spectra from ToF for the compact EJ-276 and reference BC-501A detectors measured at 16° for a 66 MeV proton beam incident on a 8.0 mm Li target.

2.5. Response functions

Spectrum unfolding uses a deconvolution algorithm and a matrix of energy dependent detector response functions to produce an energy spectrum from a measured light output spectrum [12]. In the present work, the measured response functions are made by taking cuts in the neutron energy spectrum obtained through ToF (Figure 3) and producing a light output spectrum from the events within the cut. If the energy window is sufficiently small (in this work 0.5 MeV) then the light output spectrum may be regarded as being for nearly monoenergetic neutrons. By repeating this over the full energy range of the available energy spectrum a response matrix is formed.

Figure 4 shows a selection of the response functions for the the compact EJ-276 detector and the BC-501A reference detector. The detectors have similar response functions at lower energies ($<$ 10 MeV), however as the energy increases the response functions for the EJ-276 detector begin to deviate significantly from those of the BC-501A reference detector. The difference in detector response is attributed largely to differences in light collection characteristics for the two detectors and highlights the necessity of having detector specific response functions.

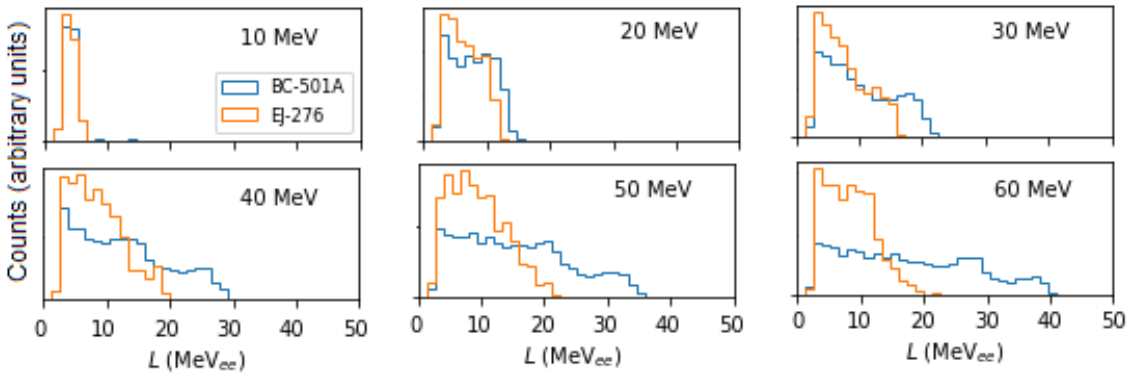

Figure 4: Response functions measured for the BC-501A and EJ-276 detectors at average energies of 10 MeV, 20 MeV, 30 MeV, 40 MeV, 50 MeV and 60 MeV.

3. Conclusion

A compact neutron spectrometer consisting of a (0.6 x 0.6 x 12 cm^3) EJ-276 plastic scintillator coupled to a silicon photomultiplier has been constructed and is in the process of being characterised for neutrons up to 100 MeV. Response functions were measured at iThemba LABS using a ns-pulsed 66 MeV proton beam and neutron time-of-flight spectroscopy. The response functions will be used to build a response matrix so that neutron spectroscopy can be performed outside of a laboratory environment through spectrum unfolding. Further characterisation of the spectrometer and validation of the response functions is currently being done with data acquired at the UCT n-lab and IRSN AMANDE fast neutron facility.

References

[1] Goldhagen P, Clem J and Wilson J 2004 *Rad. Prot. Dosim.* **110** 387-92
[2] Clem J et al. 2004 *Rad. Prot. Dosim.* **110** 423-8
[3] Grieder P 2001 *Cosmic Rays at Earth: Researcher's reference manual and data book* (Elsevier)
[4] Bagshaw M and Illig P 2019 *Travel Medicine (Fourth edition)* (Elsevier) pp 429-36
[5] Sole C 2022 *A new digital data acquisition system for neutron metrology* MSc thesis (University of Cape Town)
[6] Comrie A 2016 *A new compact neutron spectrometer* PhD thesis (University of Cape Town)
[7] Mosconi M, Musonza E, Buffler A, Nolte R, Röttger S and Smit F 2010 *Radiation Measurement* **45** 1342-5
[8] Ndlovu N, Boso N, Buffler A, Geduld D, Hutton T, Lacoste V, Leadbeater T, Malekam P and Smit F 2020 *In 22nd Int. Conf. on Cyclotrons and their Applications* 181–4
[9] Copley J and Udovic J 1993 *Journal of research of the National Institute of Standards and Technology* **98** 71
[10] Comrie A, Buffler A, Smit F, and Wörtche H 2015 *Nucl. Inst. Meth.* A **772** 43–9
[11] Herbert M et al. 2014 *Rad. Prot. Dosim.* **161** 377–82
[12] Reginatto M, Goldhagen P and Neumann S 2002 *Nucl. Instr. Meth.* A **476** 242–6